CFD Analysis, Sensing and Control of a Rotary Pulse Width Modulating Valve to enable a Virtually Variable Displacement Pump

A DISSERTATION
SUBMITTED TO THE FACULTY OF THE GRADUATE SCHOOL
OF THE UNIVERSITY OF MINNESOTA
BY

Meng Wang (Rachel)

IN PARTIAL FULFILLMENT OF THE REQUIREMENTS
FOR THE DEGREE OF
Doctor of Philosophy

Prof. Perry Y Li, adviser
Prof. Thomas R Chase, adviser

August, 2017

Acknowledgements

There are many people that have earned my gratitude for their contribution to my time in graduate school. I would like to show my sincere appreciation to my advisers, Dr. Perry Li and Dr. Thomas Chase for their education, advise, guidance, patience, and all the help. Their passion about research and engineering has deeply affected me. They grew me into a real engineer. I would like to acknowledge National Science Foundation (NSF) for supporting my research through grants $EEC - 0540834$ and ENG/CMS-0409832. I would also like to thank Center for Compact and Efficient Fluid Power (CCEFP) for supporting my research. I would like to thank Mike Rannow and Haink Tu for their kind help during my graduate school study and research, and the great non-academic activities. Finally, I would like to thank my Mom and Dad for their strong support of my studying abroad.

Dedication

To my Mom and Dad

Abstract

Hydraulic systems have been widely utilized for heavy duty industries for their competitive advantages of high power density, low cost, and flexible circuit design. However, the efficiency of hydraulic systems typically is not very competitive due to high throttling losses, which limits their applications. On/off valve based control of a hydraulic system is an approach that can potentially increase the hydraulic system's efficiency significantly. This approach combines the strengths of throttling valve control and variable displacement unit control. The former has the advantage of high control bandwidth and precision, but the disadvantage of low efficiency due to throttling loss; the latter has the advantage of high efficiency, but the disadvantage of being bulky, heavy, costly, and the control bandwidth is low when compared to valve control. To create a potentially high efficiency with relatively low cost solution, a fixed displacement pump, an accumulator, and a high speed on/off valve are combined to create a virtually variable displacement pump (VVDP). By pulse width modulating (PWM) the flow from the supply to the load via the on/off valve, the average output flow can be varied by adjusting the PWM duty ratio. The key technology to this hydraulic configuration is the pulse width modulated on/off valve. A novel rotary high speed on/off valve concept has been proposed. This concept can enable different digital hydraulic configurations, such as VVDP, VVDPM (pump/motor), and virtually variable displacement transformer. Research conducted in this dissertation supports the design, modeling, and control of the rotary on/off valve. A 3-way, high-speed, rotary, self-spinning on/off valve was developed for the VVDP configuration. The valve has two degrees of freedom. The spool's rotary motion realizes the high-speed switching required for the PWM function. This motion can be self-driven by capturing the fluid's angular momentum via a unique valve spool turbine design. The spool's axial motion determines the valve PWM duty ratio, and this motion is driven externally.

Firstly, to understand the flow inside the valve, and to quantify the valve pressure drop with the key valve parameters, a computational fluid dynamics (CFD) analysis is conducted in chapter 2. Analytical and semi-empirical formulas to model the pressure

drop across the valve spool as a function of flow rate and key valve geometrical parameters are developed. The torque generated by the valve turbines are also analyzed using CFD to validate the analytical models which calculate the torque as a function of flow rate and key valve geometrical parameters. These equations are utilized in an optimization analysis to optimize the valve geometry, targeted at reducing the valve's power loss. CFD is also utilized to optimize the valve's interior flow path to reduce the fluid volume inside the valve while maintaining a low pressure drop, so that both the compressible loss and the throttling loss of the valve are reduced. The CFD analysis enabled reducing the throttling loss pf a prototype valve design by 62.5% and reducing the compressible loss by 66%.

Secondly, the sensing and estimation of the valve spool's rotary position and velocity are addressed in chapter 5. Given the limitation on sensing distance and the requirement of a simple sealing structure, a coarse, non-contacting, optical sensor is proposed to measure the spool's angular position. Measurement events in the form of encoder count changes are obtained at irregular times and infrequently. An event-based Kalman filter is developed to improve the resolution and to provide continuous estimates of the spool's angular position and velocity.

Thirdly, the spool's axial motion actuation, sensing, and control development are addressed. The on/off valve's duty ratio is regulated by controlling the valve spool's axial position. In chapter 4, a driving mechanism to work with the self-spinning valve's feature and the corresponding sensing and control methods are developed to manipulate the spool's axial position. In the first generation's driving system, a geroter pump is hydro-statically connected to both ends of the spool chamber to move the spool axially. This design simplifies the sealing structure in order to achieve self-spinning. An optical sensor is utilized as a non-contact approach to measuring the spool's axial displacement. The measurement is corrupted by a structured noise caused by the spool's rotary motion. A periodic time varying model is proposed to model the structured noise, which can capture the main dynamics with a low order system. An analysis of the observability of the augmented system (plant plus structured noise) is conducted. A state observer can be built to distinguish between the axial spool position and the structured noise, and the estimated position can then be used in the control law. The sleeve chamber pressure dynamics are ignored, and a linear feed-forward with a Proportional-Integral

controller is developed for spool axial positioning. The self-spinning function ties the spool rotary speed with the valve flow. The controller was experimentally implemented, and achieved good spool regulation results.

In order to investigate the PWM frequency and the flow rate properties independently, an external driving mechanism is developed in chapter 5. A new passivity based nonlinear controller has been proposed which considers the pressure dynamics inside the sleeve chamber. This controller can provide more robust axial position control. From theoretical analysis' point of view, a passivity framework for hydraulic actuators is developed by considering the compressibility energy function for a fluid with a pressure dependent bulk modulus. It is shown that the typical actuator's mechanical and pressure dynamics model can be obtained from the Euler-Lagrange equations for this energy function and that the actuator is passive with respect to a hydraulic supply rate. The hydraulic supply rate contains the flow work (PQ) and the compressibility energy, where as the latter one has typically been ignored. A storage function for the pressure error is then proposed and the pressure error dynamics are shown to be a passive two port subsystem. Trajectory tracking control laws are then derived using the storage function. Since some of the states utilized in the passive controllers are from an estimator instead of being directly measured, the chapter also provides the analysis on the convergence of both tracking errors and the estimation errors to zero. This passivity-based nonlinear controller implemented with a high gain observer is applied experimentally on the valve. Experimental results validate the effectiveness of this new control system.

Lastly, the VVDP is implemented as the variable displacement pump in a direct displacement control open circuit, as presented in chapter 6. A variable flow source (VVDP), a directional valve, and a proportional valve are coordinated to manipulate the motion of the hydraulic actuator in an energy efficient way. The passivity-based nonlinear controller as discussed in chapter 5 is proposed to realize accurate actuator trajectory tracking. A nominal method to optimally distribute the control efforts between the control valve and the variable flow pump is proposed. This method can accommodate different control bandwidths from the valve and the pump, so that the valve has a large nominal opening to reduce the throttling loss. Experimental results validate the effectiveness of the control strategy.

Contents

List of Tables

List of Figures

Chapter 1

Introduction

A novel high-speed rotary 3-way on/off valve has been developed as an enabling technology for digital hydraulics. Research conducted in this dissertation focuses on the modeling, sensing, actuation and control of the valve spool motion, and investigating its implementation in a virtually variable displacement pump (VVDP) configuration. The successful development of the rotary 3-way valve and the VVDP can potentially make hydraulic actuator motion control more robust, accurate and energy efficient.

In section 1.1 of this chapter, an introduction to the operating principles of this rotary valve will be presented. The background material on how to improve the hydraulic system performance from both the component development (i.e. new valve technology) perspective and control technique improvement perspective will be discussed in section 1.2. Section 1.3 will give an overview of the research scope. This chapter will conclude with an outline of the rest of the dissertation structure.

1.1 Background

Hydraulic systems have been widely used due to their high power density, durability, and installation flexibility. Currently, two approaches are frequently utilized to achieve hydraulic motion control in fluid power systems. One approach is to manipulate the pressure or flow via a control valve. This approach has a significant advantage in control bandwidth and precision due to the small inertia being moved inside a valve. In addition, the hydraulic circuit is flexible, and the overall system can be compact.

The disadvantage of this approach is the low system efficiency due to throttling losses across the control valves. The other approach is to directly control the displacement of a variable displacement pump or motor. Ideally, energy is produced to do useful work only, and no excess energy is consumed by throttling the flow. Therefore, this approach can lead to a high system efficiency. However, variable displacement pumps and/or motors are typically more expensive, heavier, and bulkier compared with fixed displacement machines with the same flow capability. Moreover, the control bandwidth and the cost to achieve the control bandwidth for variable displacement machines are less desirable than for valve control [1].

One additional approach which partially reduces the system throttling losses is a load sensing system. In this approach, the flow source can be changed from a fixed displacement pump to a variable displacement pump with its output pressure adapted to the load pressure. The load sensing concept has been introduced to fluid power systems for off-highway vehicles to reduce the system energy consumption. In this hydraulic configuration, a variable displacement pump is typically used. The supply pressure is regulated on-line to match with the maximum working pressure [2]. This approach can improve the system efficiency significantly if only one load is being driven. However, if multiple loads are sharing the same power source, the throttling loss can be minimized only for the valve which requires the highest pressure. Valves associated with additional actuators may still lead to high throttling losses.

To combine the strengths of the "valve" approach and of the "pump" approach, a virtually variable displacement pump (VVDP) concept has been developed, which enables the throttle-less flow/pressure control of a fixed displacement pump using an on/off valve. This approach has the advantage of operating the throttling valve in its most efficient state most of the time, because the valve is either fully open to load, connecting the full pump flow from high pressure to the load; or fully open to tank, routing the full pump flow back to a tank. The VVDP does not have a physical device to vary displacement; variable flow to load is achieved "virtually" by manipulating an on/off valve that shifts the output of the pump between load and tank. The working principle of a VVDP is illustrated in Fig. 1.1. By a using pulse width modulated (PWM) on/off valve and a fixed displacement pump, the average output flow of the VVDP can be controlled by the on/off valve PWM duty ratio. The VVDP system has

the potential to be smaller in size and lighter than a variable displacement machine while maintaining the energy efficiency of the existing variable displacement machines. The new pump concept can be extended to the development of virtually variable displacement motors, virtually variable displacement pump-motors, and virtually variable displacement hydraulic transformers.

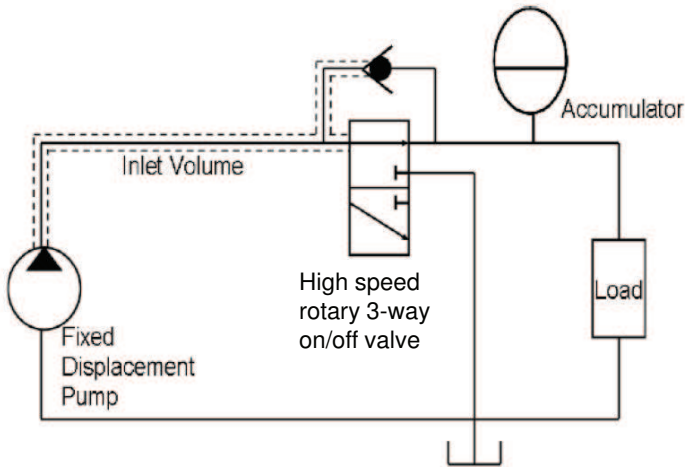

Figure 1.1: Virtually variable displacement pump circuit

The key component of the VVDP as shown in Fig. 1.1 is the high speed on/off valve. The overall efficiency of the VVDP is heavily affected by the on/off valve efficiency. An ideal on/off valve will have the following properties simultaneously: low fully open pressure drop across the valve, fast transitions between the efficient states, high PWM frequency, and low actuation power. The valve openings between different flow paths are typically realized via a valve spool's linear motion or rotary motion. Compared with linear on/off valves, rotary on/off valves have the potential to approach all four specifications of an ideal on/off valve simultaneously. The main reason is that, to achieve the same PWM frequency, the actuation power required for rotary valve is proportional to PWM frequency squared; whereas the actuator power required for linear valve is proportional to PWM frequency cubed.

A novel high-speed rotary 3-way on/off valve has been developed to be implemented in the VVDP configuration, as shown in Fig. 1.2 [3]. The valve consists of a stationary sleeve and a rotating spool. The sleeve is mounted directly onto a fixed displacement

vane pump through a customized pump housing to minimize the fluid volume in between the pump and the valve. Inlet nozzles tangential to the bore are cast inside the sleeve. The spool can rotate and translate axially inside the sleeve.

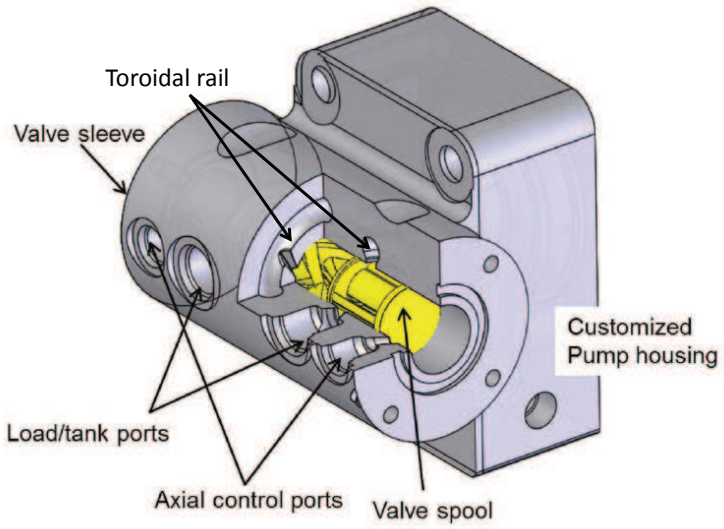

Figure 1.2: Schematic of the high speed rotary 3-way on/off valve

The valve spool consists of three sections: a center PWM section and two outlet turbines, as shown in Fig. 1.3. The helical barriers wrapped around the valve spool partition the spool into two parts. The upper triangle is connected with the upper turbine via an axial path in the center of the spool. The lower triangle is connected to the lower turbine. When the valve spool spins inside the sleeve, depending on the region of the spool that is connected to the inlet nozzle, the inlet flow is directed either to the load branch or to the tank branch, which achieves the pulse width modulation (PWM) of the source pump flow. When the spool spins inside the sleeve, the inlet flow is directed to the load branch and then the tank branch in an alternate manner to achieve pulse width modulation of pump flow. The duty ratio is defined as the fraction of time when the valve in its "on" position (inlet flow connected to the load branch) over one PWM period. The spool's axial position varies the landing of the nozzle on the spool center section. This varies the amount of flow directed to the load branch over one spool revolution, and therefore the spool axial position controls the valve PWM

duty ratio.

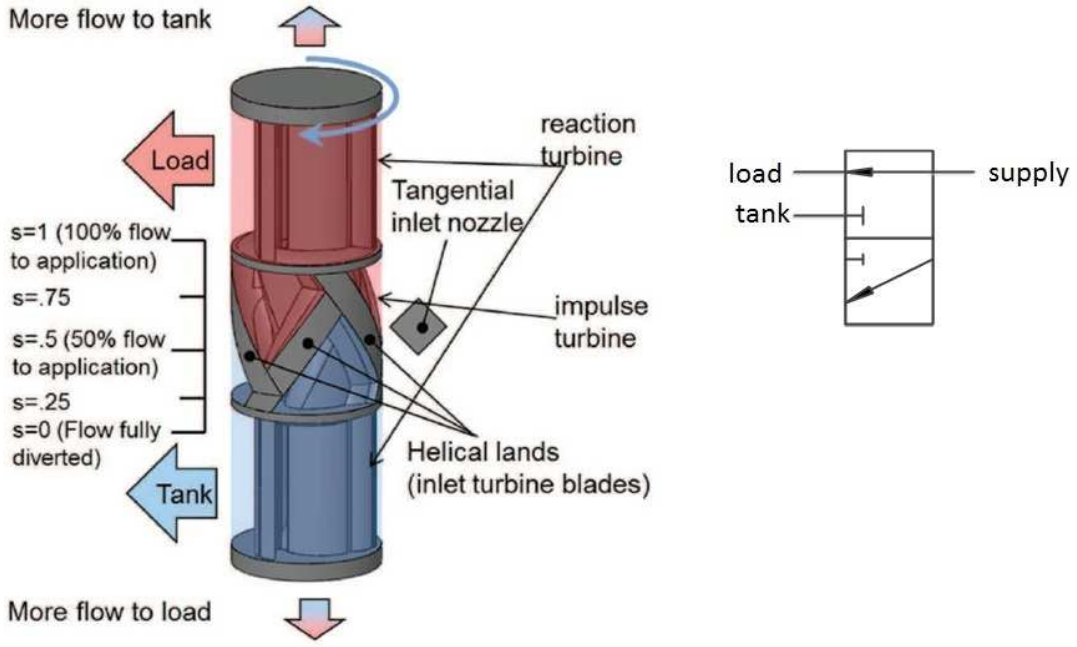

Figure 1.3: Valve spool of the high speed rotary 3-way on/off valve

The design of the valve flow path can significantly affect the valve characteristics, and the accuracy of the rotary valve spool motion can affect the operation of the valve, further affecting the performance of the VVDP. The issues of flow path modeling, valve spool motion sensing, actuation, and control problems will be addressed in this dissertation.

1.2 Literature Review

This section will provide a literature review of the work conducted by other researchers in hydraulic component and system design and control algorithms. We will first review several digital hydraulics configurations in section 1.2.1. Since the enabling component to different digital hydraulic configurations is the digital valve, digital hydraulic configurations and the current state of the art for high-speed on/off valve technologies will be reviewed in section 1.2.2. We use a Computational Fluid Dynamics (CFD) tool to facilitate the design and optimization of the flow path. A summary of CFD as a tool

to aid the design and optimization of hydraulic valves will be reviewed in section 1.2.3. Non-contact sensors have been selected as the main sensing mechanism for both the spool's rotary and axial positions. Existing non-contact sensing methods will be compared in section 1.2.4. A literature review of different control strategies for manipulating a hydraulic actuator will be discussed in section 1.2.5. Finally, different hydraulic configurations to realize direct displacement control will be considered in section 1.2.6.

1.2.1 Digital hydraulics

An efficient method for controlling a hydraulic actuator is to combine throttling valve control with variable displacement control. A digital hydraulic valve can be used in conjunction with a fixed displacement pump/motor to create a variable displacement device for this approach.

One research direction is to develop a parallel-connected on/off valve, proposed by Linjama et al. [4][5]. In this approach, N 2-way on/off valves are connected in parallel to replace one proportional valve. Each on/off valve can be controlled independently, and the valve set can produce 2^N discrete opening areas. Since each valve is an on/off valve with low cost and high robustness, using the valve set to control a linear or rotary hydraulic actuator lead to high system efficiency, high reliability, and low cost. However, expensive and complicated control strategies are required for controlling actuators using this valve. The complexity of the system drastically increases the difficulty of the controller design, which limits its application.

Another research direction is switched-mode hydraulics. In 1988, Brown et al. [6] proposed a hydraulic rotary switched inertance servo transformer, where a novel rotary valve was developed to enable the "switch-mode" feature. Tomlinson and Burrows [7] proposed a circuit to achieve a variable flow supply by controlling the unloading of a fixed displacement pump via an on/off unloading valve.

The switch-mode power supply from power electronics has been adapted to a hydraulic system. Gu et al. [8] proposed both boost and buck circuits via the combination of a high-speed switch valve, a check valve, and a hydraulic inductor (hydraulic motor with a flywheel), as shown in Fig. 1.4. In the switch mode hydraulic pressure boost circuit, the supply flow being operated at pressure P_1 is either connected to load (after the check valve), or is routed back to P_b, and the average load flow can be regulated

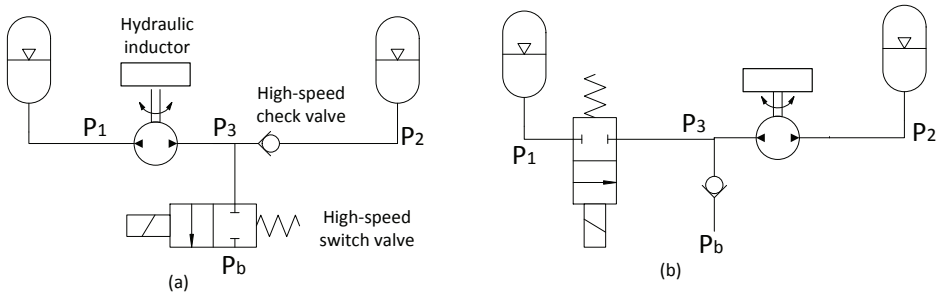

Figure 1.4: Switch mode hydraulic circuits [8] (a) pressure boost circuit, (b) pressure buck circuit

from the high-speed switch valve duty ratio. Similarly, in the buck circuit, the flow to load is either being provided from P_1 or being pulled out from P_b, depending on the state of the high-speed switch valve, and the average flow to load is controlled by the high-speed valve duty ratio. Similarly, Li et al. [1][9] proposed a VVDP by combining a fixed displacement pump, a PWM on/off valve and an accumulator (see Fig. 1.5), which is also the hydro-mechanical analog of the DC-DC boost converter.

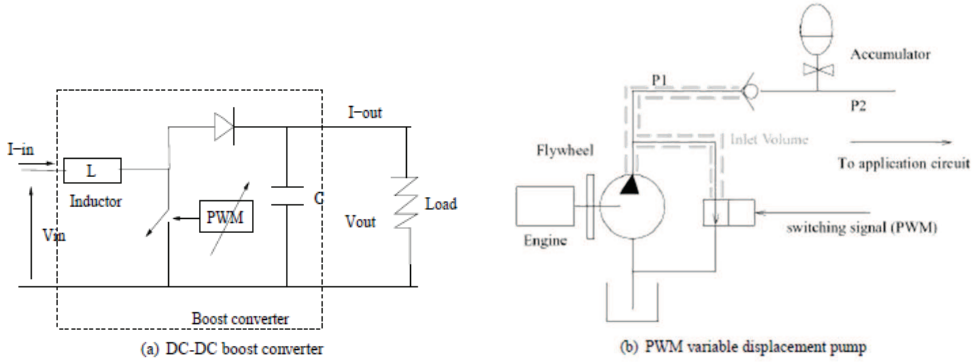

Figure 1.5: Electrical DC-DC boost converter and its hydraulic analog [9]

All the hydraulic circuits discussed here rely on the on/off valves to function efficiently. Ideally, hydraulic circuits using on/off valves should be efficient, because either the valve is fully open, with minimal pressure drop across the valve, or it is fully closed, with no flow consumed. However, when on/off valves are operated in between the on and the off states, they will still be partially open, and therefore there is still some

throttling loss associated with the on/off operations. Another problem associated with the digital hydraulic system is the pressure and flow ripples caused by the valve on/off motions. The ripple size is heavily affected by the valve PWM frequency [9]. Keeping other components the same, the faster the PWM frequency is, the smaller the ripple is. The problem to address is how to create an on/off valve that meets the following requirements at the same time, 1) large orifice to allow flow to pass through with a small pressure drop, 2) fast transition to reduce the time when the valve is partially open, 3) ability to operate at high PWM frequency to reduce the flow and pressure ripples, 4) low actuation power.

1.2.2 On/off Valves

The research on high speed on/off valves started in the late 1970s. Besides drastically reducing the throttling loss, on/off valves are also less susceptible to contamination compared with high speed servo valves. Current on/off valves can be categorized by the motion of the valve spools into two types : linear on/off valves and rotary on/off valves.

Linear on/off valves

Solenoid spool and poppet type valves have been widely investigated as candidates for high speed on/off valves in fuel injection applications. The valve operation frequency can be increased using three methods: increase the electro-magnetic force, reduce the resisting force, and reduce the mass of the moving part [10]. Different layouts of the poles and the scheduling of the pole energizing have been investigated to improve the response time [11][12]. Such valves typically achieve the fast response time with high actuation power consumption. For example, in 1994, Kajima et al. [13] developed a high-speed 4-way spool-type solenoid valve, with a flow rate capability of $60lpm$, a pressure drop of $6MPa$, and a switching time of $1ms$. The voltage required to actuate the valve is around $300V$, and the maximum current can be up to $30A$. To reduce the actuation power, a valve with two or more stages is required: the main stage is driven hydraulically, and the pilot stage is driven electrically. For example, Park et al. [14] proposed a hydraulic high-speed solenoid valve with a two-stage mechanism, which is capable of a $2ms$ switching time, a flow rate of $9lpm$, and a maximum pressure of $14MPa$.

The displacement of the pilot stage valve in a multiple-stage valve is typically small, and high speed operation is required. Piezoelectric (PZT) materials are good at producing small displacements at high speed and therefore have been investigated as the valve poppet actuator. Yokota and Akutu [15] developed a high-speed poppet-type on/off valve driven by multi-layered PZT elements with a switching time less than $100\mu s$. Experimentally, the valve was validated to follow a $2kHz$ rectangular wave. Neither the flow capability nor the driving power was reported. Because the valve was recommended as a pilot stage for a servo valve, the flow capability should be small. Lu et al. [16] reported a high-speed 3-way valve driven by a PZT component, which achieved an opening time of $1.2ms$, and a closing time of $1.7ms$. The flow rate is small ($8lpm$), and the pressure drop is large ($10MPa$). A similar high speed on/off valve with a maximum flow rate of $0.23lpm$, and a transition time around $1.5ms$ was implemented to precisely drive a hydraulic cylinder by Tsuchiya, et al. [17]. One valve that has a large flow rate ($100lpm$) and a fast switching time ($1ms$) was developed by Winker [18]. The high flow rate is achieved via an innovative spool stroke amplifier mechanism, which transforms a pilot armature's moving distance of $0.6mm$ into the spool stroke of $1.5mm$ via a lever gear. The actuation power is high due to large actuation force ($\approx 100N$).

In summary, the present state-of-the-art linear valves cannot have a small pressure drop across the spool for large flow rates, a short response time, and a low actuation power at the same time. This trend can also be found in the currently available commercial valves (e.g. Eaton DG4V3-2A, Parker A4D02-51, Sun DMDA, Rexroth RE22-045). One reason they cannot meet these requirements is that operating linear valves at high frequency requires the acceleration and deceleration of the spool or poppet during every on/off motion. To overcome the inertial force of the spool, an actuation power proportional to the PWM frequency cubed is required.

Rotary on/off valves

As a comparison to linear valves, rotary valves require much less power to operate at the same switching frequency, because the actuation power is only needed to overcome viscous friction, which is proportional to on/off frequency squared. In 1988, Brown et al. [6] proposed an externally driven rotary switching valve, which achieved $500Hz$ PWM frequency. The duty ratio is controlled by varying the angle between the control shaft

and stator. Similar designs were proposed by Lu et al. [19] and Royston [20]. The latter is a pneumatic valve. In 1990, Cui et al. [21] proposed a rotary based, single-stage, fast response digital valve. The spool rotary motion generates a force imbalance, which axially moves the spool between on and off positions. The valve achieved a response time of $2ms$, a flow rate of $18lpm$, and a pressure drop less than $9MPa$.

1.2.3 CFD analysis of valve design

CFD has been widely used in the design and optimization of hydraulic components, especially for control valves. The flow field visualization feature of CFD is used for identifying local flow phenomenon, which guides the valve flow path design process [22][23] and aids the analysis of certain valve properties (pressure drop, flow force, etc.) [24]. Given the computational cost constraint, control valve simulations are typically approximated using an axisymmetrical model [25] if possible. 3D simulations are required when the 3D turbulence induced by the intricate valve flow cannot be captured with an axisymmetric model [26][27]. However from accuracy's point of view, full 3D simulations can only predict the main flow dynamics and flow field distribution [28][29], because the detailed flow field prediction does not generally match with the experimental results well [27]. Good correlation of the CFD model to the detailed experimental measurements requires a significant amount of parameter tuning, and the simulation requires a large amount of cells and computational time. In addition, if the valve transient behavior is of interest, the computational cost increases. Such a comprehensive numerical model is not useful for quantitatively guiding the valve design or generating a quantified model for the hydraulic component optimization. If the design objective focuses on the general dynamics, a reduced order model is preferred [30], which can analytically model the valve flow pressure drop and flow forces as functions of the key valve parameters. Here reduced order refers to the reduced number of critical dimensional and material parameters. In our analysis, we also focus on developing a reduced order model, which can further be framed into solving for the valve geometry optimization problem.

1.2.4 Non-contact sensing methods

Currently, five types of non-contacting sensors are widely used, including LVDT, inductive sensors, ultrasonic sensors, magnetic sensors, and optical sensors.

`A linear variable differential transformer` (LVDT) is a type of electrical transformer used for measuring linear displacement. It consists of three solenoid coils placed end-to-end around a tube. The center coil is the primary, and the two outer coils are the secondary. An alternating current is driven through the primary, inducing a voltage in each secondary proportional to its mutual inductance with the primary. As the core moves, the mutual inductance changes, which changes the inducing voltage in the secondaries. The amplitude of the voltage is proportional to the displacement of the core. In our situation, to achieve the desired sensing range, the LVDT required will be long, which can potentially cause balancing issues with the valve spool.

`An inductive sensor` is an electronic proximity sensor, which detects a metallic object. An oscillator generates a fluctuating magnetic field around the winding of the coil that is located on the sensing face. When a metallic object is in the sensor's range of detection, the eddy current built up in the metallic object will interfere with the sensor's own oscillation field, reducing the strength of the oscillator. In this way, the distance between the sensor and the object will be monotonically mapped to the oscillator strength. In our situation, the spool is manufactured from steel, which meets the metallic object requirement. However, to achieve the long sensing range, the spool needs to have a diameter of $10cm$ or more to fit the sensor, which is not realistic.[1]

`An ultrasonic sensor` works on a principle similar to radar or sonar. It generates high-frequency sound waves and evaluates the echo which is received by the sensor. The distance is calculated via the time between sending the sound and receiving the echo. It is ideal for sensing uneven surfaces and clear objects. However, it is not applicable for the sensing range we are investigating. The desired sensing range is between $3cm$ and $6cm$, and the ultrasonic sensing range typically starts from $10cm$.[2]

`A magnetic position sensor` using Anisotropic Magneto-Resistive (AMR) sensors

[1] For example, BAW MKV-020.19-S4 Inductive Distance Sensor from Balluff Corporation has a range of $0 - 6cm$, which meets our requirement. However, the sensor size is $8cm \times 4.5cm \times 2cm$, which is too large for our application.

[2] For example: for SU Series Ultrasonic Proximity Sensors, the shortest range is $10cm - 60cm$, and it is one magnitude of order longer than the range utilized for our application.

is becoming a popular non-contact method to locate the objects in motion. By affixing a magnet or sensor element to an angular or linear moving object with a complementary sensor or stationary magnet, the relative direction of the resulting magnetic field can be quantified electronically. By utilizing multiple sensors or magnets, the capability of extended angular or linear position measurements can be enhanced. In our case, this approach is potentially feasible. However, this sensor requires special materials for the spool and sleeve, which may increase the manufacturing difficulty and cost.

`An optical sensor` refers to a sensor set including an optical emitter and a photodiode detector, which provides quantitative information about the position of an incident light beam or spot image. The structure of the sensor is relatively simple compared with the previous sensors, and the restriction on the valve material is low. Considering the sensing range, installation space constraint, and cost, we selected optical sensors for both angular and axial position measurement.

1.2.5 Hydraulic actuator position control

Electronically controlled hydraulic systems have been widely investigated due to the high power density from the hydraulic side and the flexibility in control from the electric side. However, the inherent dynamics of hydraulic systems exhibit high nonlinearity and uncertainties, which impose significant challenges on controller design.

Early research work focuses on converting the nonlinear systems into linear ones via linearization around certain operating points [31][32][33], or feedback linearization [34][35]. The corresponding linear systems can be manipulated using numerous well developed linear control techniques. However, linearization works well only within a small range around the operating points. Feedback linearization works well only when the nonlinear dynamics can be sufficiently modeled, accurately measured, and completely canceled. Therefore, these approaches typically trade control robustness and performance for computational cost. Local performance may be acceptable, but the lack of global stability may cause concerns.

In comparison, nonlinear controllers can typically achieve better performance with more robustly but computationally expensive control laws. Sliding mode controllers and backstepping controllers based on Lyapunov analysis have been broadly investigated in the application of hydraulic actuator control.

In a sliding mode (SM) control approach, a high order non-linear system can be converted into a first-order system, and then various control techniques can be applied, which typically lead to a very robust controller. Sliding mode control is implemented under the matching conditions, which means that the uncertainty shows up in the same state equation as the control input [36]. In a sliding mode controller, the trajectories are brought to a manifold in a finite time, and stay on the manifold once reaching it. Typically, the order of the controller is low, which is good for maintaining a low computational cost. However, the robustness of the controller is good only when dealing with the uncertainty that shows up in the same order as the control actions. To deal with the uncertainties that show up in higher order than the control action's order, other Lyapunov re-design techniques such as introducing nonlinear damping terms can be applied to increase the controller robustness. Another potential issue lies in the fact that sliding mode control is a variable structure control method, which means it is a discontinuous controller. When the system states are close to the trajectory (on the manifold), chattering may happen due to the finite sampling time. Approaches of introducing a smooth boundary layer can eliminate the chattering phenomenon [37]. Different versions of sliding mode controllers have been applied to hydraulic actuators for force tracking [38] and position tracking [39][40]. Sindery and Bone [41] used two position on/off valves to control one cylinder in a PWM manner. A feed-forward with position-velocity-acceleration feedback controller based on the system model was proposed and achieved good position tracking performance. By adding a sliding mode controller to increase the robustness of velocity error converging to zero, the control bandwidth was increased from $62.5Hz$ to $1000Hz$. To increase the robustness, integral control [42] and H-infinity controls [43] are added. In addition, a robust state observer in conjunction with the SM controller is proved to increase the robustness. The design of the observer and the controller is separated, and some unmatched uncertainties can be dealt with as well [44][45].

In comparison, a backstepping controller allows some model uncertainties in each order for a high order system, which inherently guarantees a more robust tracking performance. Backstepping is a recursive method for stabilizing the origin of a system in a strict-feedback form [36]. In each step, the next stage's state is treated as a "virtual" input, and the un-matching effect between the "virtual" and "true" inputs are passed to

the next stage to cope with. The procedure is repeated until the true control effort shows up, so that no more "virtual" input is used. Non-matched disturbances are allowed, and can be treated by the "virtual" input in each stage. To implement this approach on hydraulic actuator control, the first step is to design a desired hydraulic force (based on the passivity approach), and use this "virtual" input to stabilize the position (and velocity) tracking error. The second step is to stabilize the hydraulic force tracking error [46, 47]. In these approaches, a quadratic term of the hydraulic force tracking errors is used in the Lyapunov function, and the nonlinearities are canceled out to preserve stability. The physical energy associated with the actuator pressure dynamics is not considered. Since hydraulic systems exhibit parameter uncertainties and un-modeled dynamics, canceling the nonlinearities perfectly from the quadratic term is challenging. The residual part can degrade the overall control performance or even cause instability. This motivates the pursuit of a more robust Lyapunov function.

A passivity-based controller may be a more robust controller, because it utilizes the physical system's energy property to maintain the system's stability. Passivity property has been exploited in many nonlinear physical domains to derive robust control laws. One of the earliest domains was for electro-mechanical manipulators. Using the mechanical systems' physical energy functions and their modifications as Lyapunov functions, a passivity property (with mechanical power input being the supply rate) can be derived, and from which a whole class of fixed and adaptive control laws with rigorous analysis can be obtained (for example [48], [49]). This "energetic" passivity property of mechanical systems is a consequence of its Euler-Lagrange (or Hamiltonian) structure. Thus, with the success in the mechanical domain, controls that exploit the Euler-Lagrange or Hamiltonian structures have been developed for other domains as well (for example [50], [51]). In passivity-based controllers utilized in hydraulic systems, the passivity of the hydraulic valves have been considered in [52][53]. However, what determines the hydraulic force tracking error term in the Lyapunov function is the passivity of hydraulic actuators. Grabmair and Schlacher [54] proposed an energy based controller for a double ended hydraulic actuator actuated via a 4-way proportional valve. The port-Hamiltonian structure related to pressure dynamics is maintained via a special coordinate transformation. The corresponding invariants defined after coordinate transformation turned out to be the Casimir functions of the Port Hamiltonian

(PH) structure. A control strategy with different Casimir functions are exploited in [55]. Similar control logic is investigated in [56]. The similarities among these research projects can be summarized into two aspects. First, a constant bulk modulus model was assumed, whereas bulk modulus varies with pressure significantly, especially in low pressure operating ranges. Secondly, the derivation of the passivity is based on a special coordinate transformation, which mathematically provides the "hydraulic energy term" to define the Hamiltonian. However, the equation is not physically linked to the hydraulic energy stored in the fluid at a certain pressure. Li [57][58] specifies the compressible energy in the fluid at certain pressure and uses this energy term to define the Hamiltonian. This approach releases the constant bulk modulus constraint, and the only assumption is that the bulk modulus is a function of fluid pressure.

Model based advanced nonlinear controllers can be designed to guarantee certain robustness in the presence of uncertain, bounded dynamics. In hydraulic actuator systems, not all the constant parameters can be easily identified off-line. Some parameters vary slowly in real time as well. One solution to precisely capture the uncertainties is to introduce parameter adaptation with the control law. Both direct adaptive [47][59] and indirect adaptive nonlinear controllers [60] have been investigated rigorously. In a direct adaptive controller, all the parameter estimation update laws rely on the tracking errors. Due to the lack of a guaranteed persistent excitation (PE) condition, the parameters may not converge to the true values. In comparison, the indirect adaptive controllers can return a better parameter estimation. However, since the design of the controllers and the parameter update laws are separated, the only way to guarantee the effectiveness of the controller is to improve the parameter estimation, which again poses strict requirement of PE condition. If the unknown parameter appears in a nonlinear function, e.g. chamber volume in modeling the pressure dynamics, the parameter update law, and the controller will become even more complex [61].

One thing to notice is that nonlinear controllers typically require the feedback of all states. Directly feeding back the measurement may lead to a degradation in control performance due to noise. For example, if velocity or even acceleration are required for the control law, taking the direct derivative of the position measurement can introduce noise and phase lag. Therefore, we would like to build an observer and to implement the control law using the estimated states. In a linear time invariant (LTI) system,

where the separation principal applies[62], the design of the controller and the observer can be separated, and the controller can be implemented using the estimated states [62]. However, there is no such theorem for nonlinear systems. Although there is no general form as neat as the forms for linear systems, different versions of the nonlinear "separation principles" have been developed for different nonlinear systems. In general, the system consists of a nonlinear controller relying on full states feedback, and a high-gain observer [63][64][65].

In our system, to regulate the valve PWM duty ratio, we need to control the valve spool's axial position. Since the spool motion in the axial direction is actuated hydraulically, the pressure dynamics exhibits certain nonlinearities. To produce a robust spool axial position controller, a passivity based nonlinear controller was developed (in chapter 5). The spool axial position and velocity were estimated via a Kalman filter, and the states were utilized in feedback.

1.2.6 Displacement control configuration

Throttling losses across valves can drastically degrade the system efficiency, especially in the case where one power source drives multiple actuators operated at different load levels. As mentioned in section 1.1, one partial solution is to use a load sensing (LS) pump. However, there are two drawbacks with this approach. One drawback is that the throttling loss is only significantly reduced on the branch where the load pressure requires the highest pressure from the power source. Another drawback is the challenge to maintain the stability of an LS system [66].

In comparison, an approach that can ideally eliminate the throttling loss involves changing the way that flow is provided. Instead of throttling down the supply flow, we vary the supply flow. There are two principally different hydraulic circuit configurations to implement direct displacement control. One is an open circuit, in which the pump inlet and the actuator return line are connected to the hydraulic tank separately. The other one is a closed circuit, in which the actuator return line is connected to the inlet of the pump. In both open and closed circuits, the circuit and the control strategies should guarantee the following two performance criteria: i) actuator trajectory tracking; ii) the hydraulic circuit does not cavitate.

Typical hydraulic actuators are asymmetric (e.g. the piston rod is included on one

side of the actuator cylinder, but not the other). When using closed circuits, the unequal fluid volume needs to be compensated. Hewett [66] developed a closed circuit including a charge pump, an accumulator, and a 3-way 2-position shuttle valve, as shown in Fig. 1.6. The valve is actively controlled to connect a charge line to the low-pressure side when volume compensation is required. In this way, the charge pump and the accumulator guarantee that the pressure in the return line does not cavitate. For example, if the head side of the cylinder is the meter in chamber and the cylinder is extending under an over-running load, the shuttle valve will be operated in the position as shown in Fig. 1.6. The accumulator will supply fluid to the head chamber through the upper check valve. Both the pump and the accumulator will contribute to the meter in flow. If the cylinder is extending under a passive load, the shuttle valve will be shifted to its lower position. The meter out flow from the cylinder rod chamber will be combined with the accumulator flow through the lower check valve and the shuttle valve to feed to the inlet of the pump.

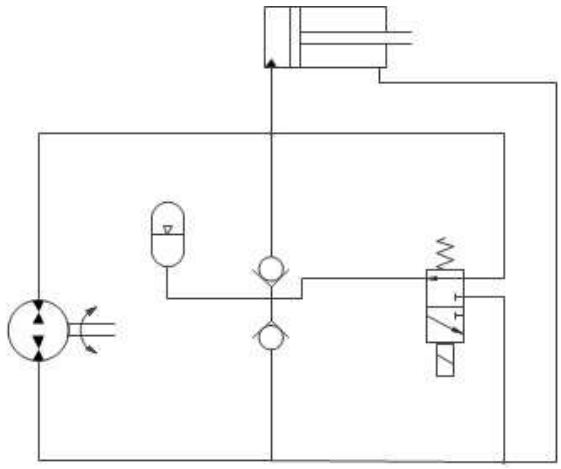

Figure 1.6: Displacement control closed circuit using a 3way shuttle valve [66]

Rahmfeld and Ivantysynova [67] proposed a different closed circuit where the charging line and the low-pressure side are connected via two pilot-operated check valves to compensate for the unequal volumes, as shown in Fig. 1.7. In closed circuits, extra components besides the variable flow source are required to compensate the unequal flow volume, which makes the circuit complex.

In contrast, open circuits yield a simpler configuration. Heybroek [68] proposed an

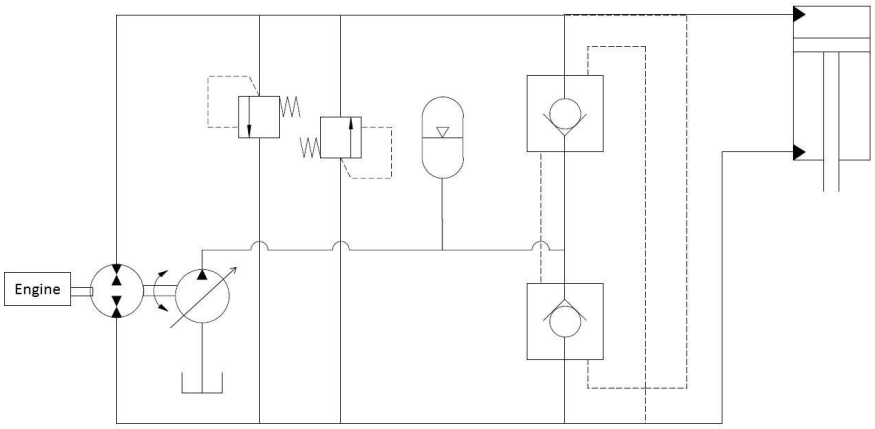

Figure 1.7: Displacement control closed circuit using pilot check valves [67]

open circuit, which includes a variable displacement pump/motor and four 2-way valves connected as a hydraulic H-bridge, as shown in Fig. 1.8. The circuit can realize four-quadrant operation. Since the pump can be operated as a motor, energy regeneration can be achieved.

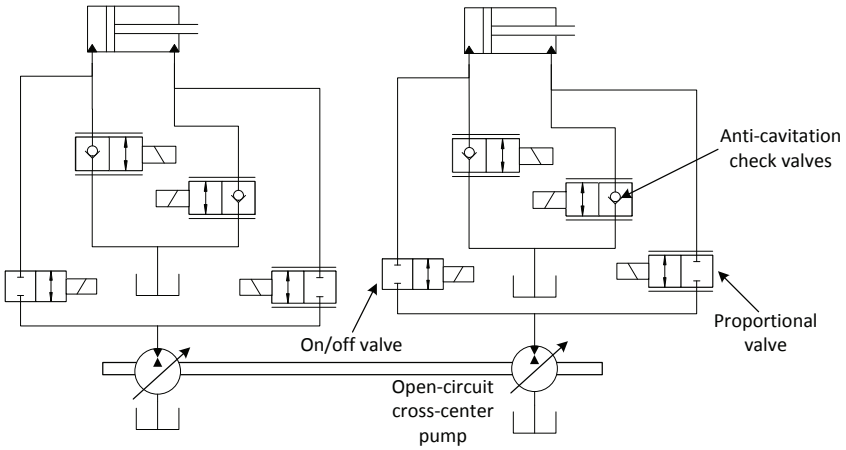

Figure 1.8: Simplified circuit diagram of the open circuit solution implemented on two drives [68]

All the circuits presented above require several components besides the variable displacement pump (motor) to achieve displacement control. Comparing between closed

and open circuit designs, the open circuit has an advantage of faster response time. We proposed an open circuit, which utilizes fewer and simpler components to achieve the similar function, as shown in Fig. 1.9. The circuit consists of a variable displacement pump, a 4-way directional valve, and a one-way proportional valve. The variable displacement pump is a virtually variable displacement pump (VVDP), which does not go over-center, so only positive displacement is provided. The 4-way valve is operated in an open-loop manner, so no valve position feedback is required. The proportional valve is coordinated with the pump to provide the control authority.

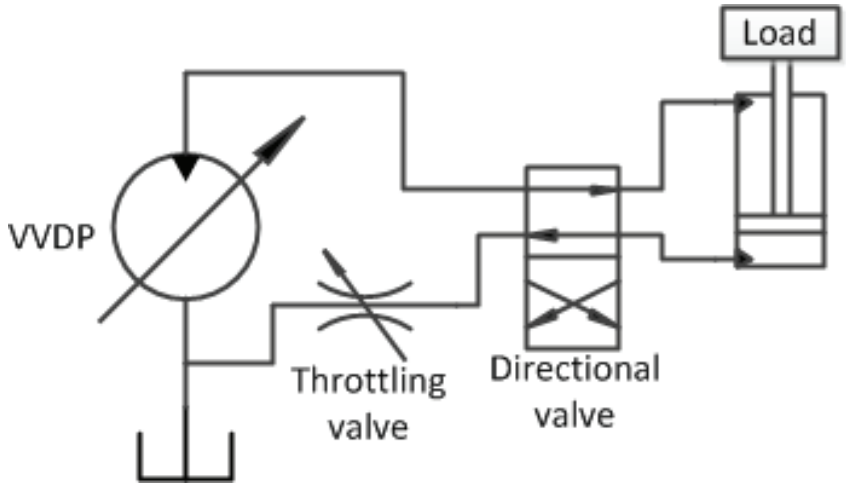

Figure 1.9: Direct displacement control open circuit using a VVDP

After the development of direct displacement control circuits, different control strategies have been investigated to manipulate the hydraulic actuators by implementing the circuit. Using the direct displacement closed circuits, Williamson and Ivantysynova developed linear controllers based on the linearized system [69][70]. Two operating modes are defined depending on if the load force is greater than the opposing forced on the piston or not. The analysis shows that there exists the potential of instability when the actuator switches operating modes, and the proposed solution is to increase system damping. Using the direct displacement open circuits, as proposed by Heybroek [68], the circuit (shown in Fig. 1.8) provides the authority to independently control the pressure in the meter-in and meter-out chambers, and to realize energy regeneration, which

achieves the actuator trajectory tracking performance, and prevents chamber cavitation in an energy efficient way.

1.3 Research scope

The dissertation focuses on 1) the loss analysis of the high-speed rotary 3-way on/off valve using CFD, 2) sensing, position estimation, and motion control development for the rotary valve spool motions, and 3) the implementation of the virtually variable displacement pump (VVDP) in a direct displacement control hydraulic circuit.

1.3.1 Scope 1

Since the efficiency of the rotary 3-way on/off valve directly affects the efficiency of the VVDP system, an optimal valve should be designed. The design method involves characterizing the operational losses as functions of valve geometries and operating conditions (flow rate, pressure, etc), and framing the valve design problem into an optimization problem to minimize the losses. Four valve losses are considered: fully open throttling loss, transition loss, compressible loss, and leakage loss [71]. Given the complicated flow path inside the valve, existing analytical formulas cannot fully characterize the valve losses. The flow inside the valve will be modeled using CFD. One purpose of the CFD analysis is to develop an analytical modeling of the 3-way valve losses. The other purpose is to design flow paths inside the valve that minimize throttling and compressible losses.

1.3.2 Scope 2

The valve spool can spin and translate axially inside the valve sleeve. The spool angular position is sensed using a set of non-contact optical sensors to simplify the valve sealing structure. The sensing range is relatively long ($\approx 2.54cm$), and the resolution of the sensor is low. The position measurement is detected at irregular time intervals. In this dissertation, we propose an event based Kalman filter, which can provide a continuous time estimate of the spool's angular position and velocity from event based measurements.

The valve spool's axial position is also measured using a set of optical sensors. The spool rotary motion corrupts the spool axial position measurement with structure noise. If the spool rotates at a constant speed, the structured noise is a periodic signal. The position feedback control relying on the corrupted spool position measurement degrades the spool position control precision. This dissertation proposes a periodic time varying model to capture the dynamics of the noise, so that the true spool position can be distinguished from the noise, and can be further used in the position feedback control. After estimating the correct spool axial position, a simple linear controller can be derived for spool position stabilization.

To improve the robustness of the spool axial position control performance, a passivity based nonlinear controller is developed that uses a novel pressure dependent fluid compressibility model to define the energy storage function. An energy function that quantifies the "energy" stored in the pressure error is proposed for pressure error regulation. The control law is to regulate the storage function to zero, and correspondingly bring the pressure error to zero. The new controller leads to robust control performance for the spool's axial position.

1.3.3 Scope 3

The last section of this research focuses on the system level control of a single hydraulic actuator. This research utilizes the VVDP described in Fig. 1.1 as a variable displacement pump (VDP) in a direct displacement control circuit, which is shown in Fig. 1.9. A passivity based nonlinear controller is developed to accurately control the position and chamber pressures of the actuator. A novel approach to distribute the control effort between the control devices (including the VVDP, a proportional valve, and a directional valve) is proposed. The approach distributes the control effort optimally between the VVDP and the proportional valve according to their control bandwidths. As a result, the valve is operated with a large mean opening area to reduce throttling loss, while the VVDP is operated following a slow varying profile.

1.4 Dissertation Structure

The rest of the dissertation is arranged as follows:

Chapter 2 presents the CFD analysis of the valve flow. Main results include the validation of the orifice equations in predicting the valve pressure drop; a semi-empirical formula developed based on the CFD results to predict the valve center PWM section pressure drop; and the local flow path modification.

Chapter 3 covers the valve spool rotary sensing and estimation. An event based Kalman filter will be presented to estimate the spool angular position and velocity.

Chapter 4 presents the first generation spool axial position sensing, actuation, and control system. The modeling of the structure-based measurement noise is described. The observability of the plant system augmented with the structured noise model is analyzed. In this generation, the valve spool self-spins, and the spool axial position is actuated hydro-statically using a small gerotor pump.

To improve the spool's axial position performance and to enable the investment of the effect of actuation strategy on valve efficiency, Chapter 5 describes the second generation of the spool driving system, which allows the spool rotary motion to be driven externally. Optimization results show that when the input flow rate through the valve varies, rotating the valve with an external actuator can produce higher efficiency than relying on self-spinning[72]. In the axial direction, the spool is treated as a single chamber actuated cylinder with a pre-loaded return spring. By manipulating the spool axial chamber pressure, we can vary the spool axial position. A passivity based nonlinear controller is developed for this new driving mechanism, which produces a robust and accurate spool position tracking performance.

Chapter 6 describes a direct displacement control, using a VVDP, to manipulate an open circuit double-ended hydraulic cylinder. The control efforts include the VVDP, supply flow to the cylinder supply chamber, a directional valve, and a proportional valve connecting the cylinder return chamber to the tank. A multi-mode controller is designed to enable the piston to track a reference trajectory. The multiple modes are defined based on the cylinder chamber pressures. The controller can guarantee a precise cylinder position tracking performance, and the cylinder pressures can stay bounded.

Finally in Chapter 7, the conclusion and the contributions of this research work are presented. The future research direction is discussed as well.

Chapter 2

CFD Analysis of a Rotary PWM Valve

2.1 Introduction

This chapter presents the CFD analysis to aid the design optimization of a rotary on/off valve. As discussed in chapter 1, the 3 way rotary on/off valve in the VVDP has four primary types of power loss: full-open loss, compressibility loss, leakage loss, and transition loss [71]. To facilitate the valve design, the loss metrics need to be linked to the design parameters analytically. In this way, the valve's key geometrical parameters and operating conditions can be framed as an optimization problem targeted at minimizing the overall valve losses. Given the complex flow path inside the valve, the pressure drop across the valve, which determines the valve throttling loss, cannot be fully modeled by orifice equations. Therefore, the semi-empirical relationship between the pressure drop, the flow rate, and the key valve geometry parameters is established based on the CFD analysis. The CFD tool is also utilized to facilitate the design of a smooth flow path inside the rotary valve.

To reduce computational cost, the fluid domain inside the valve when the inlet is connected to the load branch (or the tank branch) is divided into three parts, and each part is simulated independently. The valve spool uses turbines to gain angular momentum when the flow goes through it to spin the valve spool. The operating principle of the valve and the flow path inside it will be introduced in section 2.2, and the CFD

simulation set up will be described in section 2.3. The valve's pressure drop, flowrate, and geometrical parameter relationship will be investigated in section 2.4. The turbine torque analysis will be presented in section 2.5. The effective outlet turbine exit area will be identified from the CFD results. The CFD analysis validates the effectiveness of the analytical formula to model the pressure drop across the spool and to model the torque generated by the impulse and the reaction turbines. These equations are utilized for valve parameter optimization, which is discussed in section 2.6. Methods for improving the valve's interior flow path design based on the CFD analysis will be discussed in section 2.7. The modified design can minimize the compressible fluid volume within the valve without increasing its pressure drop. Compared with the prototype design, the valve's full-open throttling loss can be reduced by 62.5% and the compressible loss can be reduced by 66%. Finally, some concluding remarks will be summarized in section 2.8.

2.2 Rotary high speed on/off valve

The key geometrical parameters of the valve prototype are shown in Fig. 2.1. This section will first introduce the fluid domain inside the valve when the pump inlet flow is connected to the tank branch. Then, the experimental set-up of the high-speed rotary valve implemented in a virtually variable displacement pump (VVDP) circuit will be presented in sec. 2.2.2.

2.2.1 Fluid Domain Inside The Valve When it is Fully Open

The valve can be fully open from high pressure to load or from high pressure to tank. The fluid domain inside the valve at one instant, as shown in Fig. 2.2, corresponds to a spool position when the nozzle is connected to the tank branch. A similar domain can be illustrated with the nozzle connected to the load branch. The fluid inside the 3-way valve can be divided into three sections: the inlet toroidal pressure rail with nozzles, the center PWM section, and the outlet turbine with a toroidal pressure rail, as shown in Fig. 2.2. The detailed flow path is explained step by step.

First, flow supplied from the pump enters the toroidal pressure rail, which is shown in Fig. 2.3. This pressure rail is integrated into the valve sleeve to minimize the dead volume between the pump outlet and the valve spool. The rail splits the flow into three

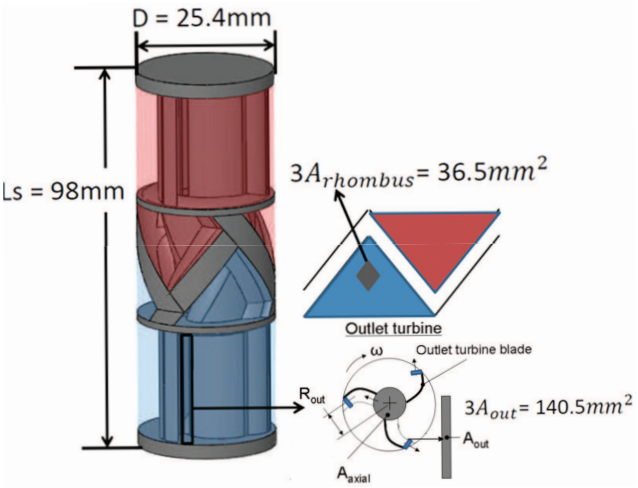

Figure 2.1: 3-way rotary valve prototype key geometry

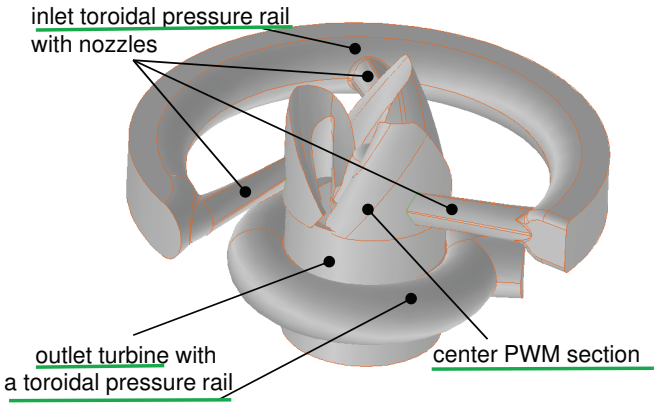

Figure 2.2: 3-way valve fluid domain (sleeve + half spool) when the inlet flow is connected to the tank branch

portions, and directs them into the center section of the valve spool tangentially via the three nozzles. Since the nozzles are tapered, the flows are accelerated before entering the spool's center section.

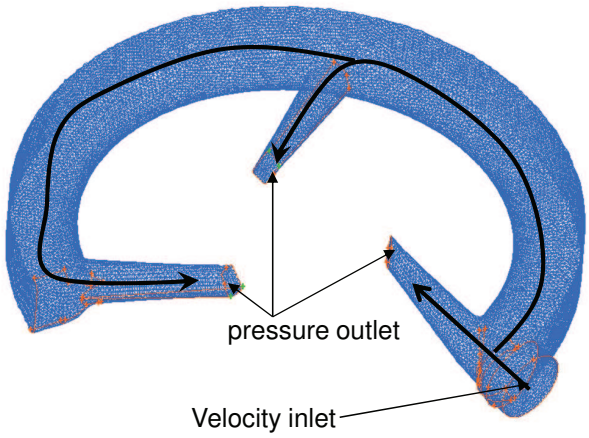

Figure 2.3: Inlet torus pressure rail with nozzles fluid domain

Second, as shown in Fig. 2.4, the flow that enters the center PWM section tangentially will be re-directed to travel axially before it exits the valve spool center PWM section. The difference in the angular momentum of the fluid between entering and leaving the spool center section imparts a torque on the valve spool, which causes the valve to spin.

Finally, as shown in Fig. 2.5, the flow enters the outlet turbine section axially, and leaves the turbine radially and tangentially. The outlet section is designed as a reaction turbine. The turbine blade guides the flow from traveling axially to tangentially, and a reaction torque is applied to the spool, which further aids the spool's self-spinning. As the flow approaches the outer edge of the turbine blade, the flow cross-sectional area expands. A toroidal pressure rail gathers the flow and guides it to the valve outlet.

2.2.2 Experimental apparatus

A prototype of the high-speed rotary valve described above has been designed and manufactured. This apparatus provides us with the experimental measurements to

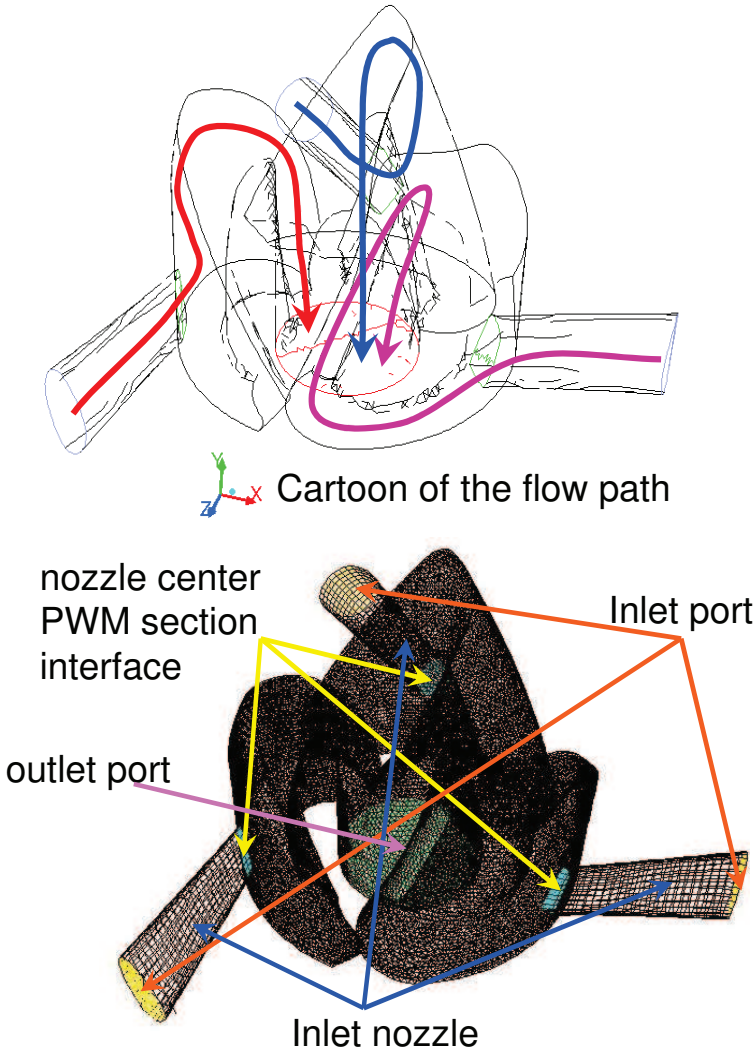

Figure 2.4: Center PWM section fluid domain

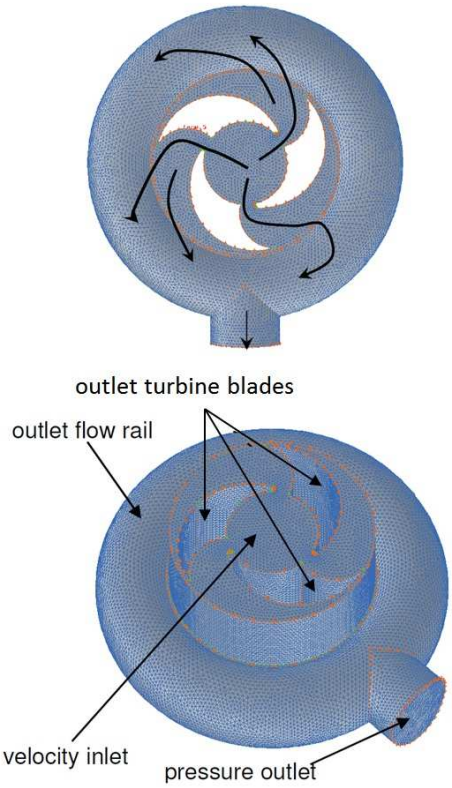

Figure 2.5: Outlet turbines with flow rail fluid domain

verify the CFD modeling and is shown in Fig. 2.6. The rotary valve is connected directly to the outlet of a fixed displacement vane pump via a customized pump housing. The vane pump has a fixed displacement of $22.8cc$, and is driven by a $5.6kW$ AC motor operated at $1800rpm$. A pressure sensor to measure the valve inlet pressure is mounted on the manifold between the pump and the valve. A load pressure sensor is mounted directly on the valve sleeve, which is at the outlet of the valve load branch. The pump provides a maximum flow of $40lpm$. The valve spool can be removed, so that the pressure drop across the valve sleeve can be measured. The flow rate into the valve can be adjusted by varying the AC motor rotary speed via varying the Variable Frequency Drive (VFD) driving frequency, and a flow meter is installed on the load branch. The flow passing through the load, which is an orifice, can be directly measured. Therefore, some operating points from the following CFD analysis can be compared with the experimental data. A relief valve is added in the circuit to provide protection during valve transition.

2.3 CFD simulation set up

Each section of the 3-way valve was created in a CAD modeler and was imported to the GAMBIT [73] pre-processor for geometry clean-up to remove unwanted geometric configurations such as short edges, cracks, and holes from the model. The fluid domain volume meshing and the boundary condition specification were also conducted in GAMBIT. Given the complex flow path, the tetrahedral element was selected as the main mesh element. The domain was simulated in FLUENT [74] on an IBM SP supercomputer. In this section, the governing equations used to model the flow inside the valve will be introduced first. Next, the boundary conditions for each sub-domain will be defined in section 2.3.1. Section 2.3.2 will summarize all the running cases we will investigate. The solution methods will be introduced in section 2.3.3, and the grid refinement procedure will be discussed in section 2.3.4.

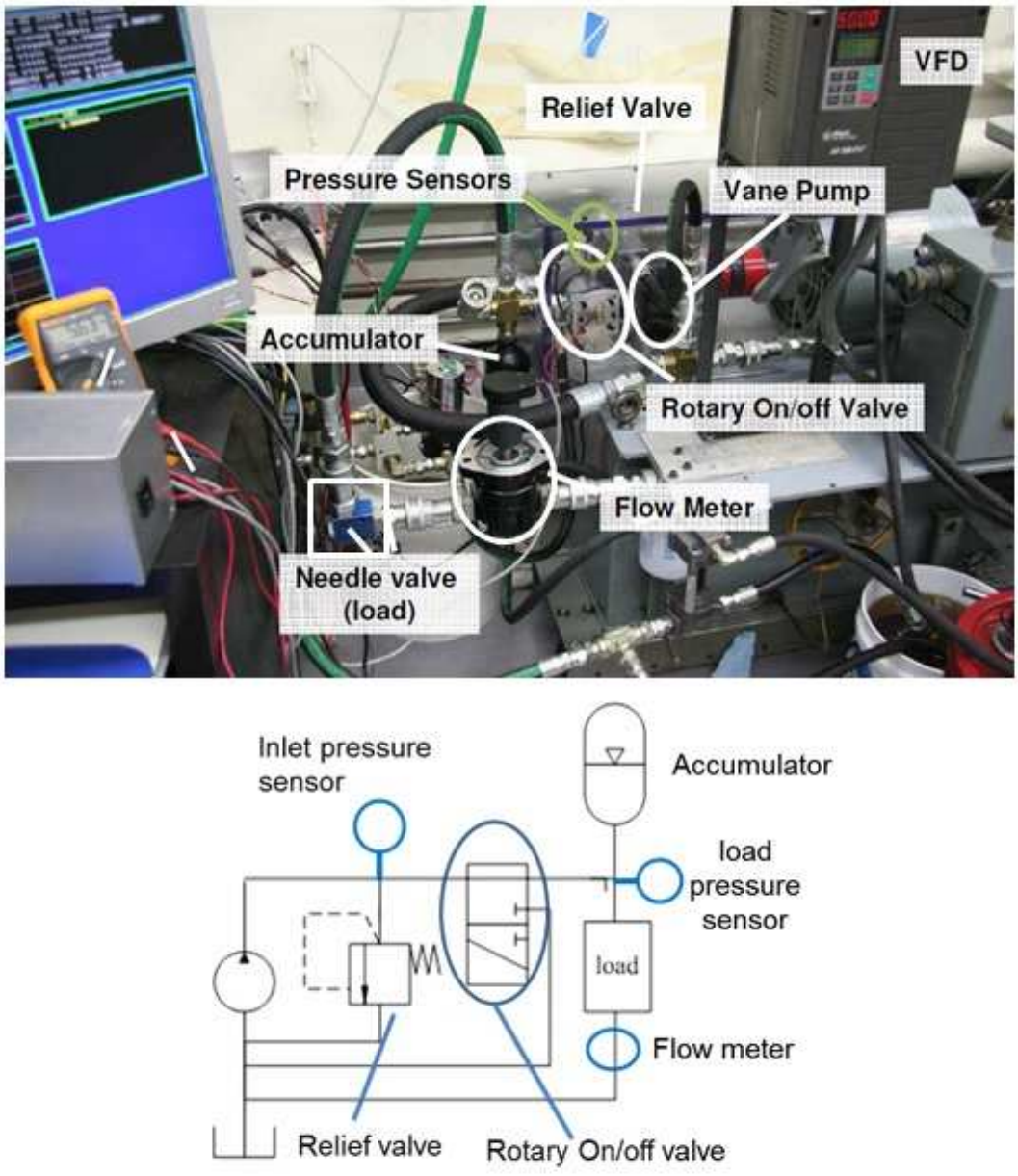

Figure 2.6: Experimental apparatus

2.3.1 Governing equations and boundary conditions

The governing equations describing the flow inside the valve when it is fully open are the incompressible Navier-stokes equations without body forces[75]:

$$\rho\frac{\partial\vec{v}}{\partial t}+\rho\vec{v}\cdot\nabla\vec{v}=-\Delta P+\mu\nabla^2\vec{v} \tag{2.1}$$

and the continuity equation:

$$\nabla\cdot\vec{v}=0 \tag{2.2}$$

where ρ is the fluid density, $\vec{v}$ is the fluid velocity vector, P is the fluid pressure and μ is the fluid dynamic viscosity. The fluid properties correspond to Mobile DTE 25, a common hydraulic oil that is used in the experiments. The density is $\rho = 876kg/m^3$, and the dynamic viscosity is $\mu = 0.0387kg/m/sec$, which corresponds to the temperature of $40°C$. The turbulent energy is modeled using the Reynolds-averaged Navier-Stokes (RANS) equations [74] method. The RANS equations are the time-average equations of the motion for fluid flow, which can be used with approximations based on knowledge of the properties of flow turbulence to provide approximate time-average solutions to the Navier-Stokes equations.

Each valve sub-section as described in Section 2.2 is simulated separately. For each sub-section, a constant pressure boundary condition is imposed at the domain outlet to provide a reference pressure. Pressures at the inlet are computed with respect to the specific outlet pressure. The inlet boundary condition is specified as a constant (in time) flow input. The flow is uniformly distributed on the inlet surface with a direction normal to the inlet surface. The no slip shear condition is imposed on all wall surfaces.

2.3.2 Simulated operating conditions

CFD was run for the prototype valve geometry with different input flow rates to estimate the pressure drop across the valve. Since the experimental measurement of the pressure drop across the prototype valve was conducted by holding the valve spool stationary, a stationary frame solver was used. To estimate the pressure drop across different sized valves, the prototype design was scaled radially while maintaining the spool length constant for the center PWM section. Different flow rates have been simulated for each

valve geometry to obtain the pressure drop across the center PWM section when the valve is fully open.

For the valve turbine torque analysis, the walls are stationary so that the fluid inside the three nozzles is not rotating around the valve spool's axial axis. In comparison, the fluid inside the spool center section is spinning around the spool's axial axis. A multi-rotating frame (MRF) model is utilized to capture the spool rotation effect. The resulting flow field from the MRF model is a representative snapshot of the transient flow field where the rotating parts are moving. The MRF model is a reliable tool to analyze rotating flows when the interaction between the rotating part and the stationary part is not significant.

2.3.3 Solution methods

Sharp edges and corners that exist in the flow path can lead to turbulent flow. A standard $\kappa - \epsilon$ viscosity model was utilized to capture this effect [28][30]. Density and velocity terms were discretized using the 1st order upwind method. The spatial gradient terms were solved using the least squares cell based method. The Semi-Implicit Method for Pressure Linked Equations (SIMPLE) was used for pressure-velocity coupling. These selections are well documented numerical methods for solving valve flow problems [74][28][29].

2.3.4 Grid refinement

In this section, we conduct the grid refinement analysis to identify the proper grid density at which the simulation results are independent of the grid density. The grid refinement simulations were based on a constant flow of $40lpm$, which was the maximum flow utilized in the experimental apparatus. The pressure drops across the three sub-sections described in Fig. 2.3 through Fig. 2.5 were simulated. The grid was refined using two methods. Since unstructured grids were used to mesh the fluid domain, the primary approach to refine the grid was to reduce the maximum allowable grid size. In addition, the grid density was increased at the locations where the pressure gradient was large. For each sub-section, the grid was refined until the pressure drop across the sub-section was independent on the grid density, as shown in Fig. 2.7 through Fig. 2.9.

Figure 2.7 shows the grid refinement analysis on the inlet toroidal rail and the inlet nozzles section described in Fig. 2.3. Figure 2.8 shows the grid refinement analysis on the spool center PWM section with inlet nozzles as shown in Fig. 2.4. Figure 2.9 shows the grid refinement analysis on the outlet turbine with the toroidal rail section described in Fig. 2.5. To balance the simulation precision and the computational cost, we refined the domain mesh locally. A pressure gradient based local grid refinement procedure was utilized. More mesh grids were introduced at the location where the pressure gradient was high.

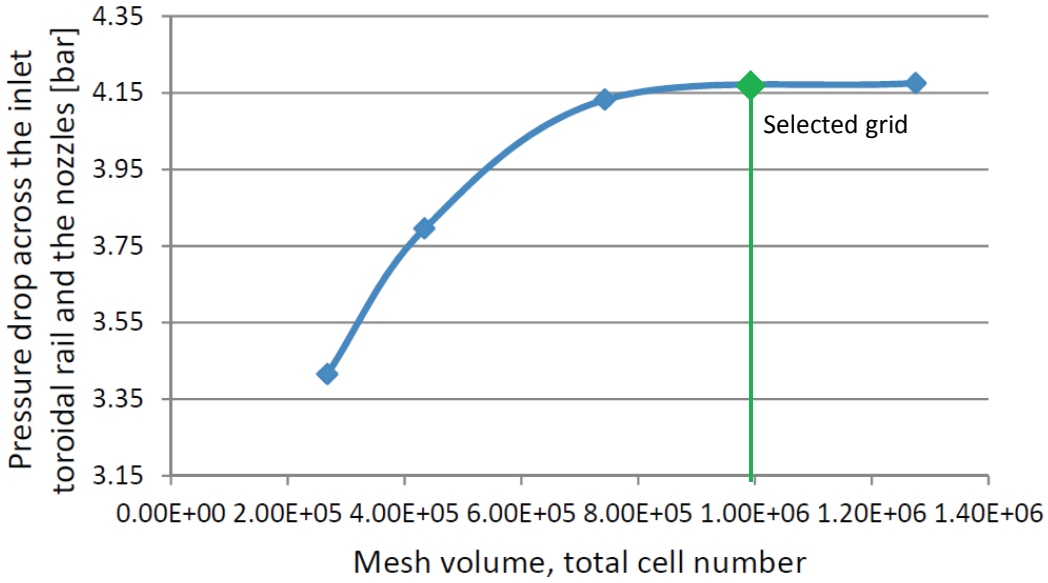

Figure 2.7: Grid independence analysis for the inlet toroidal rail and the inlet nozzles (as shown in Fig. 2.3) for a flow rate of $40 lpm$

Based on this analysis, the grid for the inlet toroidal pressure rail with nozzles domain contained 995983 cells. The nozzle with PWM domain contained 1018093 cells. The outlet turbine with toroidal pressure rail domain contained 1772910 cells. The refined domains were used in the following simulations.

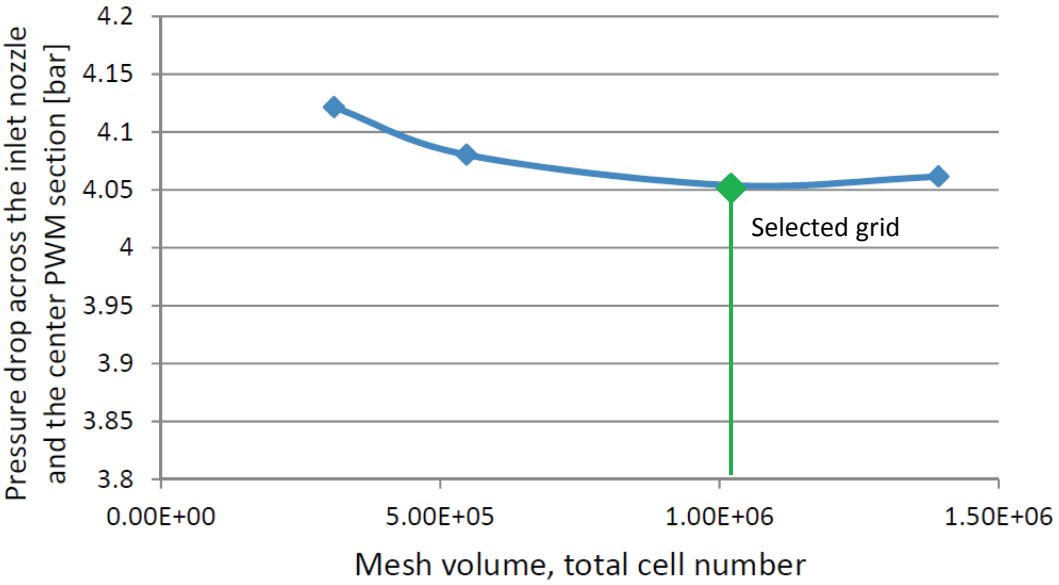

Figure 2.8: Grid independence analysis for the center PWM section with inlet nozzles (as shown in Fig. 2.4) for a flow rate of $40lpm$

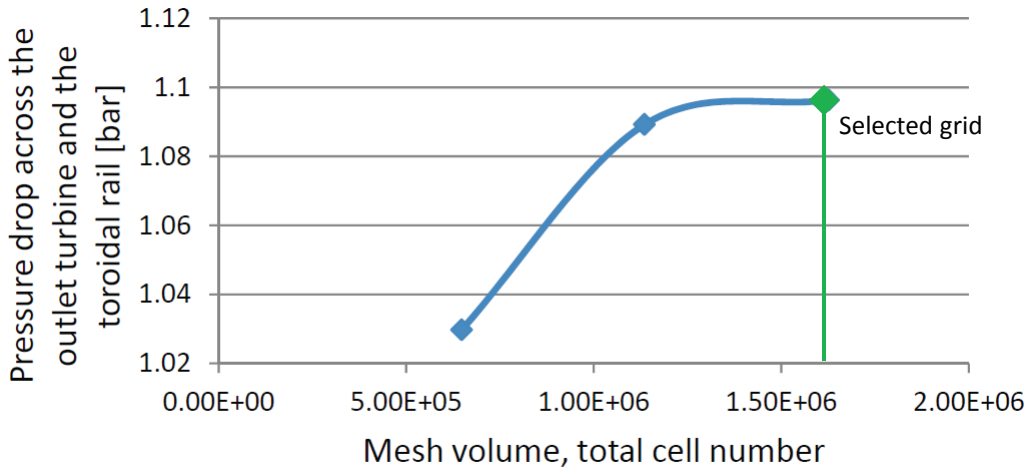

Figure 2.9: Grid independence analysis for the outlet turbine with the toroidal rail (as shown in Fig. 2.5) for a flow rate of $40lpm$

2.4 Full open pressure drop

In this section, we present the full open pressure drop CFD results across each subsection of the domain shown in Fig. 2.2. Full open pressure drop refers to the configuration when the nozzle is not partially blocked by the spool helical barriers. For the inlet toroidal rail with nozzle section (Fig. 2.3) and the outlet turbine with toroidal pressure rail section (Fig. 2.5), CFD was run for the base geometry at different flow rates, and the pressure drop across the section was obtained. For the center PWM section, the prototype spool is scaled only in the radial direction to generate different geometries, as shown in Fig. 2.10. The candidate geometries had the same height but different spool diameters. For each geometry, flow rates from $10lpm$ to $80lpm$ were simulated to obtain the pressure drop across the center PWM section. The pressure drops across the prototype valve at different flow rates were measured experimentally, and the CFD results were compared with the experimental measurements.

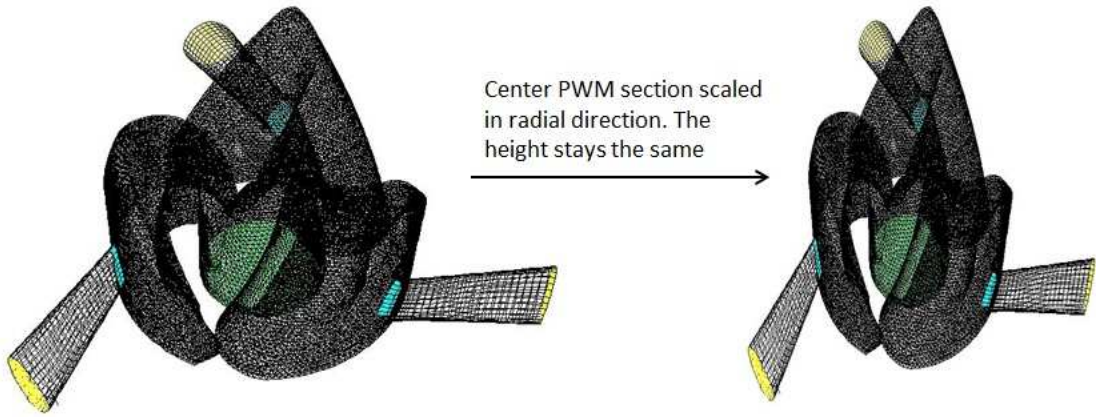

Figure 2.10: The valve spool's PWM section is scaled in radial direction to generate prototypes of different geometry for CFD analysis

The pressure drop across the three sections of the rotary valve from both the CFD analysis and the experimental results are presented in Fig. 2.11. The first figure shows that for the pressure drop modeled across the whole valve (including sleeve and spool), the pressure drop predicted by the CFD model matches with the experimental data very well. However, the correlation between the CFD prediction and the measurement for each separate section is not as good. In the second figure, it is shown that CFD

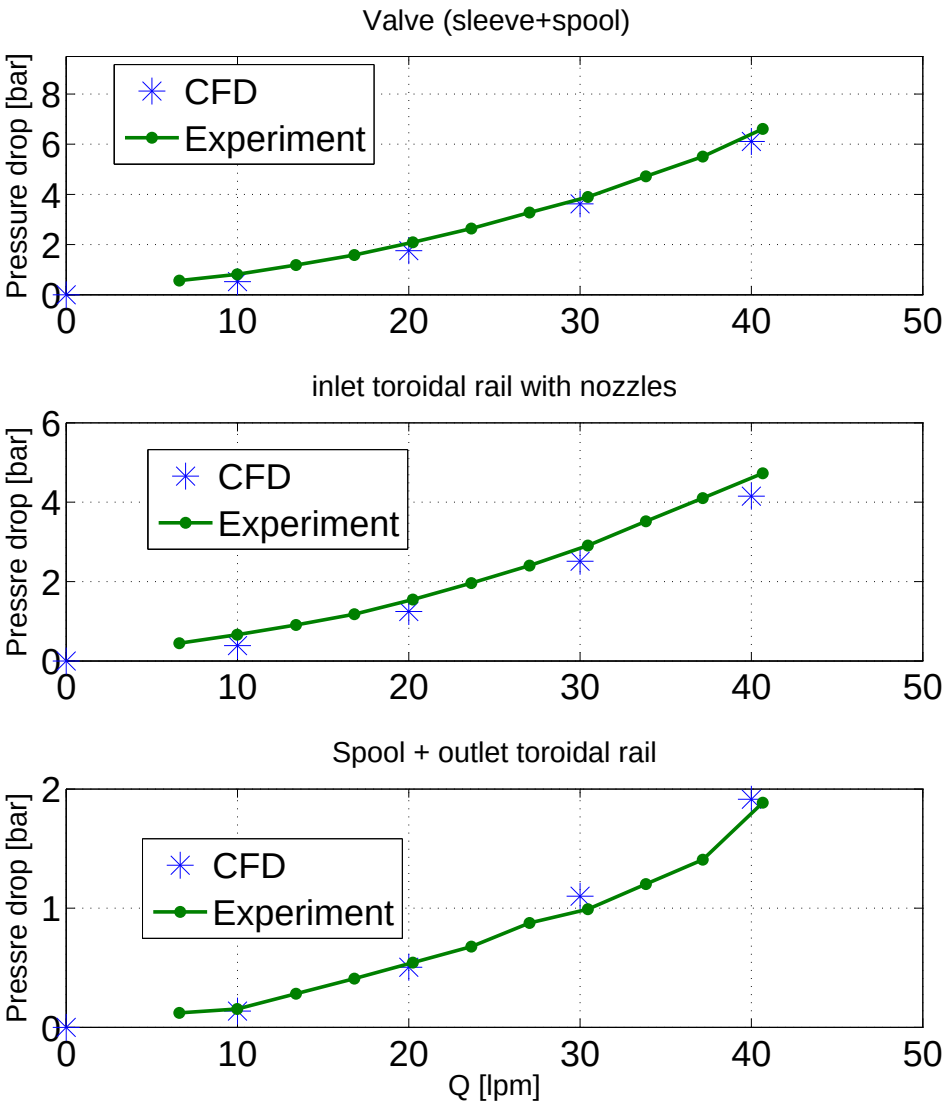

Figure 2.11: Comparison of valve pressure drop between experimental and CFD results. Top: pressure drop across the valve, including both the sleeve and the spool, as shown in Fig. 2.2. Middle: pressure drop across the inlet toroidal rails with the 3 nozzles, as shown in Fig. 2.3. Bottom: pressure drop across the spool and the outlet toroidal rail, as shown in Fig. 2.5.

predicts a $0.1bar$ lower pressure drop than the experimental data for the inlet toroidal rail with nozzles section. Ideally, we would like to compare the CFD results with the measurement at different positions within the flow path. However, since the pressure sensor cannot be located arbitrarily within the valve, we cannot measure the pressure at the inlet and the outlet surface for each sub-section. We can measure the pressure drop across the whole valve, which refers to the fluid domain shown in Fig. 2.2 The pressure drop across the inlet toroidal rail with nozzles section can be approximated by removing the spool from the valve. In this case, the pressure sensor is located on the sleeve, rather than at the nozzles' exits. Therefore, some extra pressure drop caused by the sleeve bore is included in the pressure drop measurement of the inlet toroidal rail with nozzles from experimental measurement, and the CFD prediction for the inlet toroidal rail with nozzles section is lower than the experimental measurement. The good match between the CFD simulation results and the experimental measurements shows the effectiveness of the CFD model. This enables us to analyze the valve pressure drop section by section via the CFD simulation instead of direct measurements. Next, we will use CFD to facilitate the development of analytical equations to predict the pressure drop across each sub-section defined in section 2.2 given a flow rate.

2.4.1 Pressure drop across the inlet toroidal rail with nozzles

The pressure drop across the inlet toroidal rail with nozzles is obtained via CFD for various flow rates, and the results are shown in Fig. 2.12.

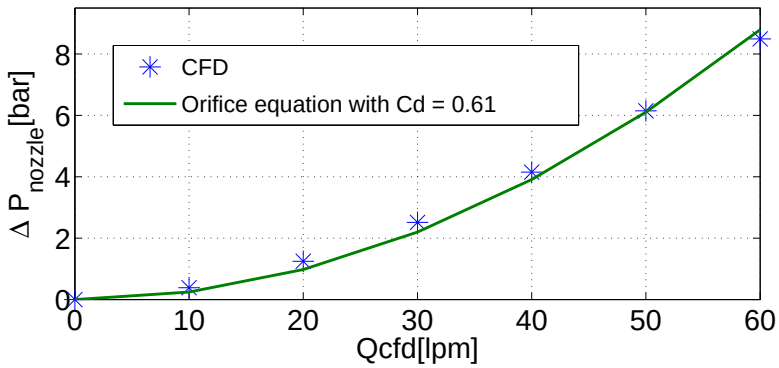

Figure 2.12: Pressure drop across the inlet toroidal rail with nozzles

From the CFD results, we observe that the pressure drop vs. flow relationship exhibits a parabolic curve trend. This means that the orifices are effectively modeled using the standard orifice equation:

$$\Delta P_{nozzle} = \frac{\rho}{2}\left(\frac{Q_{in}}{C_{d,in}A_{rhombus}}\right)^2 \tag{2.3}$$

By treating the three nozzles as one cumulative orifice, the total orifice area is $A_{rhombus} = 36.5mm^2$. The discharge coefficient $C_{d,in} = 0.61$ was calculated through a least square fit of the CFD predictions. A discharge coefficient $C_d \in [0.6,\ 0.7]$ is typically assumed for orifices [76], since the results show good agreement with expectations.

2.4.2 Pressure drop across the center PWM section

This section will present a model of a modified orifice equation to analytically predict the pressure drop across the valve center PWM section. Given other geometry constraints, the length of the spool cannot be varied much. Therefore, we impose an assumption that the equivalent flow path area depends on the spool diameter only. The baseline geometry (shown in Fig. 2.4) was scaled radially. In this way, the depth of the fluid pocket increases proportionally with the spool radius and the helix angle changes. Different flow rates were simulated for each scaled valve to obtain the pressure drop across the center PWM section, and the results are shown in Fig. 2.13.

The pressure drop across the prototype design was used as a pressure reference; the pressure drop across the various geometries (varying D) with different flow rates (varying Q) was modeled using a modified orifice equation. Since the flow path includes both a pipe portion and an orifice portion, a modified orifice equation is proposed to quantify the relationship between the pressure drop across the valve:

$$\Delta P = \frac{Q_{in}^m}{k_{center}D^n} \tag{2.4}$$

where k_{center} is a constant parameter. The boundaries of m and n are determined from a pure pipe flow equation, and a pure orifice equation: $m \in (1, 2)$, and $n \in (2, 4)$.

For each spool candidate, the pressure drop across the domain was simulated for a range of flow rates. The results are shown in Fig. 2.13. A plane was fit to the simulation data using the least squares fitting method to determine k, m, and n, as shown in the

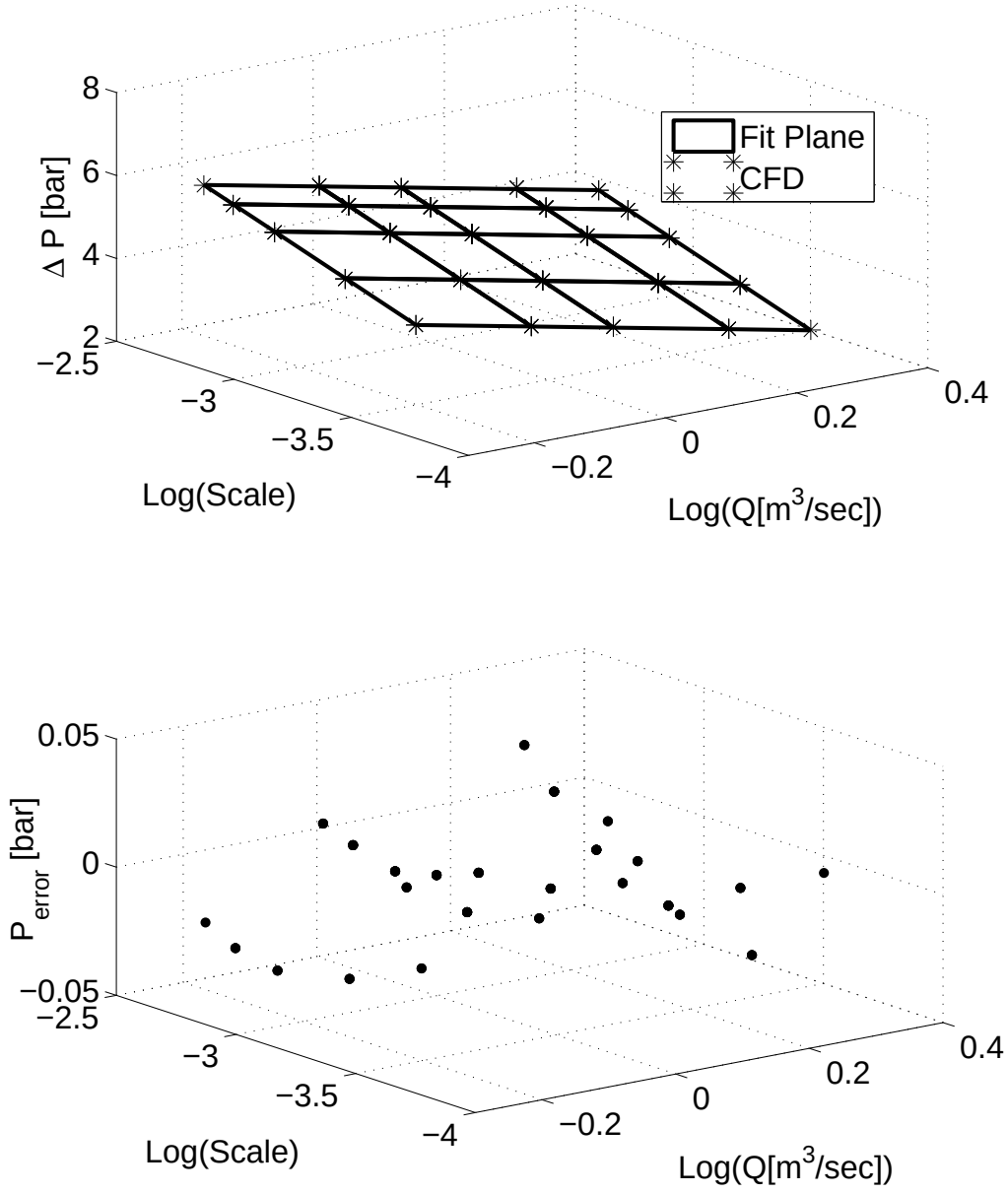

Figure 2.13: Pressure drop vs. flow rate and spool geometry scaling for center PWM section (top); pressure drop estimation error (bottom)

upper figure of Fig. 2.13. The parameters are estimated to be $m = 1.91$, $n = 3.22$, $k_{center} = 1.45 \times 10^{-6}$. $m = 1$ corresponds to a pipe flow model and $m = 2$ corresponds to an orifice flow model. Since m is close to 2, it means that the flow across the center PWM section has the attributes of an orifice. The fitting errors are shown in the lower plot of Fig. 2.13, and the maximum fitting error is less than $0.05bar$, which shows the effectiveness of the analytical model in predicting the spool center PWM section pressure drop.

2.4.3 Outlet turbine with the toroidal pressure rail

The pressure drop across the outlet turbine with toroidal pressure rail section (as shown in Fig. 2.5) was simulated for flows from $Q_{in} = 0lpm$ to $Q_{in} = 60lpm$ for the baseline geometry. This domain is analyzed in two parts. One part is the pressure drop across the outlet turbine. The other part is the pressure drop across the toroidal pressure rail.

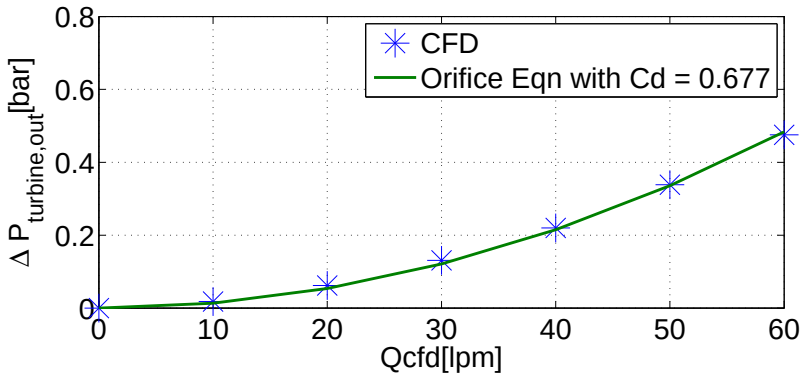

Figure 2.14: Pressure drop across the spool outlet turbine

The pressure drops at different flows across the outlet turbine are shown in Fig. 2.14. We observed that the pressure drop vs. flow curve exhibited a quadratic shape, and therefore the pressure drop across the outlet turbine with the toroidal pressure rail section was assumed to follow the orifice equation:

$$\Delta P_{turbine,out} = \frac{\rho}{2}\left(\frac{Q_{in}}{C_{d,out}A_{out}}\right)^2 \tag{2.5}$$

The outlet turbine's exit area ($A_{out} = 46.8mm^2$, as shown in Fig. 2.1) is identified as the orifice for this domain, and the assumption is that when flow exits the outlet turbine of the spool, flow directions are perpendicular to the exit cross area. The discharge coefficient in the orifice equation was calculated by the least square fit to the CFD data, and $C_{d,out} = 0.677$.

The pressure drops across the toroidal pressure rail at different flow rates by CFD are shown in Fig. 2.15. The pressure drop vs. flow relationship across this part does not need to be modeled analytically. The purpose of the analytical model is to be used in a valve parameter optimization framework to determine the optimal balance between the throttling loss and the compressible loss. Fluid inside this part is not compressed at the PWM frequency, so only throttling loss (pressure drop) needs to be considered for this section. Therefore, enlarging the flow path to reduce the throttling loss does not result in the penalty of an increased compressible volume. To reduce the throttling loss, the flow path can be designed to be as large as possible, subject to the geometric and the manufacturability constraints.

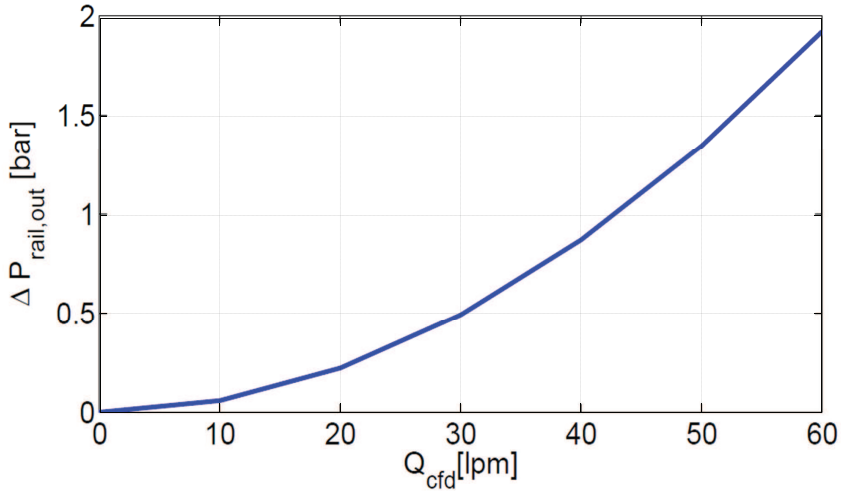

Figure 2.15: Pressure drop across the outlet toroidal pressure rail

2.5 Torque and speed

The rotary valve spool is designed to self-spin without an external driving mechanism. When the valve spool spins, the only resisting torque comes from the viscous friction force, which is proportional to the spool rotary speed. The spool's rotary motion is driven by the torque generated by the impulse and reaction turbines that correspond respectively to the inlet and outlet sections of the valve. When the turbine torque balances the friction torque, the spool will rotate at an equilibrium angular velocity, which determines the PWM frequency. Analytical formulas for predicting the turbine torques using a control volume method were developed in [77], and are reviewed below. CFD can be used to assess the accuracy of the analytical equations, and determine any modifications to the formulas which are required.

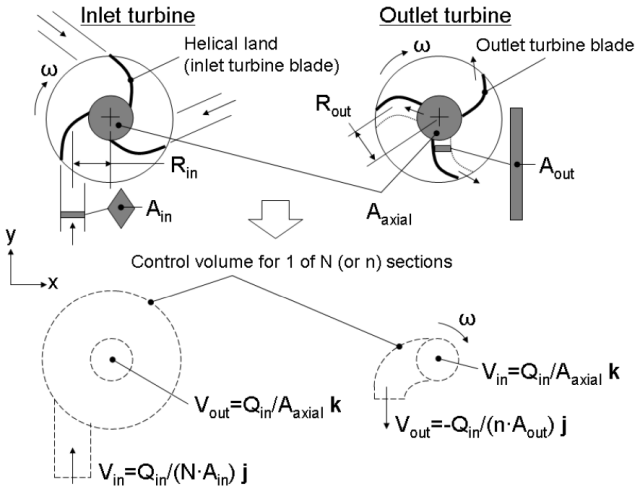

Figure 2.16: Impulse turbine and reaction turbine [77]

The control volumes for both turbines are shown in Fig. 2.16. For the inlet turbine (the center PWM section), the flow enters the valve spool tangentially, and leaves the control volume axially. The change in angular momentum of the fluid results in a torque being applied to the turbine. The mean velocity of the fluid as it enters the spool is denoted by v_{in}, and the mass flow rate is denoted by $\dot{m}$. The inlet turbine torque is

modeled as:

$$\tau_{in} = \sum_{1}^{N} (R_{in} v_{in}) \dot{m}_{in} = \frac{\rho R_{in}}{A_{in} N} Q_{in}^2 \tag{2.6}$$

where ρ is the density of the hydraulic oil, and R_{in} is the constant distance offset from the axis of rotation when the fluid enters the control volume. Q_{in} is the volumetric flow rate at the inlet of the control volume. $N = 3$ corresponds to the three inlet nozzles to the control volume.

For the outlet reaction turbine, the flow enters the turbine axially, and leaves the spool tangentially. The flow area when the fluid leaves the blade is assumed to be a constant distance R_{out} offset from the axis of rotation (Fig. 2.16), and the turbine torque is modeled as:

$$\begin{aligned} \tau_{out} &= \sum_{1}^{N} R_{out} \cdot (v_{out} - v_{CV}) \cdot \dot{m}_{out} \\ &= \frac{\rho R_{out}}{A_{out}} Q_{in}^2 - R_{out}^2 \rho \omega Q_{in} \end{aligned} \tag{2.7}$$

where A_{out} is one effective flow exit area near one turbine blade. $v_{CV} = R_{out}\omega$ is the velocity of the flow at the tip of the blade where the fluid exits the control volume.

These torque prediction formulas are compared with CFD. In this analysis, the multi-rotating-frame model was used instead of the stationary model to capture the effect of a constant turbine rotational velocity. This analysis was done for the scenario in which the valve was fully open, not in transition. In the CFD model, the turbine torque about the rotation axis was computed by summing the moment of the pressure force vector $\vec{F}_P$ and viscous force vector $\vec{F}_v$ for each mesh cell, with its moment arm $\vec{r}$. The vector $\vec{r}$ is pointing from the rotation axis to the force origin of the evaluated mesh cell:

$$\tau_{CFD} = \sum_{mesh\ cell} \vec{r} \times \vec{F}_P + \vec{r} \times \vec{F}_v \tag{2.8}$$

Figure 2.17 shows the torque analysis results. For the inlet turbine, the CFD simulation results match the predictions from Eqn. (2.6) very well, indicating that it can effectively be used to model the torque generated by the impulse turbine.

For the outlet turbine, the effective area A_{out} was calculated via least square fitting of the CFD simulation results, which produced $A_{out} = 61.8mm^2$. Since flow at the exit

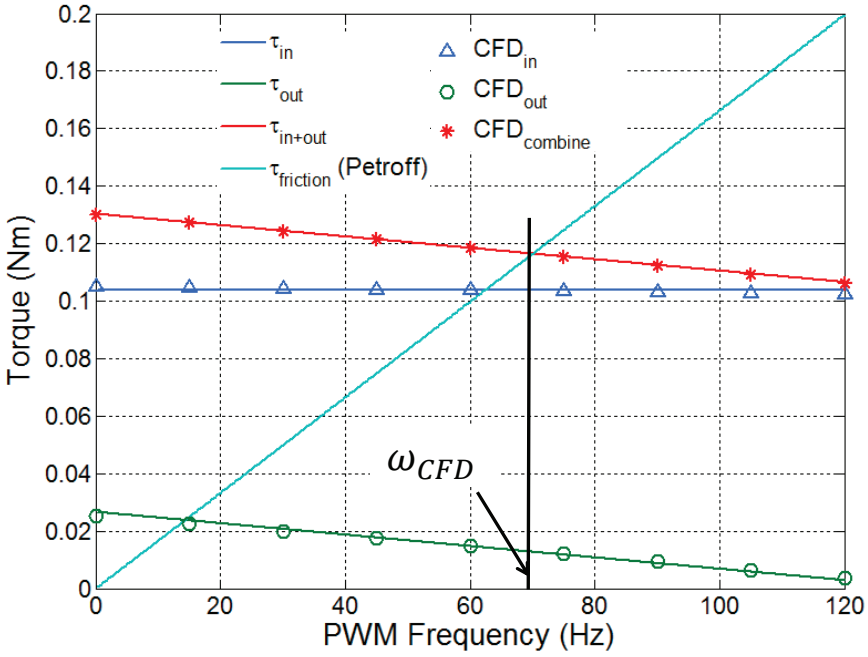

Figure 2.17: Torque predicted from CFD and analytical formula

was not a uniformly distributed flow normal to the exit area ($A_{out} = 46.8mm^2$) shown in Fig. 2.1, the effective exit area should be larger than the one read from Fig. 2.1.

Next, we will evaluate the valve spool speed. The spool self-spins at the angular speed at which the turbine torque equals the viscous friction torque. The friction torque is modeled with an analytical equation following Petroff's law[78]. The assumption here is that the fluid is Newtonian. The friction torque is modeled as:

$$\tau_{friction} = A_{surf} \frac{\mu}{c} R^2 \omega \tag{2.9}$$

where A_{surf} is the effective bearing surface area of the spool. This effective bearing area accounts for both the bearing surface area and an equivalent "bearing area" to model the viscous drag of the fluid inside the enclosed pocket, as shown in 2.18. The detailed modeling of the bearing surface is presented in [79], section 2.3.4. μ is the oil dynamic viscosity at $40\,\mathrm{deg}\,C$, ω is the spool angular velocity, and c is the clearance. Since the valve radial clearance is one thousandth of the spool radius, the friction force moment arm is approximated by R, which is the radius of the valve spool.

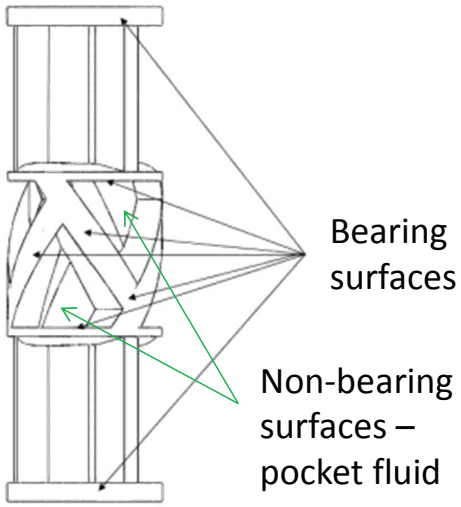

Figure 2.18: Valve bearing surface and pocket fluid, account for equivalent bearing surface

Figure 2.17 shows that the total torque generated from the turbines and the friction torque intersect at $72Hz$ PWM frequency, which corresponds to $24Hz$ spool rotational frequency based on the analytical formula with the parameters of A_{out} identified from CFD analysis. The experimental data measured the valve to operate at a PWM frequency between $70.4Hz$ and $82Hz$ depending on the oil temperature. In conclusion, analytical equations are valid to predict the torques generated by both the impulse and the reaction turbines of the valve.

2.6 Optimization of the valve design

The formulas presented in Eqn. (2.3), Eqn. (2.4), Eqn. (2.6), and Eqn. (2.7) are utilized in optimizing the 3-way valve [71]. The orifice equations Eqn. (2.3) and Eqn. (2.4) model the throttling losses of the valve, which are used in the cost function of the valve optimization. The objective of the optimization is to minimize the valve operational losses. The torque formula Eqn. (2.6) and Eqn. (2.7) are used to establish the rotary valve speed constraint in the valve optimization. The optimization variables include the spool radius R, the valve inlet nozzle area A_{in}, the valve outlet turbine exit's area A_{out}, and the valve spool/sleeve radial clearance c. The optimization results predict that for

the same flow capability ($40lpm$), the full open pressure drop across the optimized valve using the designed equations would be $2.48bar$. Compared with the current prototype, which has a full open pressure drop of $6.61bar$, a reduction of 62.5% on pressure drop can be achieved. Equivalently, the throttling power loss of the valve can be reduced by 62.5%.

2.7 Guidance to the inlet toroidal rail design improvement

Since the valve operates at high PWM frequency, in addition to the throttling loss, the compressibility loss also contributes to a significant portion of the valve's operational loss. During every PWM period, energy is required to compress the fluid to a high pressure, P_{high}, in the inlet volume, V_{comp}. This energy is lost when the high-pressure flow is connected to the tank, and the loss $L_{compress}$ is proportional to the valve compressible volume (V_{comp}) [71]:

$$L_{compress} = V_{comp} \frac{P_{high}^2}{2\beta_{eq}} N \frac{\omega_{pwm}}{2\pi} \tag{2.10}$$

Where $\omega_{pwm} = 3\omega$ refers to the valve's operational PWM frequency. The fluid bulk modulus, β_{eq}, is typically several thousand bar. The compression happens very fast, and the energy cannot cause any noticeable temperature change to the oil. In other words, no significant heat exchange happens in the oil due to this pressure change. Therefore, the energy equation is not used in CFD. Although "compressible volume" is used to refer to the volume, this volume mainly affects the dynamics of the VVDP during transition when the pressure inside this volume is compressed from low pressure to high pressure or vice versa. Here, to analyze the pressure drop across this volume when the fluid is passing the volume at its steady state, we still use an incompressible solver.

It would be ideal to keep the compressible volume as small as possible. However, making the flow path too small increases the pressure drop across the corresponding domain, which increases the valve throttling loss. How to balance between the reduction in fluid volume and the reduction in pressure drop is investigated using CFD tools. The fluid volume considered in this section includes the inlet toroidal pressure rail and the three nozzles, as shown in Fig. 2.3. Given the orifice area as a constraint, the objectives of the CFD modeling are to reduce the fluid volume, maintain or reduce the pressure

drop, and maintain the uniform flow distribution among the three nozzles compared with the prototype design.

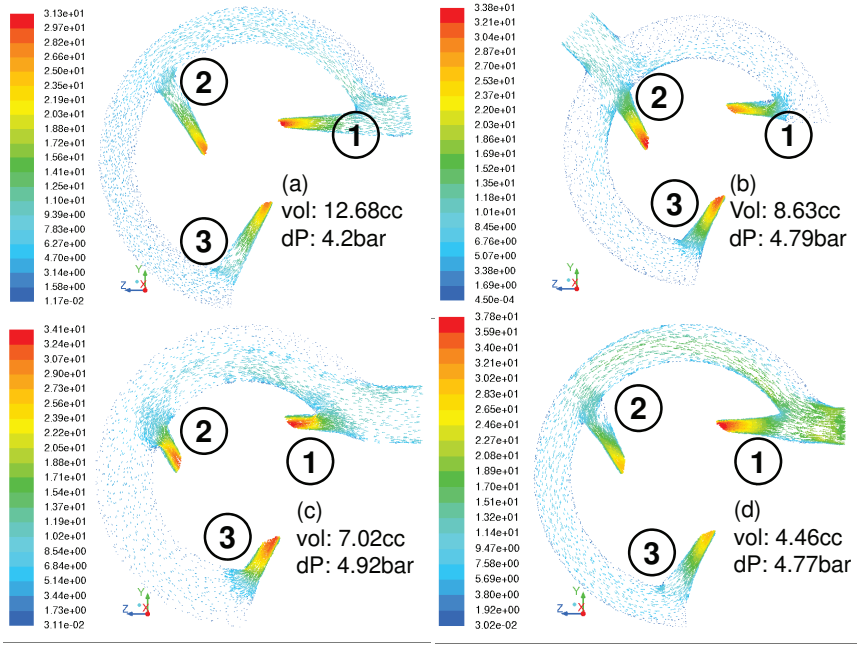

Figure 2.19: Examples of the inlet pressure rail improvement (a) prototype design; (b) inlet port moved to the center; (c) shorten the nozzle length so that the toroidal rail diameter is reduced by 16% ; (d) shrink the toroidal cross section diameter by 30%

We identified three changes which can potentially decrease the valve compressible volume: 1) moving the inlet port to the middle of the channel that supplies flow to the three orifices; 2) reducing the cross-sectional area of the toroidal flow channel; 3) shortening the nozzle length to reduce the toroidal diameter. Figure 2.19 shows the effects of each design change. Figure 2.19a shows the prototype design. In Fig. 2.19c, the nozzle length is shortened so that the toroidal rail diameter is reduced by 16%. In Fig. 2.19d, the cross-sectional diameter of the toroidal flow channel is reduced by 30% compared with the prototype. The fluid volume inside the toroidal rail of the prototype is 12.7cc (shown in Fig. 2.19a). The smallest potential design can reduce the fluid volume inside the toroidal rail to 4.2cc (shown in Fig. 2.19d). This corresponds to a 67% reduction on the compressible loss. In comparison, the pressure drop (or the full-open throttling loss) is increased by 13.6%. Since each change results in some reduction

of the compressible fluid volume, we created an optimized design by combining the three changes.

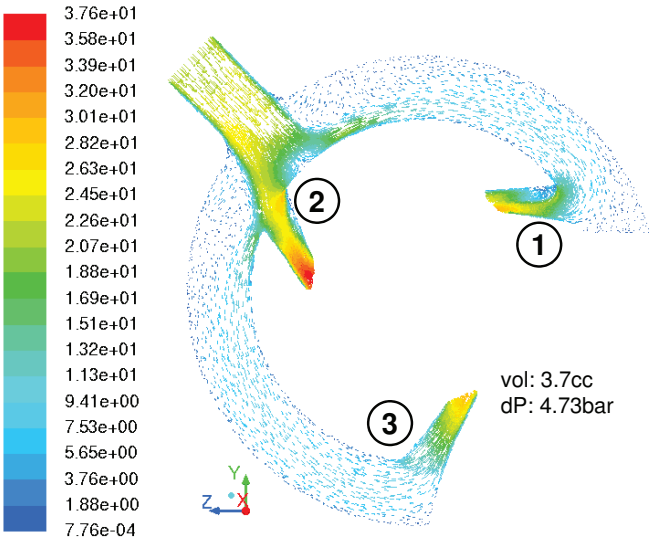

Figure 2.20: An optimized toroidal rail design

	(a)	(b)	(c)	(d)	final
1	35.5%	32.8%	38.6%	34.1%	31%
2	32.3%	35.0%	30.5%	32.1%	38.6%
3	32.2%	32.2%	30.9%	33.8%	30.4%

Table 2.1: Flow distribution among nozzles. Cases (a)(b)(c)(d) are defined in Fig. 2.19. "final" refers to the design shown in Fig. 2.20

Compared with the prototype, the new design shown in Fig. 2.20 has a shorter nozzle, an inlet that is moved to the center of the toroidal rail, and a smaller rail cross-sectional diameter. The new rail has a fluid volume of $3.7cc$, while the pressure drop for a $40lpm$ flow is $4.73bar$. This is comparable to the pressure drop of the prototype, which is $4.17bar$. The volume reduction is equivalent to a 66% reduction of the compressible loss.

The flow distribution results among the three nozzles are presented in Table 2.1. The final design does not produce as even a flow distribution as design(b) or design (d). In the final design, the pressure rail guides more flow to nozzle 2, because nozzle 2 is located closer to the inlet compared with nozzle 1 and nozzle 3. While the unbalanced flow

distribution among the three nozzles can potentially create an unbalanced radial force on the spool, the magnitude of the flow mismatch (8%) leads only to a negligible imbalance radial force on the spool. For example, when a $40lpm$ flow is passing through the valve spool, at its steady state, the unbalanced radial force is $0.93N$. Since the fluid between the valve spool and the valve sleeve functions as a journal bearing, this unbalanced radial force can be handled by the bearing. Therefore, although the flow distribution of the optimized design is not as uniform as the prototype, it is still acceptable. CFD has successfully enabled reducing the compressible volume while maintaining a similar pressure drop across this domain and a uniform flow distribution.

2.8 Summary

In this chapter, the flow inside a novel high-speed rotary on/off valve has been analyzed using CFD. CFD validated and aided the development of analytical equations which predict the valve pressure drop and the valve turbine torque as a function of geometrical design parameters. The analytical equations can be further utilized in the valve parameter optimization. Compared with the current prototype valve, the optimized valve can reduce the fully open loss by 62.5%. An improved optimized design of the inlet pressure rail with nozzles was established via CFD. The fluid volume inside the valve inlet pressure rail and the nozzles was reduced by 66%, while the pressure drop was only slightly larger (6.7%). The analysis can be extended to the design of any high-speed digital valves, where compressible loss counts for a large portion of the valve operational losses, and the balancing between compressible loss and throttling loss is important. The approach of developing a semi-empirical formula to predict the pressure drop for the center PWM section of the valve spool can also be extended to the analysis of similar valves in developing a reduced order model to predict the valve pressure drop analytically.

Chapter 3

Event based Kalman filter for valve spool rotary states estimation

3.1 Introduction

In this chapter, the valve spool angular states (angular position and velocity) sensing and estimation problem will be addressed. The self-spinning feature of the rotary valve prefers non-contact sensing to measure the valve spool rotary position. Non-contact sensors can simplify the valve sealing structure, and they can avoid the interference between the sensor and the valve spool motion (in both rotary and axial directions). The valve spool angular position is measured using a non-contact optical sensor, which consists of a laser module, a photodiode and a rotary encoder, as shown in Fig. 3.1. The light emitted from the laser is reflected from a code wheel attached to the spool end. The photodiode outputs a high-low alternating signal, depending on whether the laser light is reflected off of a black or reflective (metal) sector on the code wheel. Changes in the photodiode response are used to sense the spool angular position. Due to the small spool diameter ($25.4mm$) and the relatively large laser beam spot size ($5mm$ in diameter), the encoder resolution is relatively poor (8 sectors per revolution). Improving the quality of the laser source can permit the usage of a high resolution code

wheel, therefore improving the sensing resolution. However, it is expensive to realize this improvement.

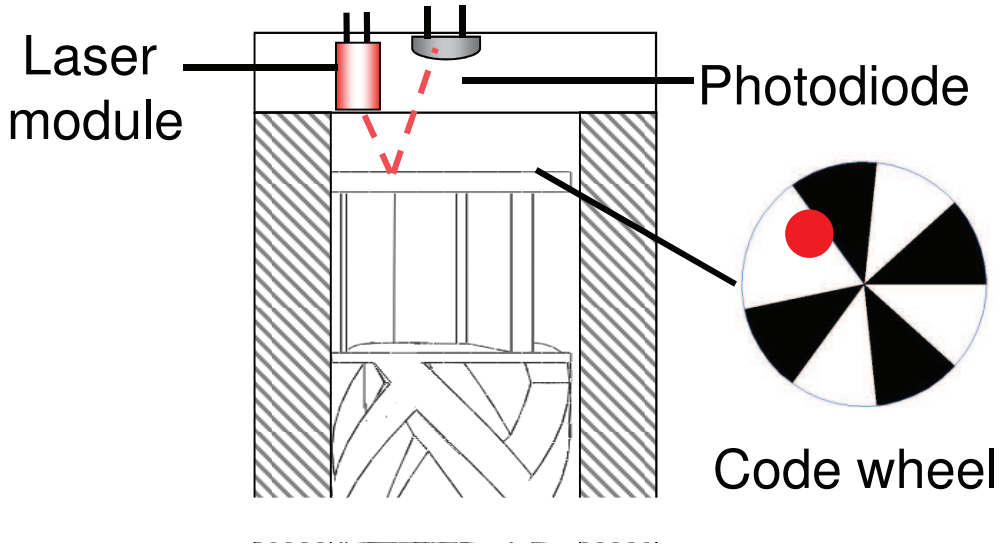

Figure 3.1: PWM valve rotary sensing mechanism

Two approaches have been frequently used to estimate the angular velocity from encoder measurements, depending on whether the angular velocity is high or low: finite difference method [80] and inverse-time method [81][82]. If the angular velocity is high, the finite difference method is preferred, where the angular velocity is calculated by counting the number of pulses within a fixed time interval, converting the counts to angle, and dividing the angle by the time interval. If the angular velocity is low, the inverse-time method is preferred, where the angular velocity is calculated by dividing the sector angle by the time between successive pulses.

If the sampling frequency is relatively slow, and the encoder resolution is low, the measurement of pulses will be obtained at irregular time instants. Both approaches will produce noisy estimations of the angular states. The performance of both finite difference estimators and inverse-time estimators can be improved by adding additional low pass filters to either pre-process the position signal (integration of the encoder), or to further filter the estimated velocity. Depending on the assumption of the noise model that is corrupting the position measurement, optimal estimators can be achieved

to estimate the velocity from the position measurement. Glad and Ljung [83] presented a Kalman filter to estimate the angular velocity, and the measurements of the angular positions are obtained at irregular time instants. The measurement, as presented in [83], can be obtained from light response changes when holes on a disc mounted on the axis pass through light source. The uncertainty of the occurrence time was converted to measurement noise, and a linear time-invariant (LTI) system with a zero mean measurement noise is derived. The corresponding estimator design can follow a typical Kalman filter design procedure. Simulation results show that the Kalman filter approach is superior to both the finite difference method and the inverse-time method.

In our problem, because the encoder resolution is very low, it is beneficial to also estimate the angular position and velocity between transitions of the encoder counts. Since the measurement of black-white transition events can occur at irregular times, we propose an event based Kalman filter observer for this purpose. When the sampling intervals are large, the uncertainty in when the transition occurs becomes more uncertain. The transition events are subject to uncertainty due to finite sampling interval, the fact that the optical signal changes gradually and the threshold for distinguishing a white or black sector is uncertain. Continuous time, time-varying Kalman filter theory is adopted to accommodate the uncertain event based measurements. The resulting algorithm is such that between events, the Kalman filter operates in an open loop manner; when a transition is detected, both the Kalman filter gain and the state estimate are updated discretely. Compared with Glad and Ljung's work in [83], our work provides the additional data estimation in between the sampling times.

In the next section, the rotary sensing working principle will be introduced. In section 3.3, the two sources of noise which corrupt the encoder measurement on event detection time will be described. The system modeling will be presented, focusing on formulating the time uncertainty to a measurement noise on position. This formulation is important to derive an LTI system model. The proposed event based Kalman filter will be introduced in section 3.4 to estimate the states of the LTI system. Finally, the simulation validation and the experimental validation of the event based Kalman filter will be presented in section 3.5 and section 3.6.

3.2 Optical rotary sensing

The sensing mechanism for the rotating spool is shown in Fig. 3.1. The rotary optical sensor consists of a laser diode light source module, a photodiode and a code wheel with black sectors printed on a piece of transparent media. The code wheel is attached to one end of the spool. A low power laser module and a photodiode are mounted next to each other on one end of the sleeve. The code wheel is designed to include a small number of sectors and an index sector. As the spool rotates, the laser beam reflects off of either a black or a white (metal) sector, causing a measurable alternating signal from the photodiode. In our case, the spool has a small diameter ($2.5cm$), and the distance between the laser beam and the encoder is about $2.54cm$, which is much larger than a typical distance between a light emitter and its receiver ($< 3mm$). As a result, the laser spot on the encoder is quite large. Under such circumstances, a low resolution code wheel (8 sectors per revolution) is required to ensure that the laser spot ($\approx 5mm$ in diameter) lies completely within in one code sector ($\approx 8mm$).

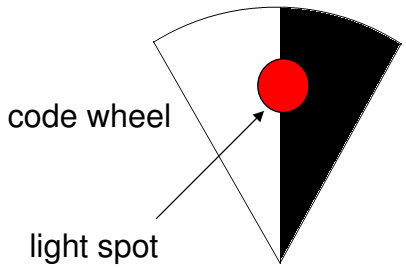

Figure 3.2: Ideal measurement detection

We define the situation when the center of the laser light spot overlaps with the code wheel sector boundary as a "transition event". The time when this "transition event" happens is defined as the occurrence time of the "transition event". When the light spot crosses the code wheel edge (as shown in Fig. 3.2), the output of the light receiver will change. Ideally, the photodiode outputs a discrete binary signal, as shown in Fig. 3.3, so that when a "transition event" is detected, a measurement of the spool angular position is received. In reality, a real photodiode output does not produce a perfect square wave signal with sharp edges. Instead, the sensor output will be discretized by comparing

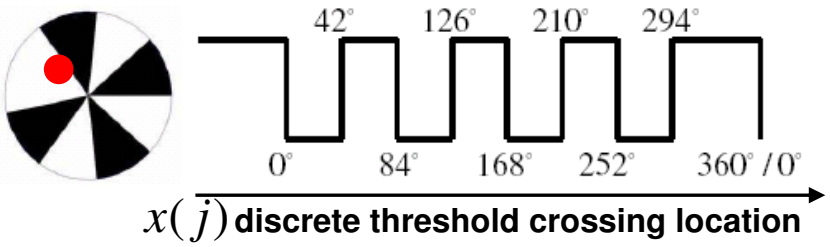

Figure 3.3: Ideal rotary encoder output

its value to a threshold value to generate the signal with sharp edges. Moreover, the acquisition system of the sensor measurement is run in a discrete time manner, so that the "transition event" cannot be detected until the next sampling time after the "transition event" occurs. Both the discretization of the analog photodiode output and the discrete time nature of the data acquisition introduce noise on the measurement of the "transition event" occurrence time.

First, we describe the "transition event" occurrence time noise caused by the photodiode signal discretization. The analog measurement from a realistic photodiode exhibits a pattern similar to the upper figure from Fig. 3.4. The raw signal is discretized by comparing its value to a threshold value. If the raw signal is greater than the threshold level, a high signal (1) is output; if the raw signal is lower than the threshold, a low signal (0) is output. The sharp edges of the discretized sensor measurement represents the occurrence of the event that the center of the light spot crosses the code wheel edge. The event that the center of the light spot crosses the code wheel edge is defined as a "transition event". The instant when a "transition event" occurs is defined as the "occurrence time" of a "transition event". A "transition event" will be captured by the sensor's output, when the discretized sensor measurement alternates. The instant when the sensor output alternates is defined as the "switching time" of the "transition event". This switching will be acquired when the sampling occurs, and the sampling time after the discretized sensor measurement alternates is defined as the "detection time" of the "transition event".

The discretization of the analog optical sensor measurement relies on the threshold value. The "switching time" of a transition event will differ from the "occurrence time"

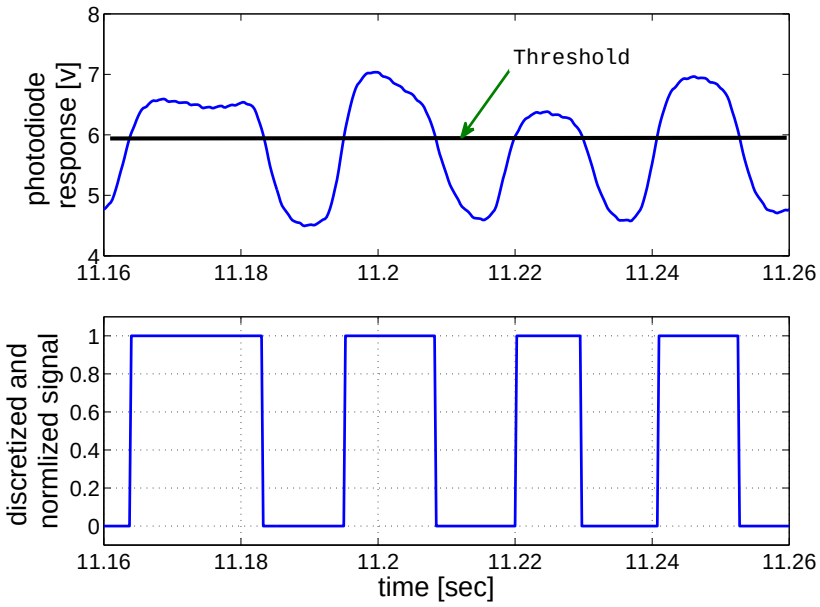

Figure 3.4: Raw (top) and discretized (bottom) signal from the photodiode.

of the transition event, if the threshold is not set correctly. Figure 3.5 shows how the setting of the threshold value affects the discretization of the photodiode output, and further affects the "switching time" of the "transition event". If the threshold value is set to be lower than the true value the transition event detection time will be delayed from the transition event occurrence time, but if the threshold value is set too high, the detection time will be advanced compared with the occurrence time.

The other measurement noise of the "transition event" occurrence time comes from the discrete time nature of the data acquisition. Since the sensor output is received at a finite sampling frequency, all the sensor information is communicated with the controller or the data acquisition system at one sampling instant. Therefore a "transition event" will be detected at the next sampling time after its occurrence. A low sampling frequency can cause a large error on the timing between the the occurrence time of the "transition event" and its measurement.

In the next section, the uncertainties of timing on the measurement of the "transition event" occurrence time will be modeled mathematically by converting the time

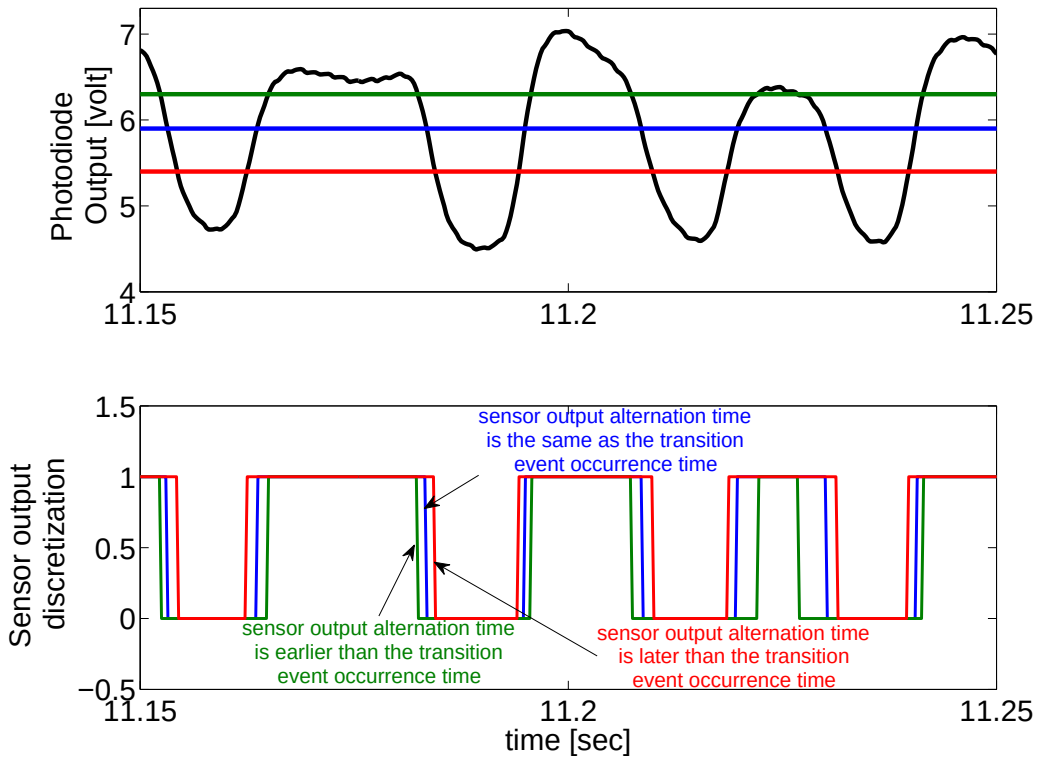

Figure 3.5: Effect of threshold bias on transition event detection. Top: photodiode measurements in black line and three thresholds denoted by green, blue, and red lines respectively. The threshold in blue is at the correct value, the threshold in green threshold is greater than the correct value, and the threshold in red is lower than the correct value. Bottom: discretized sensor measurements correspond to the three thresholds

measurement noise into a spool angular position measurement noise.

3.3 System modeling

As introduced in chapter 1, by utilizing the spool impulse turbine to capture, and the reaction turbine to convert the fluid flow moment into spool angular momentum, the turbine torque varies monotonically with the valve flowrate. On the other hand, the viscous friction torque is proportional to the square of the spool's angular velocity. Therefore, given a constant valve flowrate, the spool will rotate at a constant angular velocity at which the turbine torque is balanced by the viscous friction torque. Since in our prototype set up, the rotary valve is connected to a fixed displacement pump operated at a fixed speed, the flow through the valve is constant ($40lpm$), and therefore, the spool can be modeled as a cylinder rotating at a constant angular velocity. Any acceleration effect is modeled as a process noise d. d is assumed to be a zero mean, normally distributed noise. The spool angular position is denoted as θ, and the angular velocity is denoted by ω. The system is modeled as:

$$\frac{d}{dt}\begin{pmatrix}\theta\\ \omega\end{pmatrix} = \begin{pmatrix}0 & 1\\ 0 & 0\end{pmatrix}\begin{pmatrix}\theta\\ \omega\end{pmatrix} + \begin{pmatrix}0\\ 1\end{pmatrix}\cdot d(t) \tag{3.1}$$

The measurement of the spool angular position is denoted by y. The measurement is obtained from the detection of the "transition event". Since the edge between the black and white sectors on the code wheel is indexed, y refers to the measurement of the sharp edge when the "transition event" occurs.

The continuous time model is discretized at a sampling frequency of $\frac{1}{\Delta T}$, where ΔT is the sampling period. Let the uniform sampling time be $t_k = k\cdot\ \Delta\ T,\ k = 0,\ 1,\ 2,\ \cdots$. Fig. 3.6 illustrates the definitions of the sampling time, the transition event occurrence time, and the transition event detection time. We denote the sampling period as ΔT. The occurrence time of a transition event is denoted by τ_j^*. The "detection time" of a transition event is denoted by t_k. For the case shown on Fig. 3.6, the jth "transition event" is detected at sampling time t_k. The $j-1\ th$ "transition event" occurs at time τ_{j-1}^*, and it is detect at sampling time t_{k-m}. Let the transition counter output at time t_k be $count(t_k)$. A change in the counter value signifies that a transition event has

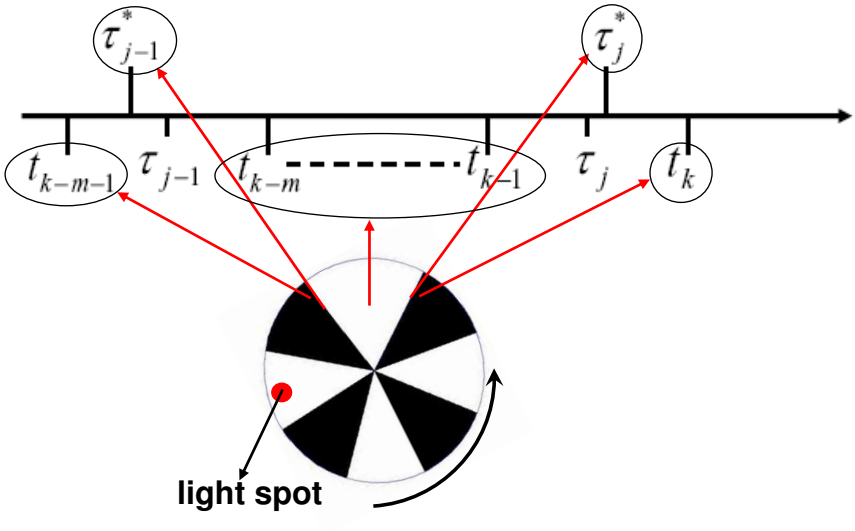

Figure 3.6: Event based Kalman filter time denotations. τ_j^* denotes the "occurrence time" of a "transition event", τ_j denotes the estimate of the "occurrence time" of a "transition event", and t_k denotes the sampling time.

occurred between the current sampling instant and the previous one. We define that a transition event is detected at t_k if:

$$\text{count}(t_k) - \text{count}(t_{k-1}) \geq 1 \tag{3.2}$$

The code wheel has a limited number of sectors (8 sectors), for the range of angular velocities $(20 - 40Hz)$ under consideration. Operated at the highest angular velocity, the time when the light spot stays on one sector is $2.9ms$. Therefore, a sampling rate of $1000Hz$ or above is sufficiently fast to guarantee only one transition edge can occur between two consecutive samples. Here we have assumed that counter overflow has been properly adjusted.

As explained in section 3.2, the measurement noise induced by the uncertainty on the transition event occurrence time is denoted by n_1, and the measurement noise induced by the bias on the threshold value is denoted by n_2. These two noises are assumed to be independent.

Taking the jth "transition event" as an example, when a measurement is detected, the only information available is that a transition event has happened in between the

two sampling times t_{k-1} and t_k. When the sampling rate is not high, this event's detection time uncertainty becomes significant. The occurrence time of the transition event $\tau_j^* \in (t_{k-1}, t_k]$ is assumed to be uniformly distributed on $(t_{k-1}, t_k]$. We define a new variable τ_j to denote the estimate of the "transition event" occurrence time τ_j^*. We estimate the transition event to happen at this estimated instant $\tau_j := (t_k + t_{k-1})/2$, and we assume that during this short period of time $t_k - t_{k-1}$, the spool angular velocity remains constant. In this way the uncertainty on transition event occurrence time is converted to a zero mean uniformly distributed measurement noise on the spool angular position at time τ_j. We denote this noise by n_1.

The other measurement noise is induced by the photodiode output discretization threshold bias, and is denoted as n_2. Since the laser light spot is large, when the spot crosses the sector boundary, the photodiode response is not an ideal square wave. A threshold is required to discretize the analog photodiode response. A bias on the threshold value can cause an error on the estimate of the transition event occurrence time, as shown in Fig. 3.7.

We assume that when the photodiode output switches from high to low (or low to high), between two successive sampling instants, the spool angular velocity is constant. The error on the estimate of the transition event occurrence time is converted to a measurement noise of the spool angular position at the estimate of the transition event occurrence time.

The measurement is available only when a transition event is detected, and the measurement information refers to the instant τ_j. The measurement is modeled as following:

$$y(t) = \begin{cases} \begin{pmatrix} 1 & 0 \end{pmatrix} \cdot \begin{pmatrix} \theta \\ \omega \end{pmatrix} + n_1 + n_2 & \text{if } t = \tau_j \\ \text{not available} & \text{if } t \neq \tau_j \end{cases} \tag{3.3}$$

If the noises n_1 and n_2 are treated directly from a detection time point of view, and the system is modeled in the angle domain, the system will be modeled as a time varying system. However, by assuming a constant angular velocity between sampling instants, the transition event detection time error is converted to a spool angular position error, and a linear continuous time time invariant system with event based measurement is obtained instead. The noises will have the following characteristics:

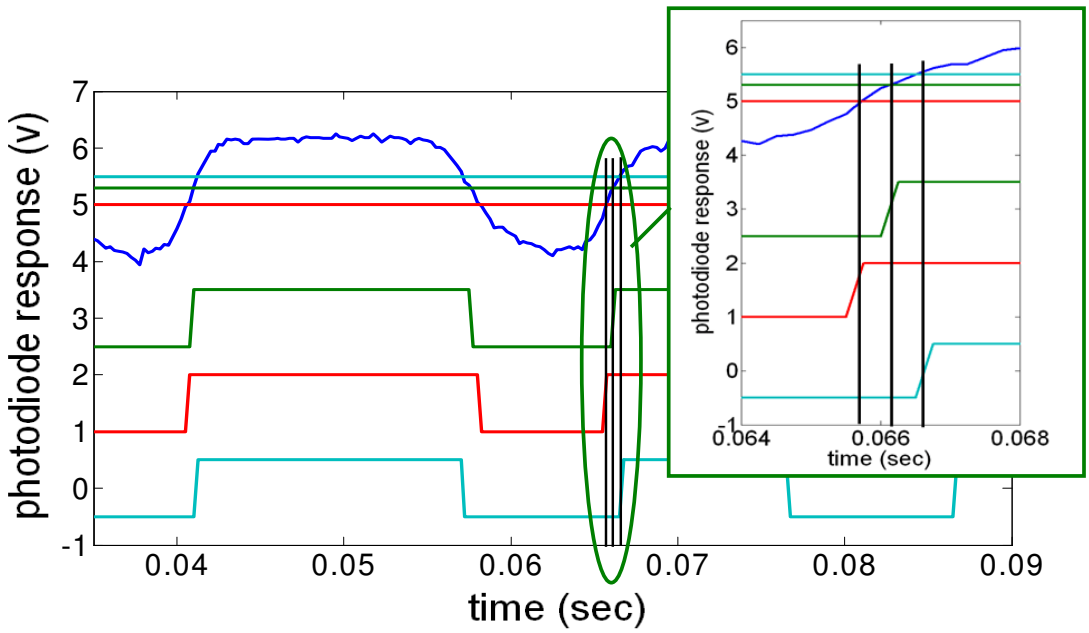

Figure 3.7: Measurement noise caused by the threshold error: the blue curve is the raw measurement; the green curve is the discretization of the raw signal with the correct threshold valve; the red curve and the sky blue curve are the discretization with biased threshold values.

- noise n_1 is assumed to be zero mean, uniformly distributed, and it is bounded by $|n_1| \leq 0.5\omega\Delta T$; the variance of this variable is $(0.5\omega\Delta T)^2/3$. This measurement noise is scaled with the sampling time ΔT.

- noise n_2 is assumed to be zero mean, normally distributed with its probability density function as a symmetric triangle function across the period. The noise's variance is $((0.5\omega\Delta T)/2)^2$. Since the sampling time is selected to guarantee that one transition event can happen within one sampling period ΔT, the longest time for the light receiver output signal to switch from high to low (or vice versa) is ΔT.

Here, we will summarize the system model:

$$\frac{d}{dt}\begin{pmatrix}\theta\\ \omega\end{pmatrix} = \underbrace{\begin{pmatrix}0 & 1\\ 0 & 0\end{pmatrix}}_{F}\begin{pmatrix}\theta\\ \omega\end{pmatrix} + \begin{pmatrix}0\\ 1\end{pmatrix}\cdot d(t)$$

$$y(t) = \begin{cases}\begin{pmatrix}1 & 0\end{pmatrix}\cdot\begin{pmatrix}\theta\\ \omega\end{pmatrix} + n_1 + n_2 & \text{if } t = \tau_j\\ \text{not available} & \text{if } t \neq \tau_j\end{cases}$$

$$\begin{aligned}E[n_1(t)n_1^{'}(t)] &= R_1(t)\delta(t-\tau), \quad E[n_1(t)] = 0\\ R_1(t) &= \frac{1}{3}(0.5\omega\Delta T)^2\\ E[n_2(t)n_2^{'}(t)] &= R_2(t)\delta(t-\tau), \quad E[n_2(t)] = 0,\\ R_2(t) &= \frac{1}{4}(0.5\omega\Delta)^2\\ E[d(t)d^{'}(t)] &= q\delta(t-\tau), \quad E[d(t)] = 0\end{aligned} \tag{3.4}$$

where θ is the spool angular position, ω is the spool angular velocity, y is the angular position measurement. R_1 and R_2 denote the covariance of the measurement noise, and q denotes the covariance of the process noise.

3.4 Event based Kalman filter observer

As described earlier, the spool angular position measurement is not always available, and when it is available, the measurement is corrupted by noise. If the position measurement

is continuously available but noisy, the problem would be trivial, and the continuous time Kalman filter technique can be applied to estimate the spool angular position and velocity from the corrupted position measurement. However, this "event" based spool position measurement poses the difficulty in developing the estimator. Our solution is to adopt the continuous time time varying Kalman filter theory [84] to accommodate the uncertain event based measurements. The resulting algorithm is that: between each transition detection, the Kalman filter operates in an open loop manner without measurement feedback, and the states are updated based on the dynamic model only. When a transition event is detected, both the Kalman filter gain and the state estimate are updated discretely. The Kalman filter operates in the open loop manner again until the next event is detected.

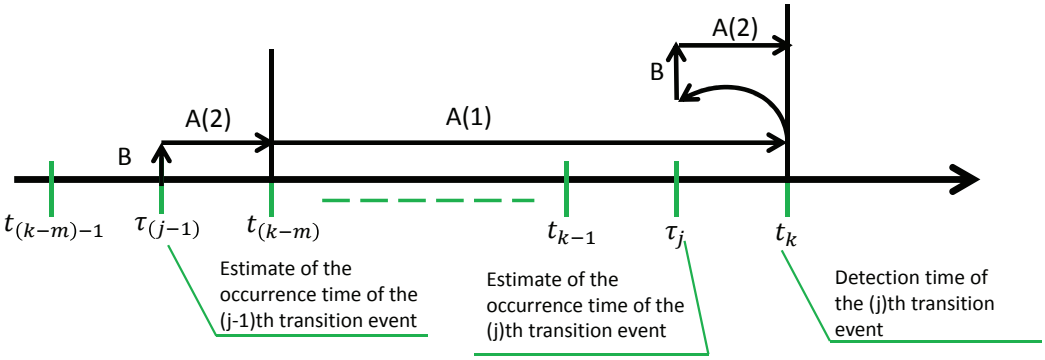

Figure 3.8: Event-based Kalman filter time line

The time flow of the proposed approach is shown in Fig. 3.8. $\tau_j, i = 1, 2, \cdots$ are the instants when transition events occur. In Fig. 3.8, the transition event that happens at τ_j is detected at t_k. The algorithm is explained along the time line. $A(1)$ denotes the section where the spool angular position and velocity are estimated in an open loop manner based on the plant model. The initial condition of the open loop estimation is defined based on the measurement of the transition event at τ_{j-1}. After the $j-th$ transition event is detected at t_k, the estimation of the spool angular position and velocity at t_k will be separated into two steps. The first step is to use the measurement information to update the spool states estimation at the time instant $\tau_j = \frac{1}{2}(t_{k-1} + t_k)$, which is denoted by B. In the second step, the estimator again operates in an open

loop manner from $t = \tau_j$ to $t = t_k$ to provide the spool state estimation at t_k, and the algorithm is explained in detail below.

In section $A(1)$, no measurement is detected. The estimates of the spool angular position and velocity are calculated based on the knowledge of the system model in an open loop manner. The estimates of the states are denoted by $\hat{X} := (\hat{\theta} \;\; \hat{\omega})^{\mathrm{T}}$. Recalling the matrix F defined in Eqn. (3.4) and the time line presented in Fig. 3.8, the estimator is modeled as:

$$\frac{d}{dt}\hat{X}(t|j-1) = F\hat{X}(t|j-1), \quad \text{for} \;\; t_{k-m} < t < t_{k-1} \tag{3.5}$$

where $X(t|j-1)$ denotes the estimate of state given that the $j-1$ th event has been detected but the j th even has not been detected.

Since no measurement is available in this period of time, a continuous-time Kalman filter is adapted to update the covariance of the estimation error only with the knowledge of the system model. Under this condition, $P(t|j-1)$, which denotes the covariance of the estimation error given that the $j-1$ th event has been detected is calculated following the Riccati equation[62]:

$$\begin{aligned} &\frac{d}{dt}P(t|j-1) = P(t|j-1)F^T + FP(t|j-1) + Q_w, \quad \text{for} \;\; t_{k-m} < t < t_{k-1} \\ &Q_w = \begin{bmatrix} 0 & 0 \\ 0 & q \end{bmatrix} \end{aligned} \tag{3.6}$$

Q_w represents the covariance of the process noise $d(t)$ from Eqn. (3.4). $P(t|j-1)$ has the form of $P(t|j-1) = \begin{pmatrix} P_{11}(t|j-1) & P_{12}(t|j-1) \\ P_{21}(t|j-1) & P_{22}(t|j-1) \end{pmatrix}$. When no measurement is implemented, an analytical solution can be developed to solve for $P(t|j-1)$, with the

initial condition:

$$P(t_{k-m}|j-1) = \begin{pmatrix} P_{110} & P_{120} \\ P_{210} & P_{220} \end{pmatrix} = \begin{pmatrix} p & 0 \\ 0 & p \end{pmatrix}$$

$$\begin{aligned}
&\text{for } t_{k-m} < t < t_{k-1} \\
P_{22}(t|j-1) =& q \cdot (t - t_{k-m}) + P_{220} \\
P_{12}(t|j-1) =& \frac{1}{2} \cdot q \cdot (t - t_{k-m})^2 + P_{220} \cdot (t - t_{k-m}) + P_{120} \\
P_{21}(t|j-1) =& \frac{1}{2} \cdot q \cdot (t - t_{k-m})^2 + P_{220} \cdot (t - t_{k-m}) + P_{210} \\
P_{11}(t|j-1) =& \frac{1}{3} \cdot q \cdot (t - t_{k-m})^3 + P_{220} \cdot (t - t_{k-m})^2 \\
& + P_{120} \cdot (t - t_{k-m}) + P_{210} \cdot (t - t_{k-m}) + P_{110}
\end{aligned} \tag{3.7}$$

The open loop estimation continues until a measurement is detected at $t = t_k$. The information we have is that an event happens between $[t_{k-1}, t_k]$, but the exact event occurrence time is unknown. Since the event can happen at any instant between $[t_{k-1}, t_k]$ with the same probability, the transition event is estimated to happen at $\tau_j = \frac{1}{2}(t_{k-1} + t_k)$ to create an estimate without bias. The measurement detected at $t = t_k$ is used to update the estimate of the states and the covariance of the estimation error at $t = \tau_j$. The a priori state estimate at τ_j, denoted by $\hat{X}(\tau_j|j-1)$, is calculated in section A(1). This is the estimate of the spool angular position and velocity before processing the measurement. The a posteriori state estimate denoted as $\hat{X}(\tau_j|j)$ is the estimation of the spool states after processing the measurement. This action is denoted by B on the time line in Fig. 3.8.

$$\begin{aligned}
\hat{X}(\tau_j|j) &= \hat{X}(\tau_j|j-1) + K(\tau_j)\left[y(\tau_j) - H^T \hat{X}(\tau_j|j-1)\right] \\
H &= \begin{pmatrix} 1 & 0 \end{pmatrix}^T \\
K(\tau_j) &= P(\tau_j|j-1)H
\end{aligned} \tag{3.8}$$

Similarly for the estimation error covariance matrix at this instant, we denote the a priori estimate by $P(\tau_j|j-1)$ and the a posteriori estimate by $P(\tau_j|j)$. They are computed as:

$$P(\tau_j|j) = [(P(\tau_j|j-1))^{-1} + H^T(\tau_j)R^{-1}H]^{-1} \tag{3.9}$$

After the discrete update, open loop estimation is used again in section A(2) to estimate the spool states and estimation error covariance at $t = t_k$. With this information, the a posteriori estimates of the states and the error covariance matrix can be calculated with the measurement detected at t_k:

$$\begin{aligned} \frac{d}{dt}\hat{X}(t|j) &= F\hat{X}(t|j) \\ \frac{d}{dt}P(t|j) &= P(t|j)F^T + FP(t|j) + Q_w(t) \end{aligned} \tag{3.10}$$

From t_k, the open loop estimation is activated until the next measurement is obtained, and the the above process is repeated.

3.5 Simulation Results

The system described in section 3.3 was simulated using Simulink with the parameters selected based on the experimental setup. The angular velocity of the spool was assumed to be $25Hz$, or $\omega = 157.1rad/s$. The encoder is assumed to have a resolution of $0.785rad$. The covariance of the estimation error at $t = 0$ is initialized by setting p to 1000. Assume the black-white transition time is smaller than $1.5ms$, set the covariance of the measurement noise as $R = 5.53 \times 10^{-3}rad^2$, and the covariance of the process noise modeled in Q_w in Eqn. (3.6) is set as as $q = 0.25rad^2/s^4$. Initial conditions for the states are selected to be $[\theta_0 \;\; \omega_0]^T = [0 \;\; 50]^T$.

The sampling time was selected to be $1ms$. As shown in Fig. 3.9 and Fig. 3.10, the estimation error of angular position takes less than $0.1sec$ to converge to less than $0.06rad$; and the estimation error of angular velocity takes the same amount of time to converge to less than $0.3rad/sec$. Compared with the measurement noise bound of $0.36rad$, the event based Kalman filter significantly improves the estimation precision. A zoom-in look at the spool angular velocity estimation on the period circled in Fig. 3.10 is shown in Fig. 3.11. The estimation of the angular velocity does not change between transition events, and it changes only when a transition event is detected. Initially, the estimation relies only on model dynamics and the initial condition of the current open loop period. This explains the large estimation error on the rotary position for the first $0.1sec$, because the estimate of the angular velocity is initialized at $50rad/sec$.

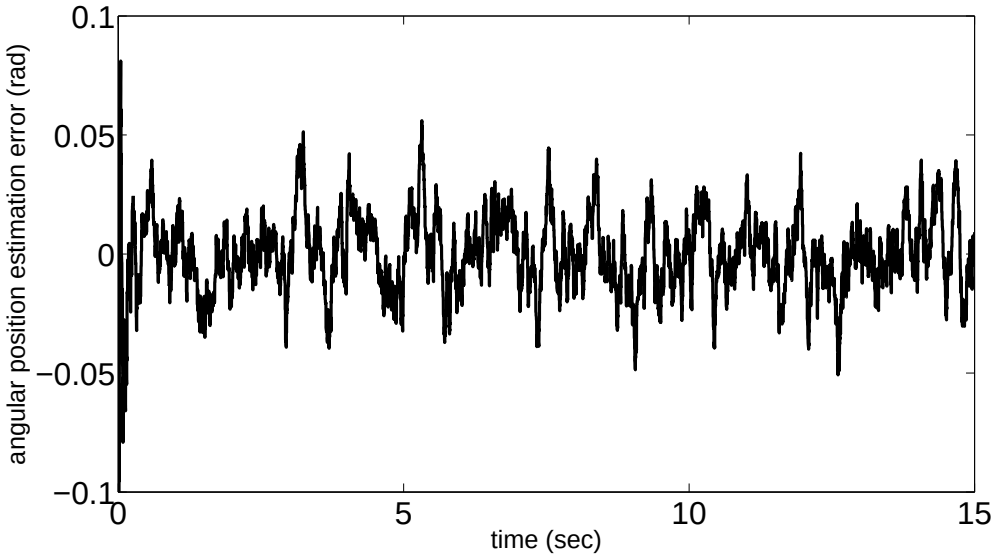

Figure 3.9: Angular position estimation error when $\Delta t = 1ms$

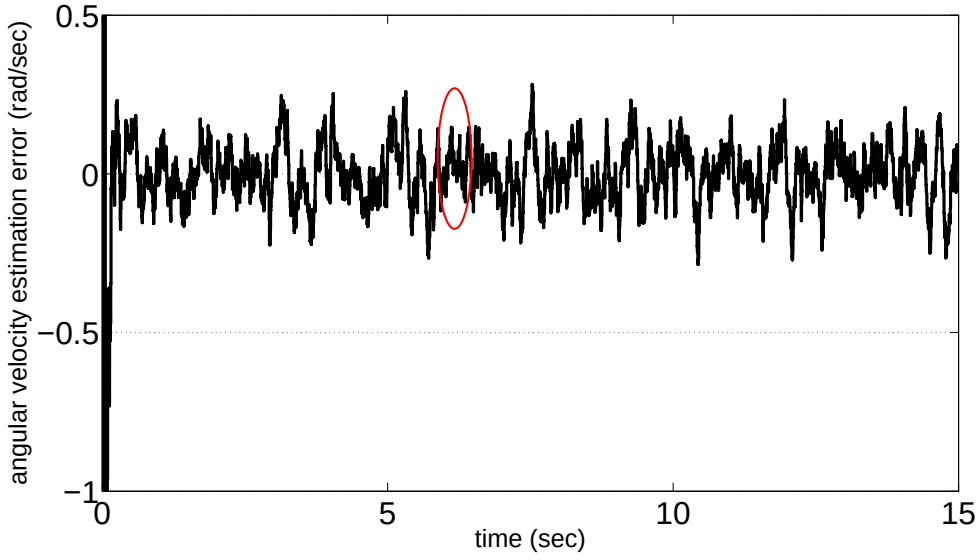

Figure 3.10: Angular velocity estimation error when $\Delta t = 1ms$

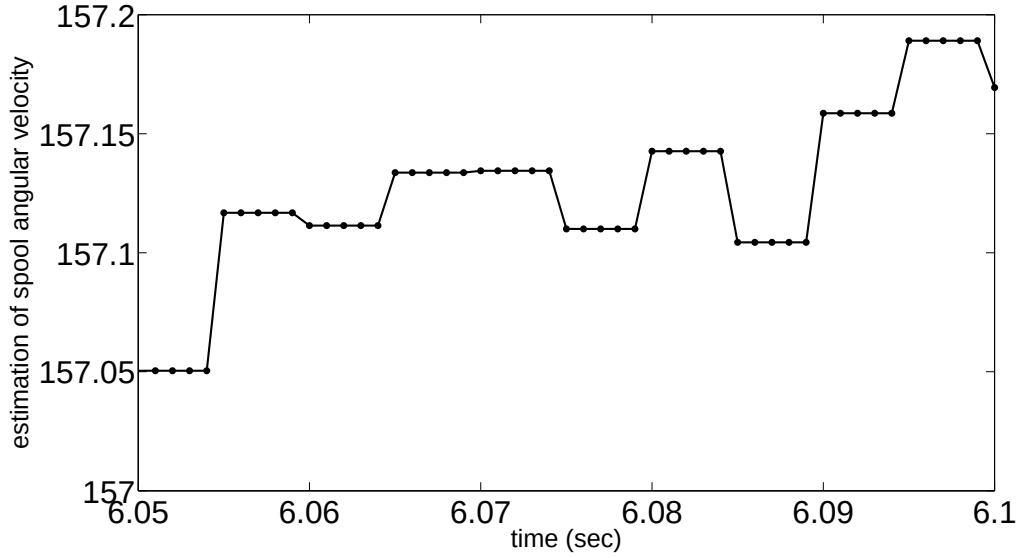

Figure 3.11: Angular velocity estimation when $\Delta t = 1ms$

3.6 Experimental Results

The event based Kalman filter was implemented experimentally to estimate the spool angular position and speed. The experimental apparatus is shown in Fig. 3.12. The rotary valve is connected to a fixed displacement vane pump via a customized pump housing. The vane pump has a displacement of $22.8cc$, and the pump is driven by a $5.6kW$ AC motor. The speed of the AC motor can be varied through a variable frequency drive (VFD), so that the pump output flow can be varied. The maximum flow the system can provide is $40lpm$. The valve's self-spinning spool is driven by the flow moment passing across it.

The sampling time was $1ms$. Initially the VFD frequency was set at $40Hz$, and a constant flow of $26.7lpm$ was passing across the valve. No additional sensors were available to directly measure the spool angular position. Therefore, the effectiveness of the proposed Kalman filter approach cannot be validated directly. However, the spool angular position is directly related to the valve inlet pressure, because the inlet flow (pressure) is pulse width modulated. Three PWM sections are wrapped around the valve spool, and the inlet pressure exhibits a repeated pattern with respect to the

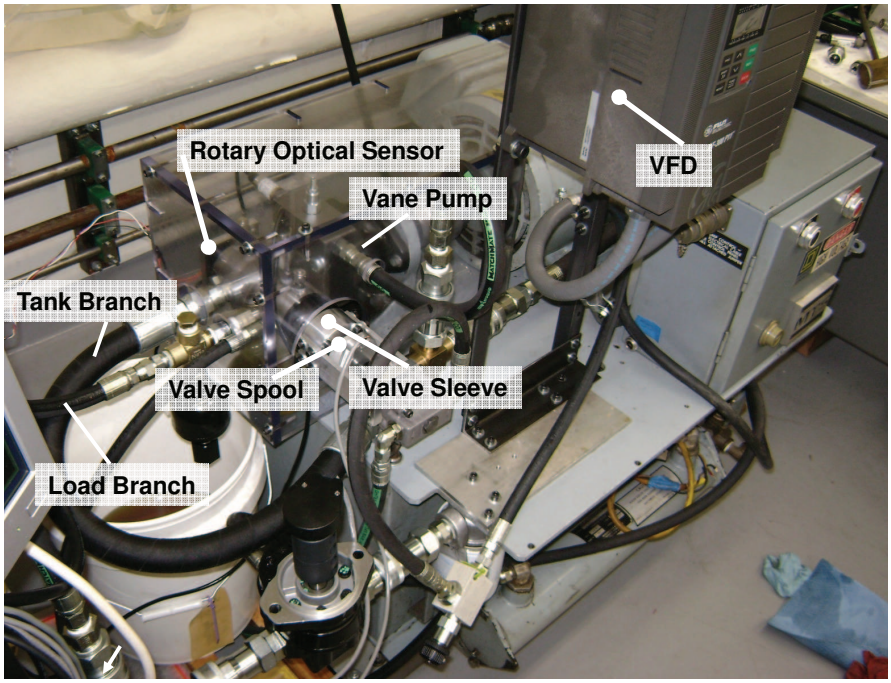

Figure 3.12: Experimental Apparatus of the VVDP

spool angular position for a fixed duty ratio (fixed axial position of the valve spool). If the Kalman filter estimates the spool angular position accurately, the pressure profile should be nearly periodically synchronous with the estimated spool angular position. In Fig. 3.13, the VVDP valve inlet pressure is plotted with respect to time, and the estimated spool angular position. During one revolution, the pressure shows three repetitive patterns. The strong correlation between the pressure profile and the estimated position shows the effectiveness of the event based Kalman filter.

Next, we study the dynamic response of the Kalman filter. A step change was applied to the spool angular velocity by applying a step change on the VFD frequency from $40Hz$ to $60Hz$. Varying the VFD frequency causes the pump output flow to change from $26.7lpm$ to $40lpm$, which correspondingly changes the turbine torque of the valve spool, and brings the spool angular velocity to a different equilibrium point. Figure 3.14 shows the Kalman filter's response to a spool angular velocity change. Since the driving torque is not modeled explicitly in the system model (Eqn. (3.1)), the Kalman filter responds to the position measurement only, and the transition time is less than $0.1sec$.

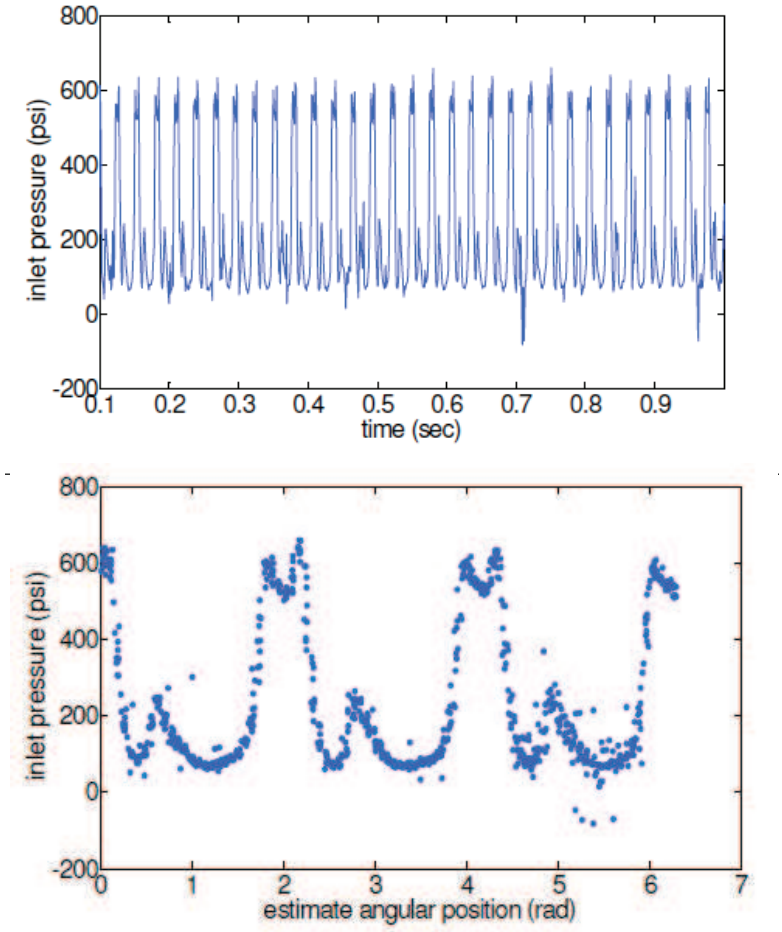

Figure 3.13: Event based Kalman filter experimental results for a case where the valve spool rotates 11 cycles. Top: VVDP inlet pressure with respect to time, bottom: inlet pressure with respect to spool angular position

The response time of the Kalman filter can potentially be improved by incorporating the driving torque of the turbine and the friction torque of the spool into the design of the Kalman filter.

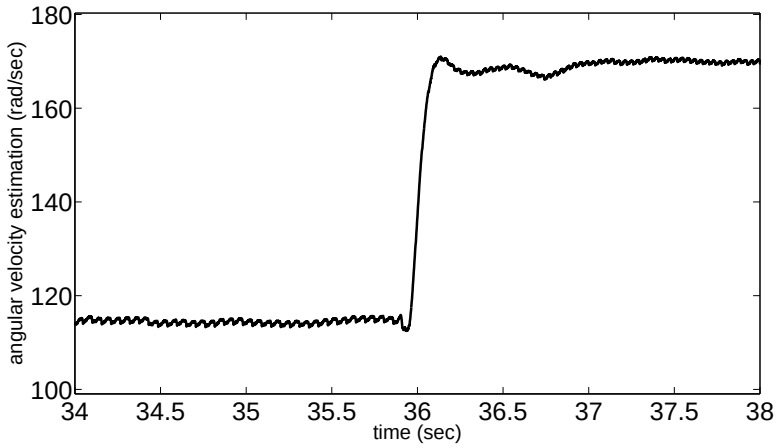

Figure 3.14: Transition response to a step change in angular velocity

3.7 Summary

The sensor constraint of our valve set up motivated the development of an event based Kalman filter, which can accurately estimate the valve rotary position and velocity using a coarse measurement received at an irregular time interval. With several simplifying assumptions, the original time-varying system is transformed into an LTI system. In the event based Kalman filter, continuous time varying Kalman filter theory [84] is adopted to accommodate the uncertain event based measurements. The resulting algorithm is: between events, since no measurement is available, the Kalman filter operates in an open loop manner, and the states are updated based on the dynamic model only; when a transition occurs, this measurement is used to update the dynamic model based state estimation following a standard Kalman filter. Both the simulation results and the experimental results validate the effectiveness of the event based Kalman filter.

This event based Kalman filter is applicable to situations where precise estimation of the system states is required, but the measurement is coarse and irregularly available.

Chapter 4

Spool axial position controller in the presence of periodic measurement noise

4.1 Introduction

This chapter will focus on the sensing, actuation and controller design for the valve spool axial position, which correspondingly controls the PWM valve's duty ratio.

As shown in Fig. 4.1, the spool axial motion is actuated hydro-statically using an electro-hydraulic gerotor pump. The pump is hydraulically connected to both ends of the valve sleeve. By pumping fluid from one end of the sleeve to the other end, the spool axial position is varied. The differential pressure required to actuate the spool is less than $2.76bar$ $(40psi)$, and the actuation power is small $(< 200watt)$.

The self-spinning feature of the valve spool prefers a non-contact sensor to measure the spool axial position, so that the sealing structure is simplified. The spool axial position is measured using an optical sensor, which consists of two LEDs and a photodiode. Light emitted from the LEDs reflects off of the polished spool end and is received by the photodiode. The LED light intensity varies monotonically with the light's traveling distance, and the relationship can be calibrated. A static mapping is obtained between the photodiode response to the light intensity and the spool axial position.

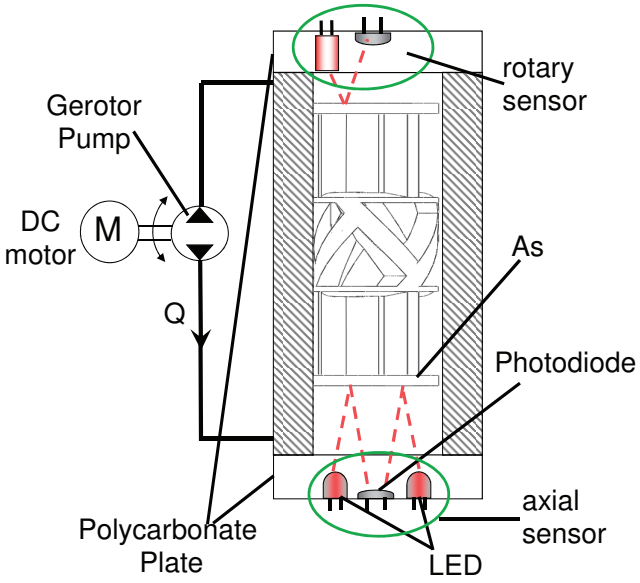

Figure 4.1: Valve spool axial actuation and sensing

Since the spool end cannot be polished to be perfectly uniform, and the rotary motion disturbs the oil inside the axial chamber, which serves as the transparent medium for the LED light to travel through, the spool rotary motion introduces a periodic measurement noise on the spool's axial position measurement, as shown in Fig. 4.2. The pattern of the noise is collected experimentally. In this experiment, the spool spins while being pushed against a hard stop to fix its axial position. The DC component of the optical sensor's output is removed, and the residual part of the sensor's output represents the measurement noise. Distinguishing between the exact spool position and this additive periodic measurement noise is important. Otherwise, via close loop control, the actuator will respond to the corrupted measurement, and the spool will oscillate axially. Given such a structured noise at a certain frequency (spool rotary frequency), a low pass filter is not sufficient to eliminate the effect of noise.

The question we will address in this chapter is how to distinguish the spool position from the structured noise, and to achieve a precise spool axial position control. The key part of the solution is to develop a dynamic model of the structured noise, so that both the spool position state and the structured noise states can be estimated from the corrupted measurement and their dynamics model via a proper estimator. The

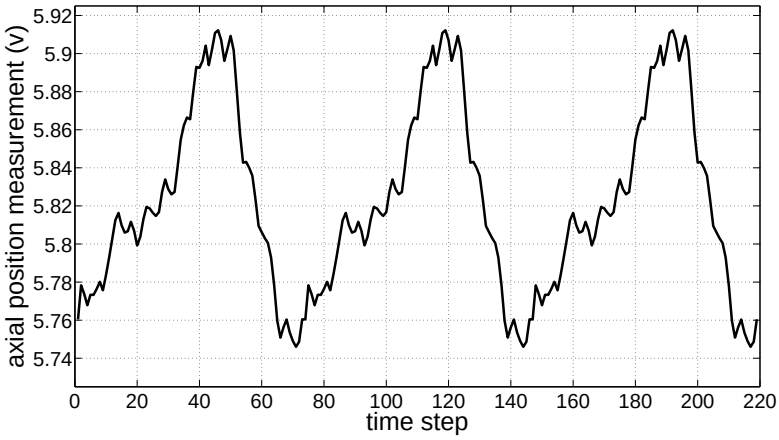

Figure 4.2: Optical sensor's output when the spool spins at a fixed axial position

structured measurement noise is caused by the spool rotary motion. As discussed in the chapter 3, if a constant flow is fed through the valve, the valve spool will rotate at a constant angular velocity. In our case, a constant flow of $40lpm$ is provided to the rotary valve, and the spool operates at a constant angular velocity of $13Hz$. Although the measurement noise is periodic with respect to the spool angular position instead of time, since the spool spins at a constant angular velocity, this noise becomes periodic in time. Two approaches will be introduced in this chapter to model this periodic measurement noise. One is a discrete time linear time invariant signal generator, and the other is a periodic continuous time varying model using weighted basis functions.

The rest of this chapter is organized as follows. In section 4.2 the spool dynamics of its axial motion and two dynamic models describing the periodic structured noise will be presented. The spool axial dynamics will be augmented with the noise model, and the observability of the corresponding augmented system will be analyzed. A Kalman filter will be designed to estimate the states of the spool axial position and the periodic measurement noise. Afterwards, a feed-forward with PI controller will be developed for the spool position reference tracking. The procedure for designing a Kalman filter and a PI with feed-forward controller will be presented in section 4.3 and section 4.4 respectively. Experimental validation and simulation discussions will be presented in section 4.5. Finally, some concluding remarks will be presented in section 4.6.

4.2 System modeling

A model representing the dynamics of the axial position of the spool is defined in section 4.2.1. Dynamic models for the periodic measurement noise and the augmented system are derived in section 4.2.2.

4.2.1 Spool dynamics modeling

The valve spool's axial position sensing and actuation system is shown in Fig. 4.1. The actuator is a fixed displacement gerotor pump powered by a DC motor. The direction of the motor speed is controlled using an electrical H-bridge. The speed of the motor is controlled by pulse-width modulating the enabling signal of the H-bridge. Varying the duty ratio of the PWM enabling signal, the motor speed is varied, and therefore, the pump flow rate is controlled. The pump dynamics exhibit dead-band, saturation, and asymmetry, which are modeled as spool dynamics' process noise.

The fluid inside the valve axial chambers is treated as incompressible media, and the pressure dynamics are ignored. The spool axial dynamics are modeled as:

$$\dot{x} = \frac{Q(u)}{A_s} + w(t) \tag{4.1}$$

where $x(t)$ is the spool axial position, $Q(u)$ is the flow fed into the axial chamber, A_s is the spool end area, and $w(t)$ represents the un-modeled spool dynamics. The static relationship between the input u and the flow $Q(u)$ is calibrated experimentally. The same experimental data is utilized to map from u to Q and from Q to u, and the results are shown in Fig. 4.3. The inaccuracy of the flow map is incorporated in the spool dynamics uncertainty $w(t)$.

The measurement of the spool axial position $y(t)$ is corrupted by a T-periodic noise $d(t) = d(t+T)$ and an unstructured noise $n(t)$. At a fixed axial position, when the spool is spinning, the average response from the axial sensor is treated as the calibration of the axial position measurement at the given location. In this way, the noise $d(t)$ becomes a repetitive signal with zero mean. $n(t)$ is assumed to be a white noise with zero mean. With these assumptions, the spool's axial position dynamics and the periodic noise are modeled as:

$$y(t) = x(t) + d(t) + n(t) \tag{4.2}$$

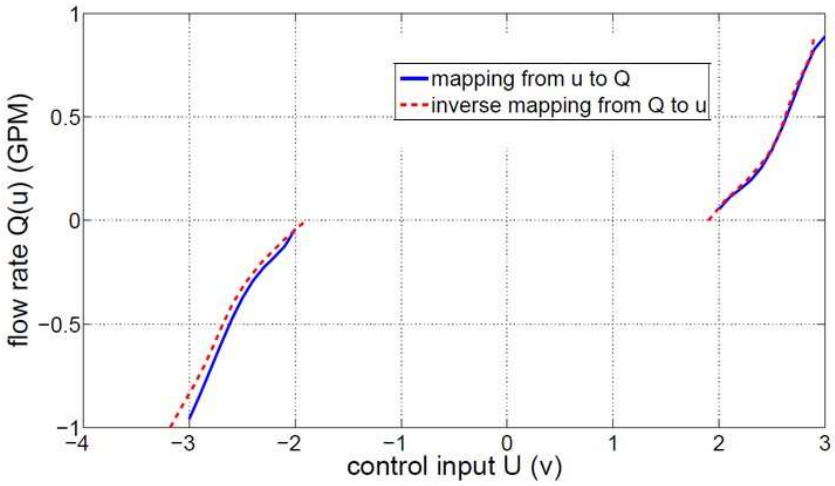

Figure 4.3: Mapping between the control input and the gerotor pump flow rate

$$\int_{t}^{t+T} d(\tau) \cdot d\tau = 0$$

4.2.2 Periodic measurement noise dynamics and the augmented system dynamics

A dynamic model is defined for the periodic measurement noise $d(t)$, and this model will further be augmented with the spool position dynamics. In this section, we will introduce two methods to model the dynamics of $d(t)$: a linear discrete time time-invariant model, and a period time varying model. The corresponding augmented system dynamics will be defined respectively.

Discrete Time Time-invariant Model

Firstly, we propose a discrete linear time invariant (LTI) system to model the dynamics of $d(t)$. $d(k) = d(k+N)$ is the discretized version of $d(t)$ with a sampling time of T_s and a period of T. The discrete time period is $N \approx T/T_s$, where N is an integer. The mean value of the noise $d(t)$ over one period is zero. We can formulate a disturbance

generating exo-system to represent this periodic signal:

$$\begin{aligned} x_d(k+1) &= A_d x_d(k) \\ d(k) &= C_d x_d(k) \end{aligned} \tag{4.3}$$

with

$$A_d = \begin{pmatrix} 0 & 1 & 0 & \cdots & 0 \\ 0 & 0 & 1 & \cdots & 0 \\ \vdots & \vdots & \vdots & \ddots & \vdots \\ 0 & 0 & \cdots & 0 & 1 \\ -1 & -1 & \cdots & -1 & -1 \end{pmatrix} \in \mathbb{R}^{(N-1)\times(N-1)}$$

$$C_d = \begin{pmatrix} 1 & 0 & \cdots & 0 \end{pmatrix} \in \mathbb{R}^{1\times(N-1)}$$

Correspondingly, we develop a discrete time linear time invariant model for the spool's axial motion dynamics. Equation. (4.1) is discretized as:

$$x(k+1) = x(k) + T_s \frac{Q(u(k))}{A_s} + w(k) \tag{4.4}$$

Together with the dynamics of the periodic measurement noise $d(t)$ defined in Eqn. (4.3), an augmented system is defined as:

$$\begin{aligned} \underbrace{\begin{pmatrix} x(k+1) \\ x_d(k+1) \end{pmatrix}}_{x_{aug1}} &= \underbrace{\begin{pmatrix} 1 & 0 \\ 0 & A_d \end{pmatrix}}_{A_{aug1}} \begin{pmatrix} x(k) \\ x_d(k) \end{pmatrix} + \underbrace{\begin{pmatrix} \frac{T_s}{A_s} \\ 0 \end{pmatrix}}_{B_{aug1}} Q(u(k)) + w(k) \\ y(k) &= \underbrace{\begin{pmatrix} 1 & C_d \end{pmatrix}}_{C_{aug1}} \begin{pmatrix} x(k) \\ x_d(k) \end{pmatrix} + n(k) \end{aligned} \tag{4.5}$$

where $x_{aug1} \in \mathbb{R}^{\mathrm{N}\times 1}$, $A_{aug1} \in \mathbb{R}^{\mathrm{N}\times\mathrm{N}}$, $C_{aug1} \in \mathbb{R}^{1\times\mathrm{N}}$, $w(k) \in \mathbb{R}^{\mathrm{N}\times 1}$. $n(k)$ represents the un-structured measurement noise as modeled in Eqn. (4.2).

In this approach, the dimension of x_d heavily relies on the selection of the sampling time. For example, for a periodic signal of $10Hz$, if $T_s = 2ms$, 50 states are required to represent the noise dynamics, and if $T_s = 1ms$, then $N = 100$. The dimension of the estimator increases as the sampling time decreases. A high dimension estimator increases the computational cost, and weakens the estimator robustness.

The observability of this augmented system modeled in Eqn. (4.5) is determined by the rank of the observability matrix. The augmented system described by Eqn. (4.5) is observable if the corresponding observability matrix is of full rank[85]. The observability matrix of system Eqn. (4.5) is defined as $\mathcal{O} \in \mathbb{R}^{N\times N}$:

$$\mathcal{O} = \begin{pmatrix} C_{aug1} \\ C_{aug1}A_{aug1} \\ \cdots \\ C_{aug1}A_{aug1}^{N} \end{pmatrix} = \begin{pmatrix} 1 & 1 & 0 & \cdots & 0 & \\ 1 & 0 & 1 & 0 & \cdots & \\ \cdots & \cdots & \cdots & \ddots & \cdots & \\ 1 & 0 & 0 & \cdots & 1 & \\ 1 & -1 & -1 & -1 & \cdots & -1 \end{pmatrix}$$

And the determinant of $\mathcal{O}$ is calculated as:

$$\det(\mathcal{O}) = (-1)^{N+1}N \neq 0 \tag{4.6}$$

Since the determinant of the observability matrix is non-zero, the observability matrix $\mathcal{O}$ is of full rank, and the pair (A_{aug1}, C_{aug1}) is observable. Both the spool axial position state and the periodic measurement noise states can be observed via a proper estimator.

Continuous time periodic time-varying model

Although the discrete time LTI noise model can produce an augmented system that is observable, the high order will drastically degrade the robustness of the estimator, which makes it infeasible to be implemented experimentally. To take advantage of the "periodic" property, we propose a periodic time-varying model to represent the noise.

In this approach, the periodic signal is represented by a linear combination of a set of periodic basis functions $f_i(t) = f_i(t+T)$:

$$d(t) = \sum_i x_{di} f_i(t) = \underbrace{\begin{pmatrix} f_1(t) & f_2(t) & \cdots & f_n(t) \end{pmatrix}}_{C_{d2}(t)} \underbrace{\begin{pmatrix} x_{d1} \\ \vdots \\ x_{dn} \end{pmatrix}}_{X_{d2}} \tag{4.7}$$

where x_{di} is the weight. This approach has the flexibility of selecting different types of basis functions, tailored to the structure of the periodical noise.

Figure 4.4 shows the curve fitting to the periodic noise with two different basis functions. One approach is to use a Fourier basis function, and the basis functions are defined as:

$$f_1(t) = \cos \omega t,\ \ f_2(t) = \sin \omega t,\ \ \cdots,\ \ f_{2i-1} = \cos i\omega t,\ \ f_{2i} = \sin i\omega t \tag{4.8}$$

where ω is the fundamental frequency. In our case, ω is the frequency of the periodic noise. The other approach is to use a set of Gaussian basis functions, and the basis function is defined as:

$$f_i(t) = e^{-\left(\frac{x-b_i}{c_i}\right)^2},\ \text{with}\ x = mod(t, \frac{2\pi}{\omega}) \tag{4.9}$$

where b_i is the centroid (location) and c_i is related to the peak width.

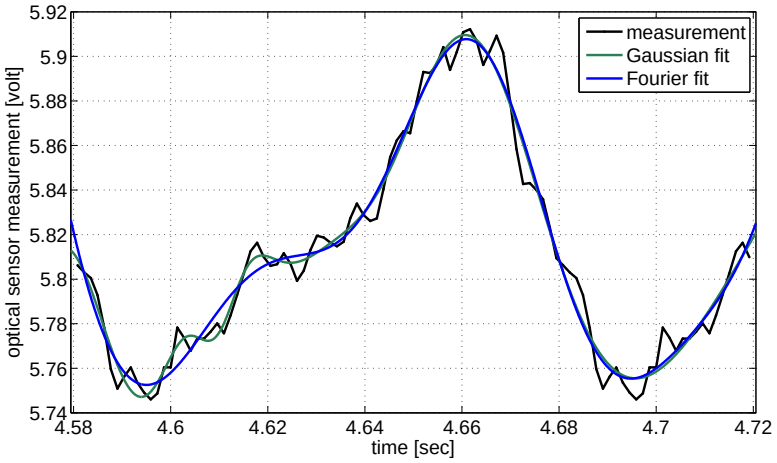

Figure 4.4: A periodic signal represented using different basis functions

In Fourier model, we use 6 basis functions, with their frequencies calculated at the fundamental frequency and up to its three times' the fundamental frequency. The fundamental frequency is the same as the spool rotary frequency. In the Gaussian model, we also use 6 basis functions. The basis functions are shown in Fig. 4.5. The Gaussian model produces a slightly better fitting result, but the calculation load is heavier than using the Fourier model. Therefore, for the rest of the analysis in this chapter, we will adopt the Fourier basis functions.

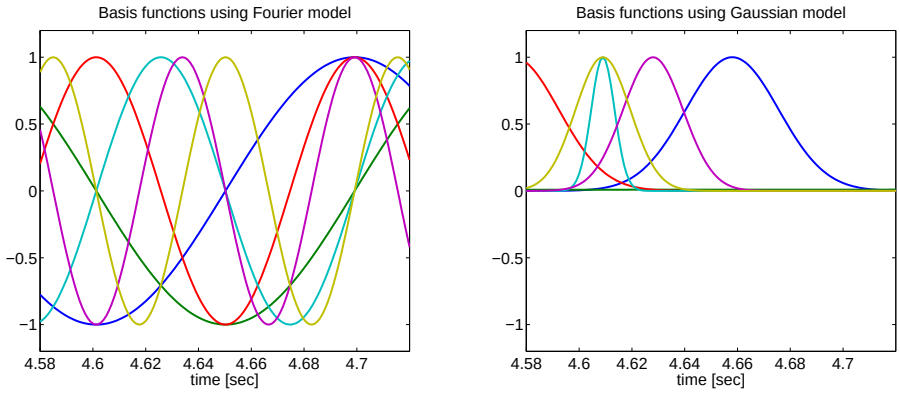

Figure 4.5: Fourier and Gaussian basis functions

Next, we will investigate the sensitivity of the model prediction error to the number of the basis functions. For a given model, the more basis functions we use, the more accurately we can approximate the periodic noise signal, with a penalty on increasing the computational cost. The photodiode measurement shown in Fig. 4.4 was collected by using an externally controlled spool. The spool was held at a fixed axial position while rotating at a constant angular velocity. We detrended the DC component from the photodiode output to obtain the zero-mean measurement noise. Utilizing the Fourier model, with the same fundamental frequency, we selected 10, 20, and 40 basis functions respectively to evaluate the estimation of the periodic measurement noise. The model with 40 basis functions produces the least estimation error, while 10 and 20 basis functions models do not exhibit a significant difference. Considering the balance between estimation accuracy and computational load, the model with 10 basis functions can effectively capture the dynamics of the photodiode measurement noise, and the Fourier model with 10 basis functions will be adopted to the analysis for the rest in this chapter.

With the Fourier functions structured noise model, we will investigate the observability of the augmented system. The periodic measurement noise model is augmented with the spool dynamics represented by Eqn. (4.1), and the dynamics of the augmented

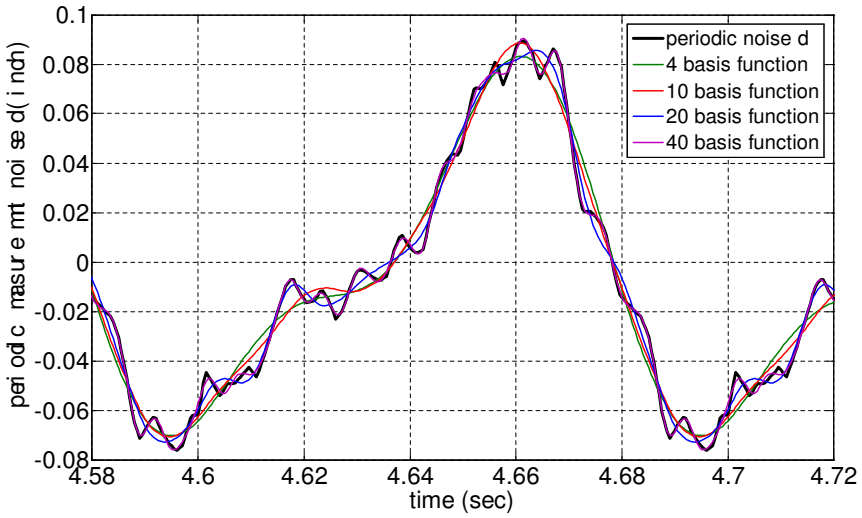

Figure 4.6: Sensitivity to the number of basis functions. The basis functions are Fourier basis.

system are defined as:

$$\frac{d}{dt}\underbrace{\begin{bmatrix} x \\ x_{d1} \\ x_{d2} \\ \vdots \\ x_{dn} \end{bmatrix}}_{x_{aug2}\in\mathbb{R}^{(N_d+1)\times 1}} = \underbrace{\begin{bmatrix} 0 & 0 & 0 & 0 & 0 \\ 0 & 0 & 0 & 0 & 0 \\ 0 & 0 & 0 & 0 & 0 \\ 0 & 0 & 0 & 0 & 0 \\ 0 & 0 & 0 & 0 & 0 \end{bmatrix}}_{A_{aug2}\in\mathbb{R}^{(N_d+1)\times(N_d+1)}} \begin{bmatrix} x \\ x_{d1} \\ x_{d2} \\ \vdots \\ x_{dn} \end{bmatrix} + \underbrace{\begin{bmatrix} 1 \\ 0 \\ 0 \\ 0 \\ 0 \end{bmatrix}}_{B_{aug2}\in\mathbb{R}^{N_d\times 1}} \frac{Q}{A_s} + \underbrace{\begin{bmatrix} w \\ w_{d1} \\ w_{d2} \\ \vdots \\ w_{dn} \end{bmatrix}}_{w}$$

$$y = \underbrace{\begin{bmatrix} 1 & \cos\omega t & \sin\omega t & \cdots & \cos\frac{n}{2}\omega t & \sin\frac{n}{2}\omega t \end{bmatrix}}_{C_{aug2}(t)\in\mathbb{R}^{1\times N_d}} \begin{bmatrix} x \\ x_{d1} \\ x_{d2} \\ \vdots \\ x_{dn} \end{bmatrix} + n \tag{4.10}$$

Since the augmented system is periodic in time, the observability of the augmented system is determined by checking the rank of the observability grammian matrix $\mathcal{M}(T,0)$ over one period T. If $\mathcal{M}(T,0)$ is invertible, the observability grammian matrix is of

full rank, and the augmented system is observable [85]. Since $A_{aug2} = 0_{(n_d+1)\times(n_d+1)}$, its transition matrix $\Phi^{\mathrm{T}}(t,0)$ and the observability grammian matrix $\mathcal{M}(T,0)$ of the augmented system described by Eqn. (4.10) are calculated as:

$$
\begin{aligned}
&\Phi^{\mathrm{T}}(t,0) = \mathrm{I}_{n_d+1\times n_d+1} \\
&\mathcal{M}(T,0) = \int_0^T \Phi^{\mathrm{T}}(t,0) C_{aug2}^{\mathrm{T}}(t) C_{aug2}(t) \Phi(t,0) dt \\
&= \int_0^T C_{aug2}(t)^{\mathrm{T}} C_{aug2}(t) dt \\
&= \begin{bmatrix}
1 & \mathcal{M}_{1,2} & \mathcal{M}_{1,3} & \cdots & \mathcal{M}_{1,\frac{n_d}{2}-1} & \mathcal{M}_{1,\frac{n_d}{2}} \\
\mathcal{M}_{2,1} & \mathcal{M}_{2,2} & \mathcal{M}_{2,3} & \cdots & \mathcal{M}_{2,\frac{n_d}{2}-1} & \mathcal{M}_{2,\frac{n_d}{2}} \\
\vdots & \vdots & \vdots & \ddots & \vdots & \vdots \\
\mathcal{M}_{\frac{n_d}{2}-1,1} & \mathcal{M}_{\frac{n_d}{2}-1,2} & \mathcal{M}_{\frac{n_d}{2}-1,3} & \cdots & \mathcal{M}_{\frac{n}{2}-1,\frac{n_d}{2}-1} & \mathcal{M}_{\frac{n_d}{2}-1,\frac{n_d}{2}} \\
\mathcal{M}_{\frac{n_d}{2},1} & \mathcal{M}_{\frac{n_d}{2},2} & \mathcal{M}_{\frac{n_d}{2},3} & \cdots & \mathcal{M}_{\frac{n_d}{2},\frac{n_d}{2}-1} & \mathcal{M}_{\frac{n_d}{2},\frac{n_d}{2}}
\end{bmatrix} \\
&\text{with } \mathcal{M}_{i,j} = \int_0^T C_{aug2}(i) * C_{aug2}(j) dt
\end{aligned}
\tag{4.11}
$$

Note that for integers i, j, with $i \neq j$, the determinant of the observability grammian matrix $\mathcal{M}(0,T)$ is calculated as:

$$
\begin{aligned}
&\int_0^T \cos i\omega t \sin j\omega t = 0, \quad \int_0^T \cos^2 i\omega t = \frac{T}{2}, \quad \int_0^T \sin^2 i\omega t = \frac{T}{2} \\
&\mathcal{M}(0,T) = \begin{bmatrix}
1 & 0 & 0 & \cdots & 0 \\
0 & \frac{T}{2} & 0 & \cdots & 0 \\
0 & 0 & \ddots & 0 & \vdots \\
\vdots & \vdots & 0 & \ddots & 0 \\
0 & 0 & \cdots & 0 & \frac{T}{2}
\end{bmatrix} \\
&\det(M(0,T)) = \left(\frac{T}{2}\right)^n \neq 0
\end{aligned}
\tag{4.12}
$$

Since the determinant of the observability grammian matrix is non-zero, the observability grammian matrix $\mathcal{M}(T,0)$ is non-singular, and the augmented system described in Eqn. 4.10 is observable. All the states can be uniquely estimated via a proper estimator.

4.3 State estimator for the augmented system

After modeling the dynamics of the periodic measurement noise $d(t)$, and the dynamics of the corresponding augmented system (Eqn. (4.5) and Eqn. (4.10)), we will develop estimators for the augmented system. Previous analysis showed that using both the discrete LTI model (Eqn. 4.5) and the periodic time varying model (Eqn. 4.10) to capture the photodiode measurement noise, the augmented system is observable. In this section we will develop a Kalman filter respectively to estimate the states of the augmented system. We assume that both the process noise w from the un-modeled dynamics and the un-modeled measurement noise n are white noise with zero mean.

4.3.1 State Estimator for the Discrete Time Augmented System

Utilizing the discrete time LTI model presented in Eqn. (4.5), the augmented system is also established as a discrete time LTI model. Following the typical procedure of designing a discrete time LTI Kalman filter, we have:

$$\begin{aligned}\hat{x}^{-}_{aug1}(k) &= A_{aug1}\hat{x}_{aug1}(k-1) + B_{aug1}Q(u)(k-1)\\ \hat{x}^{+}_{aug1}(k) &= \hat{x}^{-}_{aug1}(k) + L(k)\left[y(k) - C_{aug1}(k)\hat{x}^{-}_{aug1}(k)\right]\end{aligned} \tag{4.13}$$

where $\hat{x}^{-}_{aug1}(k)$ is the a priori estimate of the augmented system states, and $\hat{x}^{+}_{aug1}(k)$ is the a posteriori estimate of the augmented system states. The estimator gain $L(k)$ is computed by solving a discrete time Riccati equation [84]:

$$\begin{aligned}&P(k)^{-} = A_{aug1}P(k-1)^{+}A^{\mathrm{T}}_{aug1} + Q_1\\ &L(k) = P(k)^{-}C^{\mathrm{T}}_{aug1}(k)\left[C_{aug1}(k)P(k)^{-}C_{aug1}(k)^{\mathrm{T}} + R_1\right]^{-1}\\ &P(k)^{+} = \left[\mathrm{I} - L(k)C_{aug1}(k)\right]P(k)^{-}\left[\mathrm{I} - L(k)C_{aug1}(k)\right]^{\mathrm{T}} + L(k)R_1L(k)^{\mathrm{T}}\\ &P(k=0)^{+} = P_{01}\\ &Q_1 = diag\left[q_1 \quad \cdots \quad q_i \quad \cdots \quad q_{n+1}\right], \mathrm{E}(w_k w_j^{\mathrm{T}}) = Q_1\delta_{k-j}\\ &\mathrm{E}(n_k n_j^{\mathrm{T}}) = R_1\delta_{k-j}\end{aligned}$$

with $P(k)^{-}$ denoting the covariance of the estimation error of $\hat{x}(k)^{-}$, and $P(k)^{+}$ denoting the covariance of the estimation error of $\hat{x}(k)^{+}$. Q_1 and R_1 quantify the variances of the process noise and measurement noise respectively.

Since the dimension of the estimator increases linearly as the sampling time decreases, the resulting Kalman filter can have a high computational cost and the robustness of the estimator can degrade. This causes difficulty in experimental implementation.

4.3.2 State Estimator for the Continuous Time Time-varying Augmented System

Utilizing the continuous time periodic time-varying model presented in Eqn. (4.10), the augmented system also becomes a continuous time periodic time varying system. Therefore, we follow the typical procedure to derive a continuous time time varying Kalman filter:

$$\frac{d}{dt}\hat{x}_{aug2} = B_{aug2}Q(u) + L(t)(y - C_{aug2}(t)\hat{x}_{aug2}) \tag{4.14}$$

where $\hat{x}_{aug2}$ is the estimate of the augmented system states. The injection gain $L(t)$ is computed based on a continuous time periodic Riccati equation:

$$\begin{aligned} &L(t) = P_2(t)C_{aug2}^{\mathrm{T}}(t)R_2^{-1} \\ &\dot{P}_2(t) = -P_2(t)C_{aug2}^{\mathrm{T}}(t)R_2^{-1}C_{aug2}(t)P_2(t) + Q_2 \\ &Q_2 = E(ww^{\mathrm{T}}), \quad R_2 = E(nn^{\mathrm{T}}), \quad P_2(t=0) = P_0 \end{aligned} \tag{4.15}$$

with $P_2(t)$ representing the estimation error covariance for the augmented system states, and it is a periodic signal with a period of T: $P_2(t+T) = P_2(t)$. $T = \frac{1}{2\pi w_n}$, and w_n is the fundamental frequency of the Fourier transform of the periodic signal $d(t)$. Here, both the measurement noise n and the process noise w are assumed to be zero mean white noise.

Compared with the discrete time LTI model, this model has an advantage in reducing the system dimension. By selecting the proper type of basis function (i.e. Fourier model in our case), the dimension of x_d and the accuracy of the model in capturing the measurement noise profile can be balanced. The dimension of the noise model is not a function of the sampling time. Therefore, a small sampling time can be selected without drastically increasing the computational load, which is more robust to be implemented experimentally.

4.4 Controller design

The spool dynamics are modeled as a linear system in sec 4.2, and through the observability analysis in sec 4.3, we learned that both the discrete time time-invariant model presented in Eqn. (4.5) and the continuous time time-varying model presented in Eqn. (4.10) are observable. In this section, we will design a feedforward with PI (proportional integral) controller to regulate the spool position. The control objective is to regulate the spool axial position to track a reference position trajectory, and the duty ratio of the rotary valve can be manipulated.

The desired trajectory for spool axial position $r(t)$ is a periodic signal with period of $5sec$:

$$r(t) = \begin{cases} 0.8 & \text{if } mod(t,5) < 1 \\ 0.8 + 0.8(mod(t,1) - 1) & \text{if } 1 \leq mod(t,5) \leq 2 \\ 1.6 & \text{if } 2 < mod(t,5) < 4 \\ 1.6 - 0.8(mod(t,1) - 4) & \text{if } 4 \leq mod(t,5) \leq 5 \end{cases} \tag{4.16}$$

In this trajectory, the spool can travel its full stroke of $0.8inch$ within $1sec$. We define the valve spool position tracking error as $e(t) := r(t) - x(t)$, and its integral is defined as $e_i(t) = \int e(t)dt$. Recalling the spool dynamics defined in (4.1), we can define the tracking errors' dynamics as:

$$\begin{aligned} \frac{d}{dt}e_i &= e \\ \frac{d}{dt}e &= \dot{r}(t) - \dot{x}(t) = \dot{r}(t) - \frac{Q(u)}{A_s} - w(t) \end{aligned} \tag{4.17}$$

The control effort is composed of two parts: $Q(u) = Q_d + Q_m$. Q_d is the feed-forward control effort, which compensates only for the trajectory: $Q_d = A_s\dot{r}(t)$. The feedback control effort is designed as $Q_m = K_i e_i + K_p e$, which is a typical Proportional Integral controller. With this definition, the error dynamics become:

$$\begin{aligned} \frac{d}{dt}\begin{bmatrix} e_i \\ e \end{bmatrix} &= \begin{bmatrix} 0 & 1 \\ 0 & 0 \end{bmatrix}\begin{bmatrix} e_i \\ e \end{bmatrix} + \begin{bmatrix} 1 \\ -\frac{1}{A_s} \end{bmatrix} Q_m - \begin{bmatrix} 0 \\ 1 \end{bmatrix} w(t) \\ &= \underbrace{\begin{bmatrix} 0 & 1 \\ -\frac{K_i}{A_s} & -\frac{K_p}{A_s} \end{bmatrix}}_{A_{dyn}} \begin{bmatrix} e_i \\ e \end{bmatrix} - \begin{bmatrix} 0 \\ 1 \end{bmatrix} w(t) \end{aligned} \tag{4.18}$$

with $K_i > 0$ and $K_p > 0$. K_i and K_p are computed via the pole-placement technique by making matrix A_{dyn} negative definite.

The control law defines the actuator's flow $Q(u)$. The control input "u" is obtained through an inverted mapping from $Q(u)$ to u, which is calibrated experimentally (as shown in Fig. 4.3). In practice, the mapping from the voltage to the actuator's flow cannot be perfectly inverted, and the dead-band is not known precisely either. The modeling errors are captured by the process noise.

The feedback part of the control law will be implemented with the estimated spool position, which is updated on-line using the Kalman filter (Eqns (4.13) and (4.14)). The stability of the tracking error dynamics and the estimation error dynamics will be investigated for both the discrete LTI model and the periodic time varying model.

Discrete time linear time invariant model

With the discrete time LTI model, the **Separation principle** has been well established [62]. The state feedback controller and the observer can be designed separately, and the set of the eigenvalues of the complete system is the union of the eigenvalues of the state feedback system and the eigenvalues of the observer system. In practice, the poles of the observer system are selected to be faster than the state feedback system.

Periodic time time varying model

On using the periodic time time varying model, the **Separation principle** cannot be directly applied as used for LTI systems. Therefore, we will investigate the convergence of the tracking error and estimation error to zero with a Lyapunov function.

We first design a state estimator for the augmented system defined in Eqn. 4.10. We define the estimation of the spool axial position as $\hat{x}(t)$, and its integration is defined as $\int \hat{x}(t)dt = \hat{x}_i$. We define the estimation of the states representing the periodic measurement noise as $\hat{x}_d \in \mathrm{R}^{N_d x 1}$. We select a continuous time periodic time-varying Kalman filter to estimate the augmented system's states. The Kalman filter is calculated

as:

$$\frac{d}{dt}\begin{bmatrix}\hat{x}_i\\ \hat{x}\\ \hat{x}_d\end{bmatrix} = \underbrace{\left[\begin{array}{cc|c} 0 & 1 & \\ 0 & 0 & 0 \\ \hline 0_{N_d\times N_d} & & 0_{N_d\times N_d}\end{array}\right]}_{A_{aug,kalman}}\begin{bmatrix}\hat{x}_i\\ \hat{x}\\ \hat{x}_d\end{bmatrix} + \underbrace{\begin{bmatrix}0\\ 1\\ 0_{N_d\times N_d}\end{bmatrix}}_{B_{aug,kalman}}\frac{Q}{A_s} + L_{kalman}(t)(y - \underbrace{\begin{bmatrix}0 & 1 & C_d\end{bmatrix}}_{C_{aug,kalman}}\begin{bmatrix}\hat{x}_i\\ \hat{x}\\ \hat{x}_d\end{bmatrix}) \tag{4.19}$$

with

$$L_{kalman}(t) = P_{err}(t)\begin{bmatrix}0 & 1 & C_d\end{bmatrix}^{\mathrm{T}} R_{err}^{-1}$$

where $P_{err}(t)$ denotes the state estimation error covariance matrix. We use R_{err} to denote the covariance of the measurement noise $n(t)$, and we use Q_{err} to denote the covariance of the process noise of the augmented system. The dynamics of state estimation error covariance $P_{err}(t)$ are updated as:

$$\begin{aligned}\dot{P}_{err} &= A_{aug,kalman}P_{err} + P_{err}A_{aug,kalman}^{\mathrm{T}} + B_{aug,kalman}^{\mathrm{T}}Q_{err}B_{aug,kalman} \\ &\quad - P_{err}(t)C_{aug,kalman}^{\mathrm{T}}(t)R_{err}^{-1}C_{aug,kalman}(t)P_{err}(t)\end{aligned} \tag{4.20}$$

Define the estimation error on the spool axial position as $\tilde{e}(t) = x - \hat{x}$, and its integration as $\tilde{e}_i(t) = \int \tilde{e}(t)dt$, and use $\tilde{e}_d = x_d - \hat{x}_d$ to denote the estimation error from the states representing the periodic measurement noise $d(t)$.

The control law will be implemented with the estimated states. Define a Lyapunov function which is quadratic in the state tracking errors and the estimation errors:

$$V_{aug} = \begin{bmatrix}e_i & e\end{bmatrix}^{\mathrm{T}} P_{dyn}\begin{bmatrix}e_i\\ e\end{bmatrix} + \begin{bmatrix}\tilde{e}_i & \tilde{e} & \tilde{e}_d\end{bmatrix}^{\mathrm{T}} P_{err}^{-1}\begin{bmatrix}\tilde{e}_i\\ \tilde{e}\\ \tilde{e}_d\end{bmatrix} \tag{4.21}$$

where P_{dyn} is defined from the solution to the following Lyapunov equation:

$$A_{dyn}^{\mathrm{T}}P_{dyn} + P_{dyn}A_{dyn} = -\mathrm{I}$$

Define $e_{track} = \begin{bmatrix}e_i & e\end{bmatrix}^{\mathrm{T}}$, and $e_{est} = \begin{bmatrix}\tilde{e}_i & \tilde{e} & \tilde{e}_d\end{bmatrix}^{\mathrm{T}}$. The time derivative of V_{aug} becomes:

$$\begin{aligned}\frac{d}{dt}V_{aug} =& -e_i^2 - e^2 + 2\left(B^{\mathrm{T}}P_{dyn}e_{track}\right)\tilde{e} \\ &- e_{est}^{\mathrm{T}}\underbrace{\left[P_{err}^{-1}B_{aug,kalman}Q_{err}B_{aug,kalman}^{\mathrm{T}}P_{err}^{-1} + C_{aug,kalman}^{\mathrm{T}}R_{err}^{-1}C_{aug,kalman}\right]}_{\Gamma_{err}}e_{est}\end{aligned} \tag{4.22}$$

where $B = [0 \quad 1]^{\mathrm{T}}$, and $\Gamma_{err} > 0$. Notice that for some constants α_i and α_e, we can compute the following expression:

$$2\left(B^{\mathrm{T}} P_{dyn} e_{track}\right)\tilde{e} = \alpha_i e_i \tilde{e} + \alpha_e e \tilde{e},$$

and the time derivative of V_{aug} becomes:

$$\frac{d}{dt}V_{aug} = -\begin{bmatrix} e_{track} & e_{est} \end{bmatrix}^{\mathrm{T}} \underbrace{\left(\begin{array}{cc|ccc} 1 & 0 & \alpha_i/2 & 0 & 0 \\ 0 & 1 & 0 & \alpha_e/2 & 0 \\ \hline \alpha_i/2 & 0 & \multicolumn{3}{c}{\multirow{3}{*}{Γ_{err}}} \\ 0 & \alpha_e/2 & \multicolumn{3}{c}{} \\ 0 & 0 & \multicolumn{3}{c}{} \end{array}\right)}_{\Lambda_{aug}} \begin{bmatrix} e_{track} \\ e_{est} \end{bmatrix} \tag{4.23}$$

By properly designing Γ_{err}, Λ_{aug} will be positive definite, and therefore both the tracking errors and the state estimation errors can converge to zero exponentially. This analysis shows that with the periodic noise model, we can also design the estimator and the controller separately, and utilize the estimated spool position in feedback control.

4.5 Simulation and experimental results

The computation cost and the robustness of the discrete approach is constrained by the sampling time, and this approach is not quite practical to be implemented experimentally. Therefore, estimators and controllers derived using the discrete time LTI approach is validated in simulation, and the periodic time varying approach is implemented experimentally.

4.5.1 Simulation Results

A block diagram summarizing the state estimation and the control strategy for spool axial position reference tracking is shown in Fig. 4.7.

The reference spool axial position trajectory described in Eqn. (4.16) is shown in the upper sub-figure of Fig. 4.8, and the periodic noise signal is shown in the upper figure of Fig. 4.9. The periodic measurement noise has a frequency of 25 Hz. Selecting a sampling time of $2ms$, we used 20 states to model the periodic measurement noise's dynamics.

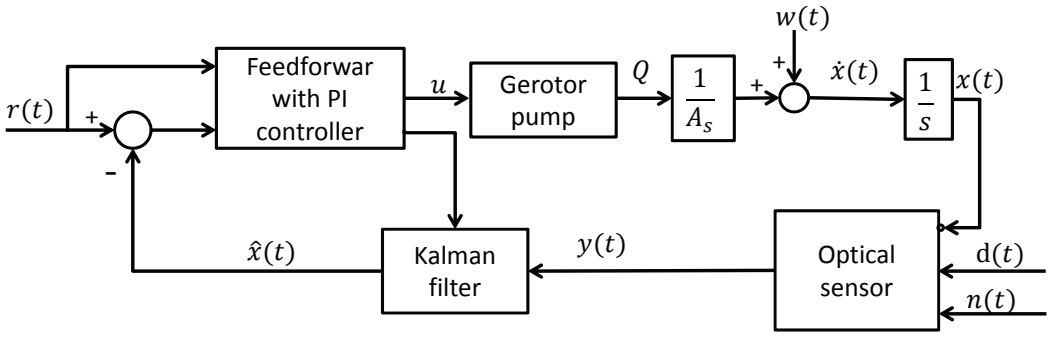

Figure 4.7: System Block Diagram

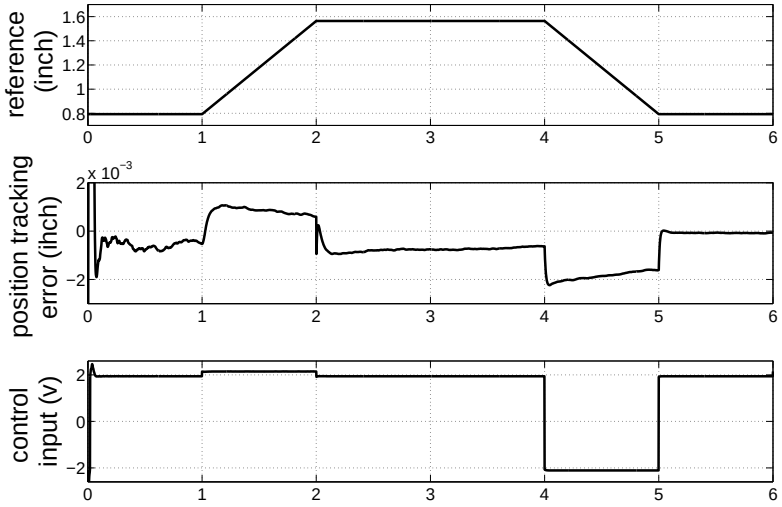

Figure 4.8: Trapezoid reference signal, tracking error, and the control command

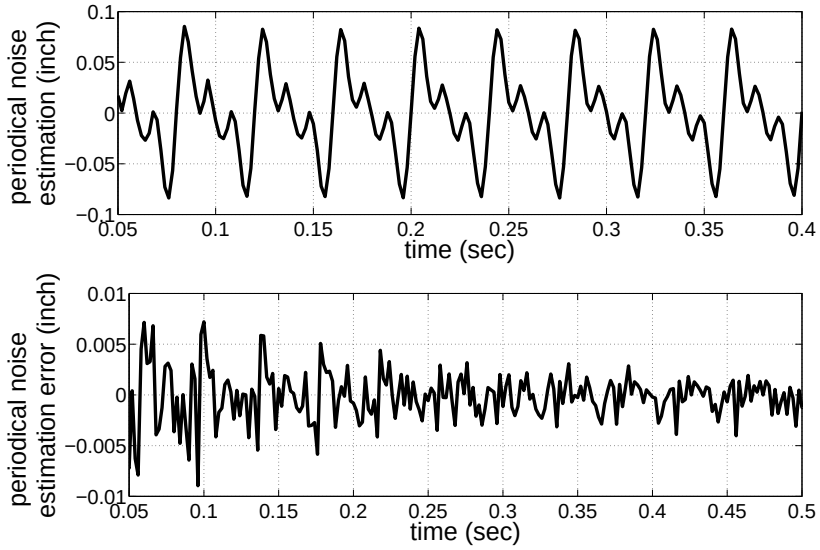

Figure 4.9: Repetitive noise and its estimation error

Using the discrete time time invariant model, the state estimations are calculated following (4.13). The spool position can be distinguished from the periodic measurement noise, and the trajectory tracking performance is satisfactory. If the sampling time is selected to be $1ms$, and the repetitive noise is of $10Hz$ frequency, we would need 100 states to represent this noise.

To investigate the importance of modeling the dynamics of the periodic measurement noise and excluding it from the control effort, a control law without modeling the periodic noise is derived. In this approach, the measurement noise is lumped into one term n_t without considering its temporal structure. Since the system model is a first-order LTI system, a continuous time LTI Kalman filter is selected as the spool's position estimator.

$$\begin{aligned} \dot{x} &= \frac{Q(u)}{A_s}, \qquad y = x + n_t \\ \dot{\hat{x}} &= \frac{Q(u)}{A_s} + L(y - \hat{x}) \end{aligned} \tag{4.24}$$

The same feedforward with PI controller is implemented with the spool position estimated from (4.24), and the spool position tracking performance is compared with the

case when the periodic measurement noise's dynamics are modeled.

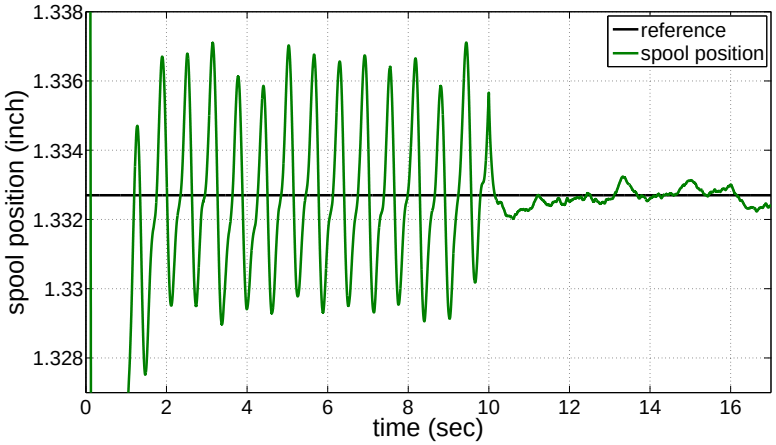

Figure 4.10: Spool tracking error comparison: state estimated from lumped model Kalman filter is fed back in the first 10 sec, and after 10 sec, the state estimated from the basis function Kalman filter is fed back

Figure 4.10 shows the simulation comparison between the lumped estimation model (shown in Eqn. (4.24)) and the periodic basis function model (modeled in Eqn. (4.10)). The lumped model Kalman filter in Eqn. (4.24) is used in the first 10 sec, and the feedback state is switched to the estimated state from the periodic basis function Kalman filter at $t = 10sec$. With the lumped model Kalman filter, the repetitive noise corrupts the estimate of the true spool state, and the actuator responds to the repetitive noise (as shown in Fig. 4.11). This leads to spool oscillations. In contrast, with the periodic basis function Kalman filter, Fig. 4.10 shows that the spool position is regulated to the desired value in the presence of the periodic noise, and the control input does not respond to the periodic noise (Fig. 4.11).

4.5.2 Experimental Results

Since using the continuous time periodic time-varying model (4.7) for the periodic measurement noise can lead to a low dimension system, we implemented this controller and the estimator based on this model experimentally. The periodic measurement noise was modeled using 10 Fourier series basis functions. The reference trajectory in this

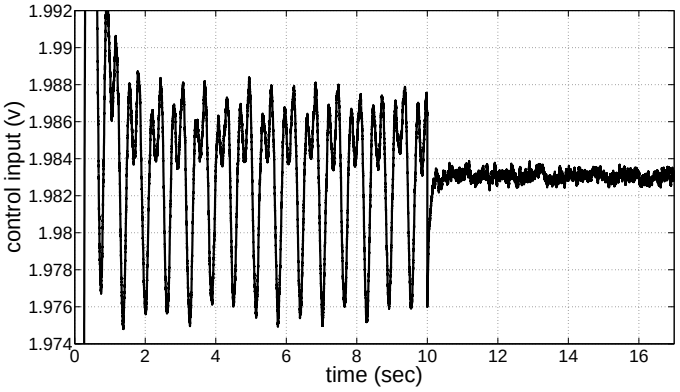

Figure 4.11: Control input comparison between feeding back state from lumped model Kalman filter and feeding back state from basis function Kalman filter

experiment is a constant.

$$d(t) = \sum_{k=1}^{5} [x_{d2k-1} cos(k\omega t) + x_{d2k} sin(k\omega t)] \tag{4.25}$$

The tracking performance is also compared to that with the lumped noise model presented in Eqn. (4.24), which combines the periodic noise and the unstructured noise into one term, n_t.

The position tracking performance and the control effort by using the lumped noise model are shown in Fig. 4.12. In Fig. 4.12(a), the yellow line shows the reference signal, which corresponds to a valve duty ratio of 50%. The green curve is the raw position measurement, and the red curve is the estimation of the spool axial position based on the lumped noise model (Eqn. (4.24)). Since the system model does not capture the dynamics of the periodic measurement noise, the estimation of the spool position cannot converge to the spool position state. As a result, we can observe an oscillation in the spool position's estimation. The control reacts to this estimated spool position and exhibits an oscillating profile, as shown in Fig. 4.12(b). Control input has a frequency twice the spool angular frequency.

In comparison, by implementing the estimator and control law with modeling the periodic measurement noise's dynamics, this oscillation has been reduced considerably. As shown in Fig. 4.13(a), the estimation of the spool position does not have a periodic component. The position tracking error is reduced from 2% using the lumped noise

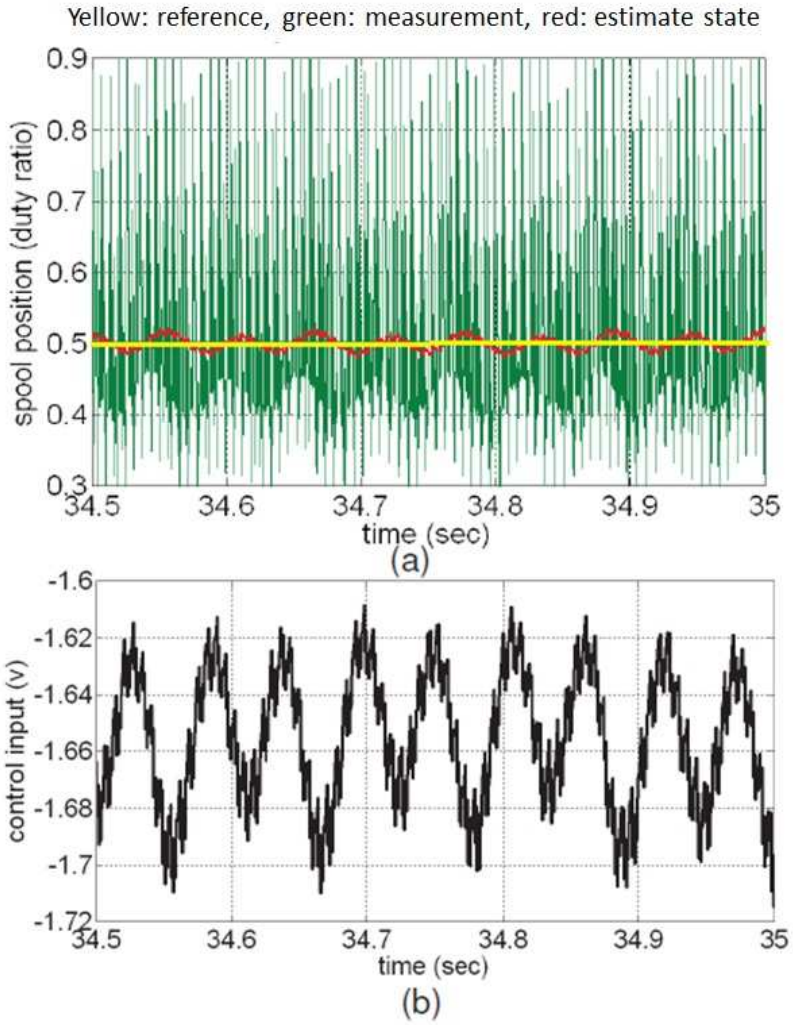

Figure 4.12: Tracking performance with the controller and the estimator derived from the lumped noise model: (a) Spool position tracking (b) control input

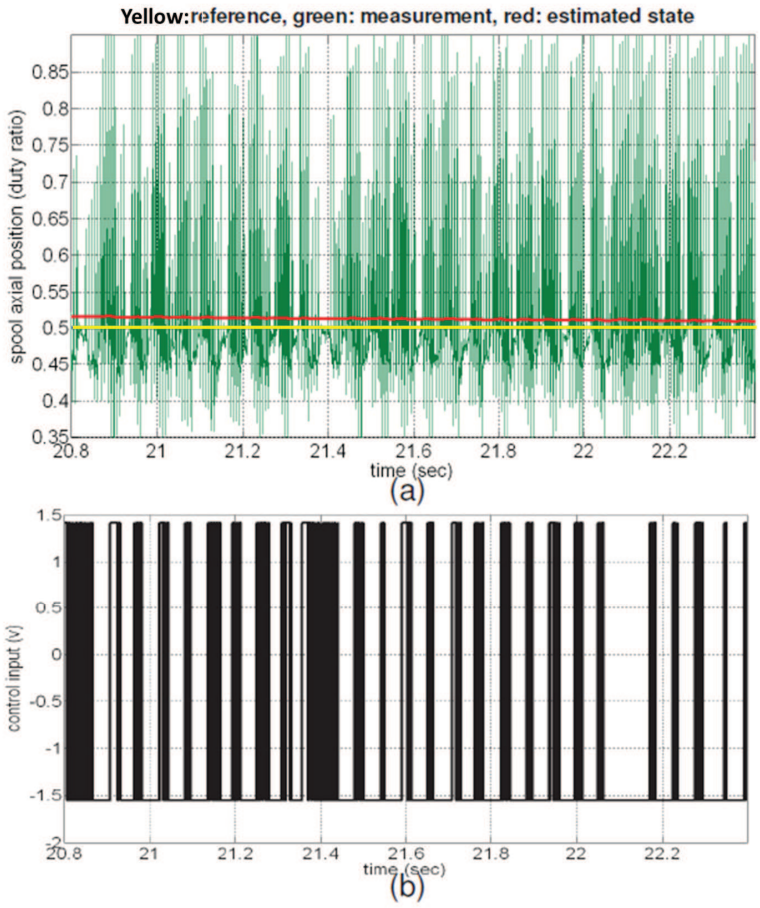

Figure 4.13: Tracking performance with the controller and the estimator derived from the periodic time time-varying model: (a) Spool position tracking (b) control input

model to less than 0.7% using the new model, which is within the actuator's control deadzone. Comparing the control input in this case with the previous one, as shown in Fig. 4.13 (b), the control input in this case mainly oscillates within the deadzone, and little physical energy is provided to the actuator to move the spool. This means the magnitude of the control input is very small because of the small tracking error.

A power spectrum analysis on the control input of both state feedback cases is shown in Fig. 4.14. We can see that when feeding back the state estimated from the lumped Kalman filter, the control input has a significant frequency component at a harmonic of the spool frequency ($\sim 19.53Hz$).

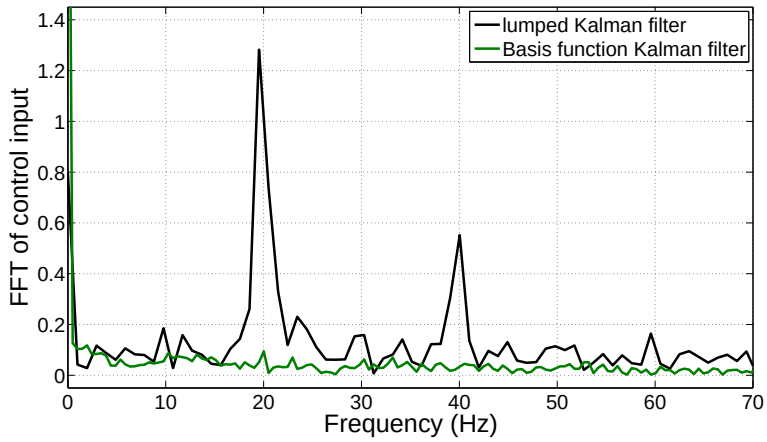

Figure 4.14: FFT analysis on control input

As shown in the experimental results, there is a discrepancy between the estimate of the spool frequency of $10.5Hz$ and the true frequency analyzed using FFT of $9.766Hz$. In practice, the angular velocity of the spool is not measured directly, and it can vary as the oil operating conditions varies. The sensitivity of the periodic noise estimate to the bias of the fundamental frequency is investigated in simulation.

A $0.5Hz$ bias on the fundamental frequency is imposed onto the basis function, while the repetitive noise has a frequency of $10Hz$. As shown in Fig. 4.15, this induces an estimation error on both the repetitive noise and the spool position. This is similar to the problem when using a lumped model Kalman filter. The difference is that estimation error of the spool state is smaller compared with the error using a lumped model Kalman

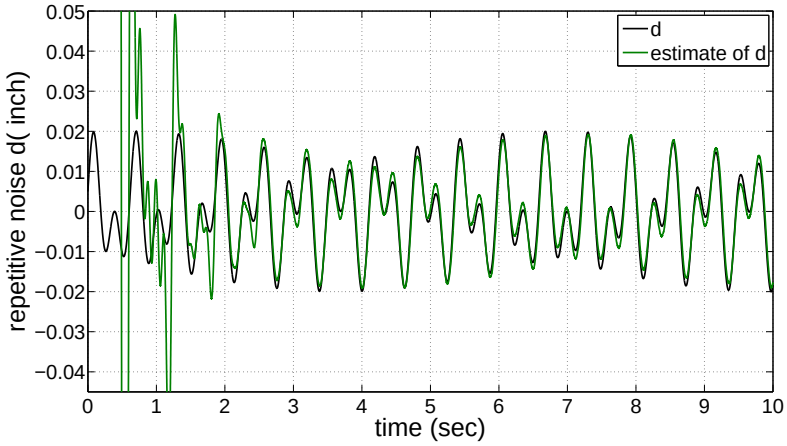

Figure 4.15: Noise estimate with a fundamental frequency bias

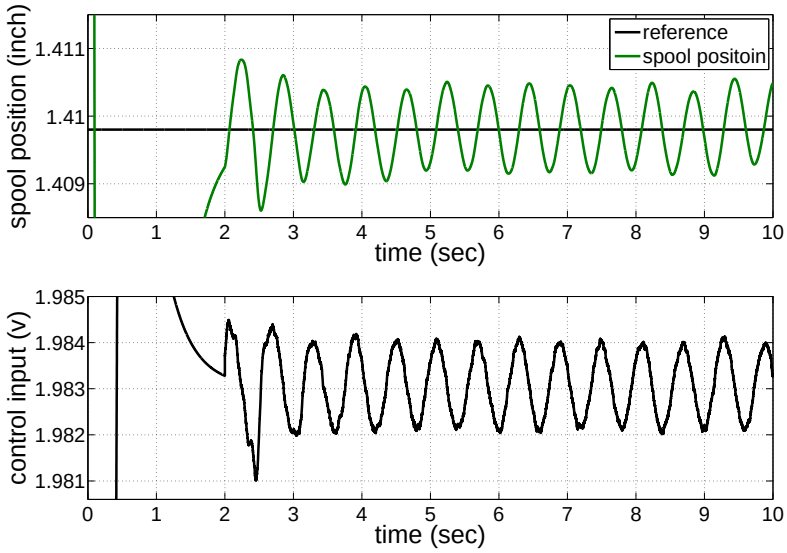

Figure 4.16: Spool position tracking and control input with the fundamental frequency bias

filter. In simulation, the actuator can respond to the state tracking error (shown in Fig. 4.16) fast enough, and the spool can oscillate. In practice, the error may be so small that the actuator input falls into the dead-band, and cannot cause oscillation.

4.6 Summary

Periodic measurement noise can be estimated using state estimators that incorporate models for the periodic noise. In this chapter, we proposed a periodic time varying model for the measurement noise. Compared with the traditional way of treating periodic measurement noise with a time-invariant model, the periodic time varying model leads to a low dimensional system, which is feasible and robust when implemented experimentally.

Sensitivity of the noise model to the dimension of the noise dynamics and the accuracy of the fundamental frequency were investigated in simulation. We can see that knowing the period of the signal is critical in eliminating the effect of the noise.

The focus of this chapter is the modeling of the periodic noise. The spool axial dynamics and the controller are simplified, and robust against modeling errors. The spool axial chamber pressure dynamics will be considered in the next chapter, and this motivates the development of an advanced passivity based controller to guarantee a better and more robust tracking performance.

Chapter 5

Passivity based spool axial position controller in the presence of periodic measurement noise

5.1 Introduction

Chapter 4 focuses on the modeling of the periodic spool axial position measurement noise, so that by utilizing a proper estimator, the true position can be distinguished from the periodic noise and a precise spool position can be obtained for feedback control use. However, two performance drawbacks are observed with the approach in chapter 4. One is that the control bandwidth is slow due to the large gerotor pump inertia. The other is that the controller was designed without considering the fluid pressure dynamics inside the valve sleeve axial chambers. Ignoring the pressure dynamics makes the controller less robust, and the feedback gains are difficult to tune. In addition, the self-spinning feature of our rotary valve ties the PWM frequency with the flow rate crossing the valve, which prevents us from investigating the PWM frequency and the flow rate properties independently. These factors motivate us to pursue an alternate actuation mechanism, which enables the spool rotary speed to be controlled externally. In addition, a more robust spool axial controller is preferred for the externally controlled actuation system.

In this chapter, controls will be developed for an externally driving mechanism for

the rotary spool, instead of for the self-spinning spool. With this new actuation system, the valve spool's rotary motion and the axial motion can be manipulated independently, regardless of the flow passing across it. A similar optical sensing approach will be used to measure the spool axial position. The motivation is to simplify the sealing structure with the installed sensor. A drawback is that periodic noise on the spool axial position is introduced by the spool angular motion. In order to develop an axial positioning (i.e. duty ratio control) controller for the spool, the spool's dynamic model is required. Compared with the model presented in Chapter 4, where only the spool dynamics are considered, the pressure dynamics in the spool axial control chamber will also be considered. With pressure dynamics, the system under control becomes a nonlinear system. Instead of using a typical backstepping control technique to stabilize the spool motion in the axial direction, we incorporate a passivity framework into the backstepping technique so that the natural physical property of this hydraulic system is exploited. The advantage is improved robustness and ease of control design. The control objective is for the actuator position to accurately track a reference trajectory in the presence of a periodic measurement noise.

The rest of this chapter is organized as follows. Section 5.2 will present the external driving mechanism and the corresponding valve spool dynamics. Since the passivity property from the hydraulic system is incorporated into the design of the spool controller, a pressure dependent fluid compressible energy will be discussed in section 5.3. This energy function defines the Lyapunov function associated with the pressure error. With this novel pressure error Lyapunov function term, a passivity based nonlinear controller stabilizing the spool axial position can be derived, and will be presented in section 5.4. As a comparison, a basic backstepping controller will also be derived in section 5.4. Since the measurement of the spool axial position is corrupted by the periodic noise, building an estimator to extract the true plant states from the measurement is important, and this will be discussed in section 5.5. The passivity based controller derived in section 5.4 will then be modified to use the estimated states instead of measured states in section 5.6. Finally, the experimental validation of the new controller will be presented in section 5.7. This chapter will end with a summary and some concluding remarks in section 5.8.

5.2 External driving mechanism

The two degree of freedom (DOF) driving mechanism which can drive the valve spool's rotary and axial motion externally is shown in Fig. 5.1[79][86]. The defining feature of this mechanism is the decoupling of axial and rotary sealing, so that standard O-ring sealing can be applied in both directions. The proposed sealing concept utilizes a translating piston and an intermediate shaft to decouple the rotary and the translational sealing functions. A standard O-ring is used to seal around the rotating shaft, and this seal does not experience any translating motion. The translational sealing function is accomplished using a standard reciprocating piston O-ring seal.

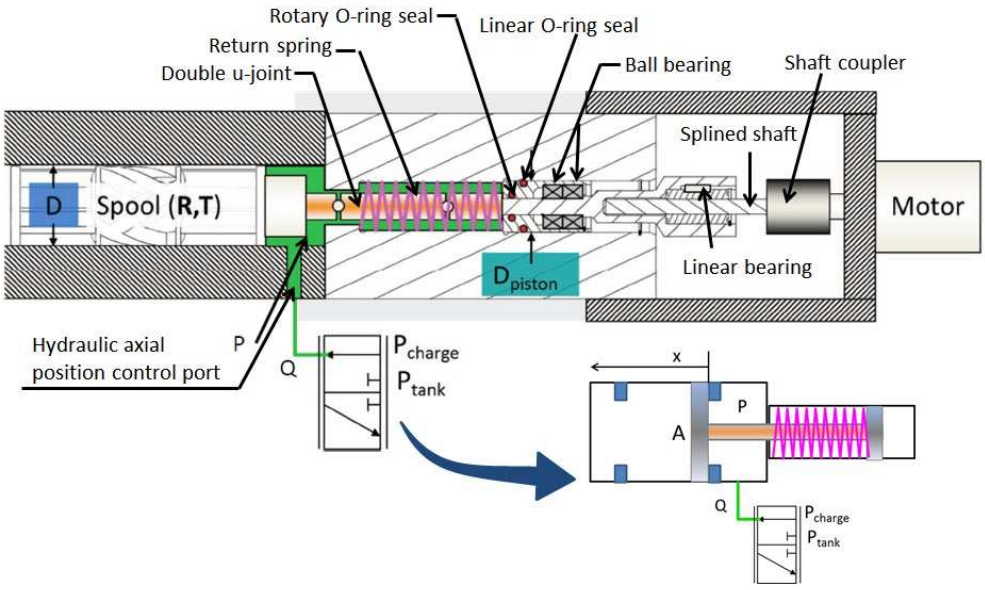

Figure 5.1: Valve spool external driving mechanism

The spool's rotary motion is driven via an electric motor. A flexible shaft coupling is used to connect the motor's shaft to a splined shaft that rotates. The splined shaft allows relative translational motion between the spline and a linear bearing while simultaneously transmitting torque to the bearing. A slotted key is used to transmit torque between the linear bearing and the intermediate shaft, which is connected to the spool via a double u-joint. The double u-joint is required to compensate for the angular and

parallel misalignment between the spool and the intermediate shaft. The hydraulic fluid around the periphery of the spool acts as a journal bearing between the spool and the sleeve. The intermediate shaft is supported by two ball bearings inside of the translating piston.

The axial motion of the spool is driven hydraulically by controlling the pressure in a single chamber. This is accomplished by maintaining an area difference between the spool and the translating piston. As shown in Fig. 5.1, the diameter of the spool is larger than the diameter of the piston. When the axial chamber of the valve is connected with a charge pressure, a net pressure force will be applied to push the spool to the left. The spool pulls on the intermediate shaft with the U-joint, which in turn pulls to the left. The translating piston which in turn compresses the return spring. When the axial chamber is connected with a tank pressure, the return spring will push the translating piston to move to the right. The intermediate shaft then pulls the spool to the right. The design assures that the intermediate shaft, containing the u-joint, is always in tension, so the shaft will not buckle. By controlling the pressure in the valve axial chamber, we can change the spool axial position, and correspondingly change the valve duty ratio. Hard stops are incorporated into the drive mechanism to insure that the spool remains in a specific range of travel. The spool is maintained at the zero duty ratio position via the return spring when the axial control chamber is connected to tank.

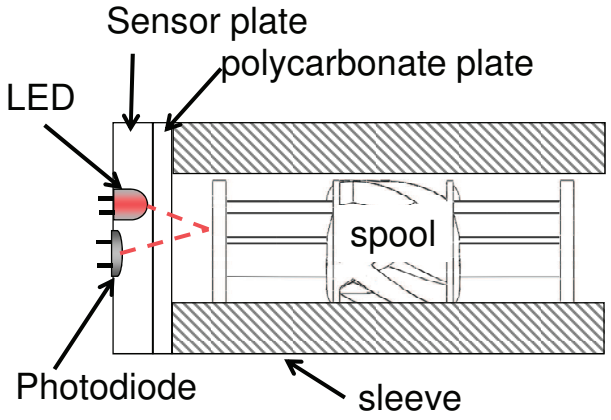

Figure 5.2: Optical sensing configuration

A variety of non-contact as well as contacting sensing approaches have been explored to sense the spool's axial position, which is required for closed-loop control of the valve's duty ratio. Due to its simplicity, as well as former implementation in the self-spinning rotary valve prototype, a non-contact optical sensor described in Chapter 4 is used to sense the valve spool's axial position. A schematic of the sensor is presented in Fig. 5.2. The sensor consists of an LED and a photodiode that are mounted on a sensor plate behind a transparent polycarbonate plate. The polycarbonate plate is used to isolate the sensor from the hydraulic fluid. Light emitted from the LED is reflected off of the spool's end, and is detected by the photodiode. The output of the photodiode exhibits a monotonic relationship with the distance.

In this single chamber hydraulic linear actuator system, the spool and the chamber pressure have the dynamics:

$$\begin{aligned} M\ddot{x} &= AP - K(x + x_0) + F_{load} \\ \dot{P} &= \frac{\beta(P)}{V_0 + Ax}(Q - A\dot{x}) \end{aligned} \tag{5.1}$$

where $M \approx 0.5kg$ is the hydraulic cylinder mass, $A = 1.74cm^2$ is the equivalent piston area (which is the area difference between the spool side and the driving shaft side piston areas), $K \approx 2594N/m$ is the spring constant, $Kx_0 \approx 211.5N$ is the spring pre-load, and $V_0 \approx 60cc$ is the chamber dead volume. $Q(t)$ is the flow entering and exiting the axial chamber, determined by the chamber pressure and the opening of the throttling valve, following the orifice equation:

$$Q(u) = \begin{cases} C_d\sqrt{\frac{2}{\rho}}A_{max}u\sqrt{P_s - P} & u \geq 0 \\ C_d\sqrt{\frac{2}{\rho}}A_{max}u\sqrt{P - P_t} & u < 0 \end{cases} \tag{5.2}$$

where $C_d = 0.62$ is the coefficient of discharge for the proportional valve, and A_{max} is the maximum valve opening area. The magnitude of u models the fraction of the valve opening area, and the sign of u indicates the flow direction across the orifice. $u > 0$ means the flow going from the supply to the work port, and $u < 0$ means to the flow going from the work port back to return. P_s denotes the supplied pressure, and P_t denotes the tank pressure.

5.3 Fluid compressibility, density, energy and passivity

We will exploit a passivity based approach to design the spool axial position controller. In a passivity approach, the storage function associated with the pressure error is modeled based on the fluid compressible energy. This section will define the energy stored in a volume of compressed fluid. Finally, the storage and passivity will be defined for the pressure error.

5.3.1 Compressibility and density function

Assumption 1 (Bulk Modulus): The constitutive relationship of the fluid is defined by its (absolute) pressure-dependent bulk modulus, $\beta : [0, \infty) \to \mathrm{R}^+$, as follows [76]:

$$\frac{d\rho}{\rho} = -\frac{dV}{V} = \frac{dP}{\beta(P)} \tag{5.3}$$

where V and P are the volume and pressure of a fixed fluid mass m and $\rho(P) := \frac{m}{V}$ is the fluid density. We assume that for all $P \in [0, \infty)$,

$$\beta(P) \geq \underline{\beta} > 0 \tag{5.4}$$

Given $\beta(P)$, define the function $g(P_2, P_1)$ as the integral of Eqn (5.4) over the pressure limits P_1 and P_2

$$g(P_2, P_1) := ln\left[\frac{\rho(P_2)}{\rho(P_1)}\right] = \int_{P_1}^{P_2} \frac{dP'}{\beta(P')} \tag{5.5}$$

where $\rho(P)$ is the fluid density at pressure P.

The function $g(P_2, P_1)$ satisfies the group and inverse properties under condition: $\forall P_1, P_2, P_3 \geq 0$,

$$g(P_3, P_2) + g(P_2, P_1) = g(P_3, P_1) \tag{5.6}$$

$$g(P_1, P_2) = g(P_2, P_1) \tag{5.7}$$

Using these properties and the definition (5.5), we have the following results:

Theorem 5.3.1. *Let the pressure-dependent liquid bulk modulus be $\beta(P) > 0$, where $P \in [0, \mathrm{inf})$. Then the pressure-dependent densities $\rho(\cdot)$ at any pressures P, $P_1 \geq 0$ satisfy*

$$\rho(P) = \rho(P_1) \cdot e^{g(P, P_1)} \tag{5.8}$$

Since $g(P,P) = 0$ and $g(P_2, P_1) > 0$ for all $P_2 > P_1, \rho : P \to \rho P$ is a monotonic function. Hence, the inverse function $\rho^{-1}(\cdot)$ exists on the achievable density range.

Proof. Equation (5.8) is obtained by taking the exponential of both sides of Eqn. (5.5). Monotonicity is a consequence of $\beta(\cdot) > 0$ in the integral expression in Eqn. (5.5). □

5.3.2 Compressibility energy

Consider a fluid of mass m in an ambient pressure P_0, its volume V and pressure P are related by:

$$V \cdot \rho(P) = V_0 \cdot \rho_0 = m \tag{5.9}$$

where ρ_0 and V_0 are the density and volume of the fluid at the datum pressure P_0. Excluding the work done by the ambient pressure, the extra work required to compress the fluid from (P_0, V_0) to (P, V) is

$$W(m,P) = -\int_{V_0}^{V} (P^{'} - P_0) dV = \int_{\rho=\rho_0}^{m/V} \frac{(P^{'} - P_0)V}{\rho} d\rho = m \int_{\rho=\rho_0}^{m/V} \frac{(P^{'} - P_0)}{\rho^2} d\rho \tag{5.10}$$

$$= m \int_{P_0}^{P} \frac{(P^{'} - P_0)}{\beta(P^{'})\rho(P^{'})} dP^{'} \tag{5.11}$$

where $m/\rho(P)$ with $\rho(\cdot)$ defined in Eqn. (5.8), $\rho(P)dV = -V d\rho$ (since m is fixed), and the bulk modulus in Eqn. (5.3) was used in the last two equalities. $P^{'}$ is the integration dummy variable. Note that with $P = \rho^{-1}(m/V)$, the work input in (5.11) can be expressed in terms of V as well.

Define $W_v(P_g, P_0)$ and $W_m(P_g, P_0)$ as the volumetric energy density and the gravimetric energy density respectively, at gauge pressure $P_g := P - P_0$, relative to ambient reference pressure P_0 by

$$W_v(P_g, P_0) = \frac{W(m,P)}{V} \tag{5.12}$$
$$W_m(P_g, P_0) = \frac{W(m,P)}{m}$$

Theorem 5.3.2. *Relative to ambient pressure P_0, the volumetric energy density $W_v(P_g, P_0)$ and the gravimetric energy density $W_m(P_g, P_0)$ are given by*

$$W_v(P_g, P_0) = \int_{P_0}^{P} \frac{(P^{'} - P_0)\rho(P)}{\beta(P^{'}\rho(P^{'})} dP^{'} = \int_{P_0}^{P} \left[e^{g(P,P^{'})} - 1 \right] dP^{'} \tag{5.13}$$

$$W_m(P_g, P_0) = \int_{P_0}^{P} \frac{(P' - P_0)}{\beta(P'\rho(P')} dP' = \frac{1}{\rho(P)} \int_{P_0}^{P} \left[e^{g(P,P')} - 1 \right] dP' \tag{5.14}$$

Proof. Since $W_v(P_g, P_0) = W(m, P)/V$ and $W_m(P_g, P_0) = W(m, P)/m$, the first equalities in (5.13) and (5.14) are immediate from (5.11). For the second equality, it is obtained by the substitution

$$\frac{\rho(P)}{\beta(P'\rho(P')} = \frac{e^{g(P,P')}}{\beta P'} = -\frac{de^{g(P,\sigma)}}{d\sigma}\bigg|_{\sigma=P'}$$

and by integrating by parts

$$\begin{aligned} W_v(P_g, P_0) &= -\int_{P_0}^{P} (P' - P_0) \frac{d}{d\sigma} e^{g(P,\sigma)}\bigg|_{\sigma=P'} dP' \\ &= -(P' - P_0) e^{g(P,P')}\bigg|_{P_0}^{P} + \int_{P_0}^{P} e^{g(P,P')} dP' \\ &= -P_g + \int_{P_0}^{P} e^{g(P,P')} dP' \end{aligned} \tag{5.15}$$

□

The second equality in (5.14) is obtained by $W_m(P_g, P_0) = \rho(P) W_V(P_g, P_0))$. Both $W_v(P_g, P_0)$ and $W_m(P_g, P_0)$ are fluid properties that are only dependent on pressures.

Remarks:

1. $W_V(P_g, P_0)$ and $W_m(P_g, P_0)$ are proper energy functions in that $W_V(P_g, P_0) \geq 0$ and $W_m(P_g, P_0) \geq 0$ for all $P = P_g + P_0 \geq 0$, and they are zero when at the ambient pressure: $W_V(P_g, P_0)$ and $W_m(P_g, P_0)$, and are positive definite with respect to the gauge pressure P_g.

2. When the bulk modulus β is a constant, the gravimetric energy density, and the volumetric energy density (relative to P_0) are

$$\rho(P) = \rho_0 e^{(P - P_0)/\beta} \tag{5.16}$$

$$W_v(P_g, P_0) = \beta \left[e^{\frac{P_g}{\beta}} - \left(1 + \frac{P_g}{\beta} \right) \right] \tag{5.17}$$

$$W_m(P_g, P_0) = \frac{\beta}{\rho(P)}\left[e^{\frac{P_g}{\beta}} - \left(1 + \frac{P_g}{\beta}\right)\right] \tag{5.18}$$

where ρ_0 is the fluid density at the ambient pressure P_0. These expressions are compatible with the internal energy function in [87].

3. From the Taylor expansion of Eqn. (5.17) for $|P_g| \ll \beta$, we see that $W_V(P_g, P_0) \approx \frac{P_g^2}{2\beta}$ is essentially a quadratic function of P_g when β is constant. When $\beta(P)$ is pressure dependent, we can define the pressure-dependent mean bulk modulus, $\bar{\beta}(P, P_0)$ to express the energy density quadratically with P_g:

$$\bar{\beta}(P, P_0) := \frac{(P - P_0)^2}{2W_V(P_g, P_0)} \tag{5.19}$$

so that $W_V(P_g, P_0) = P_g^2/(2\bar{\beta}(P, P_0))$.

If $\beta(\cdot)$ is positive and bounded over $[0, P]$, then so is $\bar{\beta}(\cdot, P_0)$. The point and the mean bulk moduli $\beta(P)$ and $\bar{\beta}(P, P_0)$ are plotted in Fig. 5.3, which shows that $\bar{\beta}(P, P_0)$ is much smaller than $\beta(P)$, especially when the level of air entrainment is high.

4. Figure 5.3 also illustrates that typically the point and the mean bulk moduli are non-decreasing functions of pressure. This property can be used to derive some bounds for the mean bulk modulus.

5.3.3 Storage and passivity for the pressure error

After defining the energy stored in a volume of compressed fluid, we will propose a storage function for the pressure error. This will be used for controlling pressure and correspondingly, the cylinder velocity according to some desired reference trajectories.

Let P_d and $r(t)$ denote the reference pressure and the reference velocity. Let the pressure error and the velocity error be defined as:

$$\tilde{P}(t) = P(t) - p_d(t) \tag{5.20}$$

$$e_v(t) = \dot{x}(t) - r(t) \tag{5.21}$$

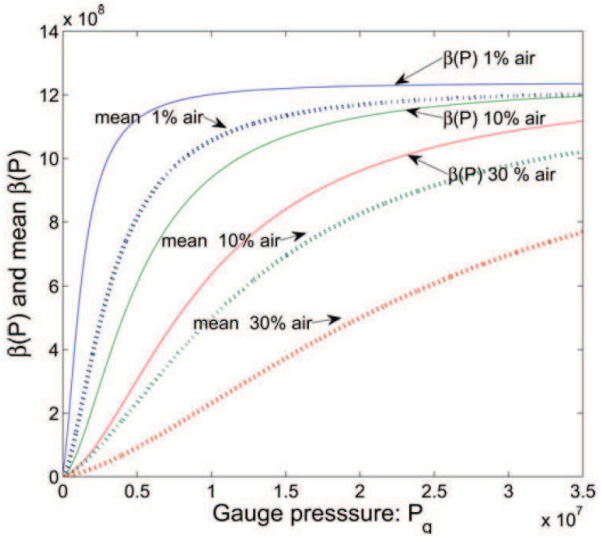

Figure 5.3: Bulk modulus $\beta(P)$ (solid line) and the mean bulk modulus, $\bar{\beta}(P, P_0)$ (dotted lines, defined in (5.19) with $P_0 = 0.1MPa$) at 1%, 10%, and 30% air entrainment. Here, the bulk modulus model based on [88] is used to illustrate the general trend. Other bulk modulus models can also be used.

We define the pressure error storage density $W_V(\tilde{P}, P_d)$ similarly as (5.13) except that the reference pressure $P_d(t)$ is used instead of the ambient pressure:

$$W_V(\tilde{P}, P_d) := \int_{P_d}^{P} \frac{\rho(P)(P' - P_d)}{\rho(P')\beta(P')} dP' = \int_{P_d}^{P} \left[e^{g(P,P')} - 1 \right] dP' \tag{5.22}$$

Similar to $W_V(P_g, P_0)$, $W_V(\tilde{P}, P_d)$ is positive definite with respect to $\tilde{P}$, and can be expressed as a quadratic function in $\tilde{P}$. Hence, following (5.19), we can define the mean bulk modulus over the range $[P_d,\ P]$ as

$$\bar{\beta}(P, P_d) := \frac{(P - P_d)^2}{2W_V(\tilde{P}, P_d)} \tag{5.23}$$

The following proposition establishes the bounds on $\bar{\beta}(P, P_d)$.

Proposition 1: The mean bulk modulus over the range $[P_d,\ P]$ satisfies

$$\bar{\beta}(P, P_d) \leq \max_{\sigma \in [P_d,\ P]} \beta(\sigma) e^{-g(P,P_d)}$$

$$\bar{\beta}(P, P_d) \geq \min_{\sigma \in [P_d,\ P]} \beta(\sigma) e^{-g(P,P_d)}$$

If $\beta(\cdot)$ is monotonically increasing, the above inequalities reduce to:

$$\bar{\beta}(P, P_d) \leq max(\beta(P), \beta(P_d)e^{-g(P,P_d)})$$
$$\bar{\beta}(P, P_d) \geq min(\beta(P), \beta(P_d)e^{-g(P,P_d)})$$

which is equivalent to

$$\beta(P) \geq \bar{\beta}(P, P_d) \geq \beta(P_d)e^{-g(P,P_d)}, \quad if\ P \geq P_d$$
$$\beta(P_d)e^{-g(P,P_d)} \geq \bar{\beta}(P, P_d) \geq \beta(P), \quad if\ P_d \geq P$$

Proof. Using the expression for $W_V(\tilde{P}, P_d)$:

$$W_V(\tilde{P}, P_d) = \int_{p_d}^{P} \frac{e^{g(P,P')}}{\beta(P')}(P' - P_d)dP'$$
$$W_V(\tilde{P}, P_d) \leq \max_{\sigma \in [P_d, P]} \left[\frac{e^{g(P,\sigma)}}{\beta(\sigma)}\right] \frac{\tilde{P}^2}{2}$$
$$W_V(\tilde{P}, P_d) \geq \min_{\sigma \in [P_d, P]} \left[\frac{e^{g(P,\sigma)}}{\beta(\sigma)}\right] \frac{\tilde{P}^2}{2}$$

Therefore,

$$\bar{\beta}(P, P_d) = \frac{\tilde{P}^2/2}{W_V(\tilde{P}, P_d)} \geq \min_{\sigma \in [P_d, P]} \left[\frac{\beta(\sigma)}{e^{g(P,\sigma)}}\right]$$
$$\bar{\beta}(P, P_d) \leq \max_{\sigma \in [P_d, P]} \left[\frac{\beta(\sigma)}{e^{g(P,\sigma)}}\right]$$

□

It shows particularly that $\bar{\beta}(P, P_d)$ is bounded from zero if $\beta(\cdot)$ is, and is close to $\beta(P_d)$ as $P \to P_d$.

Now define the pressure error storage function for a single pressure chamber as:

$$W_P(x, \tilde{P}, P_d) = V(x)W_V(\tilde{P}, P_d) \tag{5.24}$$

For an actuator chamber with volume $V(x)$, cylinder position x, volume pressure P, and the in-flow rate $Q(t)$, recall the pressure dynamics defined in (5.1):

$$\dot{P} = \frac{\beta p}{V(x)}\left[Q - A(x)\dot{x}\right]$$

where $A(x) = \frac{dV}{dx}$ is the effective cylinder piston area. This equation (5.1) can be used to derive the dynamics of the pressure error storage function:

$$\frac{d}{dt}W_P(x,\tilde{P},P_d) = \underbrace{\left[\tilde{P} + W_V(\tilde{P},P_d)\right]}_{\Psi(\tilde{P},P_d)} Q - \tilde{P}A(x)\dot{x} - V(x)\left[e^{g(P,P_d)} - 1\right]\dot{P}_d \qquad (5.25)$$

Note that $\tilde{P}\Psi(\tilde{P},P_d) \geq 0$ for all $\tilde{P}$ if

$$\frac{W_V(\tilde{P},P_d)}{\tilde{P}} = \frac{\tilde{P}}{2\bar{\beta}(P,P_d)} > -1$$

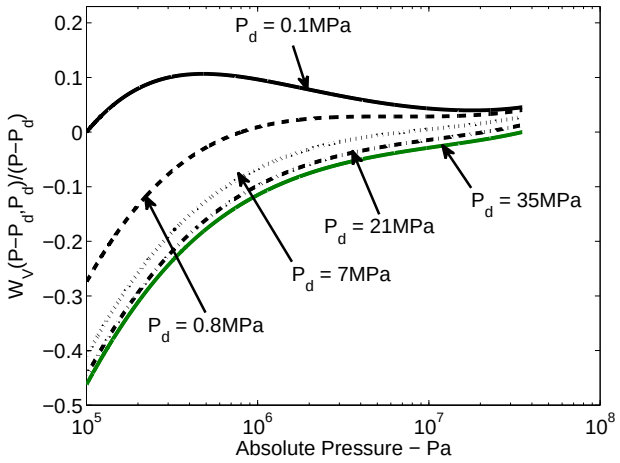

Figure 5.4: $\frac{W_V(\tilde{P},P_d)}{\tilde{P}}$ versus $P = P_d + \tilde{P}$ for various P_d and the entrained air content is 30%

This is indeed the case as established by the following proposition.

Proposition 2: For all $P, P_d \in [0,\ \infty)$,

$$\frac{\tilde{P}}{2\bar{\beta}(P,P_d)} \geq min\left[e^{-g(P_d,P)} - 1, 0\right] > -1$$

it approaches -1 when $P_d \to \infty$ and $P = 0$. Also,

$$\frac{\tilde{P}}{2\bar{\beta}(P,P_d)} \leq max\left[e^{g(P,P_d)} - 1, 0\right] \leq e^{g(P,0)} - 1$$

Proof.

For the lower bound,

$$\frac{\tilde{P}}{2\bar{\beta}(P,P_d)} = \frac{W_V(\tilde{P},P_d)}{\tilde{P}} = \frac{\int_{P_d}^{P}\left[e^{g(P,\sigma)}-1\right]d\sigma}{(P-P_d)}$$
$$\geq \min_{\sigma\in[P_d,P]}\left[e^{g(P,\sigma)}\right]-1 = min[e^{g(P,P)},e^{g(P,P_d)}]-1 = min[0,-(1-e^{g(P_d,P)})]$$

We have used the fact that $g(P,\sigma)$ is monotonically decreasing in σ. The final expression is minimized when $P=0$ and $P_d\to\infty$ as desired. The upper bound is derived in a similar way:

$$\frac{\tilde{P}}{2\bar{\beta}(P,P_d)} \leq \max_{\sigma\in[P_d,P]}\left[e^{g(P,\sigma)}\right]-1 \leq max(0,[e^{g(P,\sigma)}-1])$$

This is maximized when $P_d=0$ and $P\to\infty$. □

Figure. 5.4 illustrates (with the bulk modulus model in [88]) the function $P\mapsto W_V(\tilde{P},P_d)/\tilde{P}$, when the entrained air content is 30% (an extreme case). Note that $W_V(\tilde{P},P_d)/\tilde{P}\to 0$ as $\tilde{P}\to 0$. Moreover, $W_V(\tilde{P},P_d)/\tilde{P}<0$ for $\tilde{P}<0$. As indicated in Proposition 2, $W_V(\tilde{P},P_d)/\tilde{P}$ approaches its smallest value when P_d is large and $P=0$. Even so, this is always greater than -1. Fig. 5.4 shows that over the entire range $P,P_d\in[1,350]$ *bar*, $W_V(\tilde{P},P_d)/\tilde{P}\in[-0.5,1]$. The range is smaller for smaller $\tilde{P}$ or for lower air entrainment.

For a trajectory tracking problem, the reference actuator velocity r and the reference pressure P_d can be determined using a backstepping procedure. The following theorem shows that the function $W_V(\tilde{P},P_d)$ is indeed an appropriate storage function for showing that the pressure error dynamics is a passive 2 port system. It also provides the required control to accommodate the reference velocity and desired pressures.

Theorem 5.3.3. *Using the input flow control law,*

$$Q := \underbrace{A(x)r+\frac{V(x)}{\beta(P)}\dot{P}_d}_{Q_d} - \gamma_P\tilde{P}+\tilde{Q} \tag{5.26}$$

where $A(x)=\frac{dV(x)}{dx}$ *is the cylinder area, with a sufficiently large pressure feedback gain* $\gamma_P>0$*, the error storage function given in* (5.24)*:*

$$W_P(x,\tilde{P},P_d) = V(x)W_V(P,\tilde{P}_d)$$

satisfies the error passivity property

$$\frac{d}{dt}W_P(x,\tilde{P},P_d) \leq \underbrace{\left[\tilde{P}+W_V(\tilde{P},P_d)\right]}_{\Psi(\tilde{P},P_d)}\tilde{Q} - \tilde{P}A(x)e_v \tag{5.27}$$

where e_v is the velocity error in (5.21)*, so that*

$$\int_{t_0}^{t}\left[\Psi(\tilde{P},P_d)\tilde{Q} - \tilde{P}A(x)e_v\right]d\tau \geq -W_P(x(t_0),P(t_0),P_d(t_0))$$

Furthermore, the output function $\Psi(\tilde{P},P_d)$ is a positive function of $\tilde{P}$ in that $\Psi(0,P_d) = 0$ and

$$\tilde{P}\Psi(\tilde{P},P_d) \geq 0$$

Proof.

Q_d in (5.26) is designed from (5.25) by assuming that the pressure error output $\Psi(\tilde{P},P_d) \approx \tilde{P}$, and the $\dot{P}_d$ feedforward gain term $\left[e^{g(P,P_d)}-1\right] \approx \frac{1}{\beta(P_d)}$. Any discrepancies are then handled by the pressure feedback $\gamma_P\tilde{P}$.

To wit, consider the latter approximation. Observe that the $\dot{P}_d$ feedforward gain term in (5.25) can be written, using the mean value theorem, as

$$\left[e^{g(P,P_d)}-1\right] = \left[\frac{e^{g(P,P_d)}}{\beta(\sigma)}\right]\tilde{P} \approx \frac{\tilde{P}}{\beta(P_d)}$$

where $\sigma \in [P_d, P]$. The approximation is obtained by evaluating σ at P_d. The approximation error increases continuously from 0 as σ goes from P_d to P. Therefore, there exists $\mu(P,P_d) \geq 0$ such that

$$\left|\left[\frac{e^{g(\sigma,P_d)}}{\beta(\sigma)}\right] - \frac{1}{\beta(P_d)}\right| \leq \mu(P,P_d)|\tilde{P}|$$

$$\left|\left[e^{g(P,P_d)}-1\right] - \frac{\tilde{P}}{\beta(P_d)}\right| \leq \mu(P,P_d)\tilde{P}^2$$

Let $\tilde{W}_V$ denote $W_V(\tilde{P},P_d)$. Using $\dot{x} = r + e_v$, and the control law (5.26), the error

storage dynamics in (5.25) becomes

$$\begin{aligned}\dot{W}_p &\leq \tilde{P}\left[Q_d - \frac{dV}{dx}r - \frac{V(x)}{\beta(P_d)}\dot{P}_d\right] - \tilde{P}\frac{dV}{dx}e_v + (\mu(P,P_d)|V\dot{P}_d|)\tilde{P}^2 \\ &\quad + \tilde{W}_V Q_d + (\tilde{P} + W_V)(\tilde{Q} - \gamma_P \tilde{P}) \\ &\leq -\tilde{P}A(x)e_v + (\tilde{P} + \tilde{W}_V)\tilde{Q} - \left[\gamma_P\left(1 + \frac{\tilde{W}_V}{\tilde{P}}\right) - (\mu(P,P_d)V\dot{P}_d) - Q_d\frac{\tilde{W}_V}{\tilde{P}^2}\right]\tilde{P}^2\end{aligned}$$

Since $\frac{\tilde{W}_V}{\tilde{P}^2} = \frac{1}{(2\bar{\beta}(P,P_d))}$ is finite and $\frac{\tilde{W}_V}{\tilde{P}} > -1$, we can choose γ_P sufficiently large such that the last term is negative. □

Remarks:

1. Theorem 5.3.3 shows that the pressure error dynamics is a passive two-port subsystem with the mechanical port power being $-A\tilde{P}e_v$, where $A\tilde{P}$ is the force error and e_v is the reference velocity error; and the hydraulic port power being $\Psi(\tilde{P}, P_d)\tilde{Q}$.

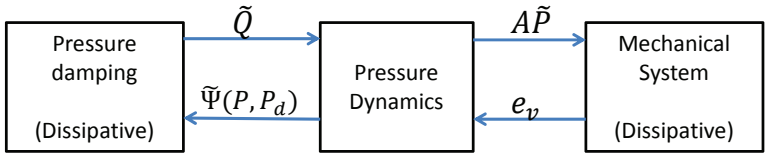

Figure 5.5: Interconnections of compatible passive blocks within the actuator control system

2. If the mechanical system is passive with respect to a compatible supply rate $-A\tilde{P}e_v$, then a cascade of the pressure error with the mechanical system results in a passive system and the $\tilde{P}Ae_v$ term in (5.27) is canceled out by a similar term in the mechanical system supply rate. This interconnection of passive blocks is illustrated in the pressure error dynamics block in Fig. 5.5, and can be stabilized simply by the introduction of damping.

3. The control term in (5.26) consists of three parts: a) a feedforward term; b) a damping term to passify the feedforward term; and c) an additional input. The feedforward term in turn consists of components for r and $\dot{P}_d$. Note that the velocity $\dot{x}$ feedback is **NOT** needed.

4. Since $\Psi(\tilde{P}, P_d)$ is a positive function, $\tilde{Q}$ defined to be a negative function of $\tilde{P}$, will result in further stabilization.

5.4 Valve spool axial position controller

With the development of the compressed fluid energy and the pressure error passivity properties above, we are ready to design a passive control law to manipulate the valve spool axial position, and hence the PWM valve duty ratio. A Desired Compensation Control Law (DCCL) controller[89], which is frequently used in passivity based mechanical robot motion control, was derived to achieve the actuator trajectory tracking, and to define the chamber desired pressure $P_d(t)$.

Assume a trajectory $x_d(t)$ and up to its third time derivative are available, the position tracking error e, the reference velocity r and the reference velocity error e_v are defined as:

$$\begin{aligned} e &:= x - x_d \\ r &:= \dot{x}_d - \lambda_p e \\ e_v &:= \dot{x} - r = \dot{e} + \lambda_p e \end{aligned} \tag{5.28}$$

with $\lambda_p > 0$.

Applying the desired compensation control law (DCCL) [89] to this problem, the desired pressure is obtained as:

$$P_d = \frac{1}{A}\left[M(\ddot{x}_d - \lambda_p \dot{e}) - F_{load} + K(x_d + x_0) - K_p e - K_v e_v\right] \tag{5.29}$$

with $K_p > 0$ and $K_v > 0$.

Applying this desired pressure to the actuator dynamics defined in Eqn. (5.1), we have the following reference velocity error dynamics:

$$M\dot{e}_v = -(K + K_p)e - K_v e_v + A\tilde{P} \tag{5.30}$$

where $\tilde{P} = P - P_d$. Here we define the Lyapunov function related to the mechanical energy part:

$$\begin{aligned} W_{mech} &:= \frac{1}{2}Me_v^2 + \frac{1}{2}(K + K_p)e^2 \\ \frac{dW_{mech}}{dt} &= -K_v e_v^2 - \lambda_p(K + K_p)e^2 + \tilde{P}Ae_v \end{aligned}$$

and the mechanical system is passive with respect to the supply rate $\tilde{P}Ae_v$.

By successively applying Eqn. (5.1) and Eqn. (5.30), we will have:

$$\begin{aligned}\dot{P}_d &= \frac{1}{A}\left[M(\dddot{x}_d - \lambda_p\ddot{e}) - \dot{F}_{load} + K\ddot{x}_d - K_p\dot{e} - K_v\dot{e}_v\right] \\ &= \underbrace{\frac{1}{A}\left[M\dddot{x}_d - \dot{F}_{load} + K\ddot{x}_d\right]}_{\dot{P}_{d1}} + f(e, e_v, \tilde{P}) \end{aligned} \tag{5.31}$$

where $f(e, e_v, \tilde{P}) = \alpha_e e + \alpha_{ev} e_v + \alpha_P \tilde{P}$ for some α_e, α_{ev}, and α_P.

Next, we will take into consideration the pressure dynamics. We will use the proposed passivity approach, discussed in section 5.3. In comparison, we will also derive a controller using the traditional backstepping approach, where the pressure error is treated as a quadratic term.

5.4.1 Passivity approach

Define an augmented Lyapunov function using the proposed pressure error storage function defined in Eqn. (5.24):

$$W_{passive} = \frac{1}{2}Me_v^2 + \frac{1}{2}(K + K_p)e^2 + (V_0 + Ax)W_V(P, P_d) \tag{5.32}$$

The time derivative of the augmented Lyapunov function becomes:

$$\begin{aligned}\frac{d}{dt}W_{passive} &= -K_v e_v^2 - \lambda_p(K + K_p)e^2 + \tilde{P}Ae_v + \tilde{P}Q - \tilde{P}A\dot{x} \\ &\quad + W_V(P, P_d)Q - V(x)\left[e^{g(P,P_d)} - 1\right]\dot{P}_d \\ &= -K_v e_v^2 - \lambda_p(K + K_p)e^2 + \tilde{P}\left[Q_d - Ar - \frac{V(x)}{B(P, P_d)}\dot{P}_d\right] \\ &\quad + W_V(P, P_d)Q_d + \tilde{P}[1 + \frac{W_V(P, P_d)}{\tilde{P}}]\tilde{Q} \end{aligned} \tag{5.33}$$

The control effort Q is defined with two parts: $Q = Q_d + \tilde{Q}$, with the desired flow Q_d compensating the terms only related to the reference trajectory defined as:

$$Q_d = Ar + \frac{V(x)}{\beta(P_d)}\dot{P}_{d1} \tag{5.34}$$

where $r(t)$ defined in Eqn. (5.28) is the reference velocity and $\dot{P}_{d1}$ defined in Eqn. (5.31) is the desired chamber pressure. The time derivative of $W_{passive}$ becomes

$$\frac{d}{dt}W_{passive} \leq -K_v e_v^2 - \lambda_p(K+K_p)e^2 - \tilde{P}\frac{V(x)}{\beta(P_d)}f(e,e_v,\tilde{P}) + \tilde{P}(1+\frac{W_V(\tilde{P},P_d)}{\tilde{P}})\tilde{Q} + \underbrace{(\mu(P,P_d)V(x)\dot{P}_d + \epsilon(P,P_d)|Q_d|)}_{\kappa}\tilde{P}^2 \tag{5.35}$$

where $\mu(P,P_d) > 0$, $\epsilon(P,P_d) > 0$ are defined from:

$$\begin{aligned} \left[e^{g(P,P_d)} - 1\right] &= \frac{1}{B(P,P_d)}\tilde{P} \\ \mu(P,P_d)|\tilde{P}| &\geq |\frac{1}{B(P,P_d)} - \frac{1}{\beta(P_d)}| \\ \epsilon(P,P_d)\tilde{P}^2 &\geq W_V(P,P_d)/\tilde{P}^2 = 1/(2\bar{\beta}(P,P_d)). \end{aligned} \tag{5.36}$$

Note that the term $\tilde{P}Ar_v$ from the mechanical system has been canceled out by the term from the pressure error dynamics by using this passivity based approach.

Next, we design $\tilde{Q} = -\lambda_3\tilde{P}, \lambda_3 > 0$, and the overall control law becomes:

$$Q = Ar + \frac{V(x)}{\beta(P_d)}\dot{P}_{d1} - \lambda_3\tilde{P} \tag{5.37}$$

And the corresponding time derivative of the Lyapunov function becomes:

$$\dot{W}_{passive} \leq -\begin{bmatrix} e & e_v & \tilde{P} \end{bmatrix} \underbrace{\begin{bmatrix} \lambda_p(K+K_p) & 0 & \frac{\alpha_e V(x)}{2\beta(P_d)} \\ 0 & K_v & \frac{\alpha_{ev} V(x)}{2\beta(P_d)} \\ \frac{\alpha_e V(x)}{2\beta(P_d)} & \frac{\alpha_{ev} V(x)}{2\beta(P_d)} & \bar{\lambda}_3 - \kappa + \frac{\alpha_P V(x)}{\beta(P_d)} \end{bmatrix}}_{\Lambda_{passive}} \begin{bmatrix} e \\ e_v \\ \tilde{P} \end{bmatrix} \tag{5.38}$$

with $\bar{\lambda}_3 = \lambda_3\left(1 + \frac{\tilde{W}}{\tilde{P}}\right)$. Hence, selecting λ_3 to be sufficiently large, matrix $\Lambda_{passive}$ is positive definite, and the tracking errors $\begin{bmatrix} e & e_v & \tilde{P} \end{bmatrix}$ converge to $\begin{bmatrix} 0 & 0 & 0 \end{bmatrix}$ exponentially. This implies that the system would be input-to-state stable, and hence robust in the presence of disturbance [36]. Although the control law seems to require $\dot{P}_{d1}$ and the pressure dependent bulk modulus $\beta(P_d)$, ignorance or inaccuracies in the estimation of these terms can be treated as disturbances, which will have small but bounded effects.

5.4.2 Traditional backstepping approach

In a traditional backstepping approach [46][47][60], a quadratic term is utilized to model the pressure error, so that the Lyapunov function is defined to be:

$$\begin{aligned} W_{bkstp} :=& \frac{1}{2}Me_v^2 + \frac{1}{2}(K+K_p)e^2 + \frac{\lambda_2}{2}\tilde{P}^2 \\ \frac{dW_{bkstp}}{dt} =& -K_v e_v^2 - \lambda_p(k+K_p)e^2 + \tilde{P}Ae_v + \lambda_2\tilde{P}\left[\frac{\beta(P)}{V(x)}(Q-A\dot{x}) - \dot{P}_d\right] \end{aligned} \tag{5.39}$$

Design the input flow as:

$$Q = A\dot{x} - \frac{V(x)}{\beta(P)}\left[\frac{Ae_v}{\lambda_2} - \dot{P}_{d1}\right] - \lambda_3(t)\tilde{P} \tag{5.40}$$

Again, correspondingly the time derivative of the Lyapunov function becomes:

$$\dot{W}_{bkstp} \leq -\begin{bmatrix} e & e_v & \tilde{P} \end{bmatrix} \underbrace{\begin{bmatrix} \lambda_p(K+K_p) & 0 & \frac{\alpha_e\lambda_2}{2} \\ 0 & K_v & \frac{\alpha_{ev}\lambda_2}{2} \\ \frac{\alpha_e\lambda_2}{2} & \frac{\alpha_{ev}\lambda_2}{2} & \bar{\lambda}_3(t) + \alpha_P\lambda_2 \end{bmatrix}}_{\Lambda_{bkstp}} \begin{bmatrix} e \\ e_v \\ \tilde{P} \end{bmatrix} \tag{5.41}$$

where

$$\bar{\lambda}_3(t) = \frac{\beta P\lambda_2}{V_0 + Ax}\lambda_3(t)$$

Selecting λ_3 to be sufficiently large, matrix Λ_{bkstp} will become positive define, and the tracking errors converge to zero exponentially.

The basic backstepping control in (5.40) differs from the passivity-based control in (5.37) in the following ways, which establishes the advantages of the passivity-based approach.

1. Actuator volume and the bulk modulus are needed only for the feedforward term for the passivity-based control (5.37), but are needed for both the feedback and feedforward terms for the basic backstepping control (5.40). The former may have some advantage for adaptation in the presence of measurement noise.

2. The treatment of the piston velocity is different. In the passivity-based approach, only the reference velocity r is used; whereas in the traditional backstepping approach, the actual piston velocity $\dot{x}$ is actively canceled, and the velocity error e_v is fed back. Intuitively, the $\dot{x}$ term has a positive feedback effect as $\dot{x}$ has a positive

effect on input flow Q which in turn has a positive effect on piston velocity. The negative feedback of e_v has the purpose of stabilizing this effect.

3. Equation (5.40) provides an additional gain λ_2 for tuning. It will be equivalent to (5.37) if $\lambda_2 \approx \frac{(V_0+Ax)}{\beta(P)}$ and similar $\lambda_3(t)$ are chosen for both. However, this requires knowledge of the system parameters. Moreover, since λ_2 must be a constant in (5.40), this equivalence can only be approximated. In the later section, sec 5.7, experimental results indicate that λ_2 chosen as $\frac{V}{\beta P}$ results in the smallest tracking error.

5.5 Estimation of the augmented system states

If the spool axial position can be directly measured, the passive control provided in (5.37) from the previous section can be implemented directly with the measurement. However, when the spool is spinning and traveling axially simultaneously, the measurements of spool axial position and velocity are corrupted by a periodic noise, and a similar problem has been illustrated in chapter 4. In this section, we will focus on developing an estimator to estimate the spool position and velocity from a noisy position measurement, which will be used in the passive controller.

We will use the periodic time varying model to model the measurement noise, and these dynamics will be augmented with the spool dynamics defined in sec 5.5.1. The observability of the augmented system will be discussed in sec 5.5.2. Finally, a periodic time varying Kalman filter will be presented to estimate the states of the augmented system in sec 5.5.3.

5.5.1 Augmented system dynamics

Consider the dynamics of the spool's axial position:

$$M\ddot{x} = AP - K(x + x_0) + F_{load}$$

The two states defined here are the spool axial position x_1 and the spool axial velocity x_2:

$$\underbrace{\frac{d}{dt}\begin{bmatrix} x_1 \\ x_2 \end{bmatrix}}_{x_s} = \underbrace{\begin{bmatrix} 0 & 1 \\ -\frac{K}{M} & 0 \end{bmatrix}}_{A_s} \begin{bmatrix} x_1 \\ x_2 \end{bmatrix} + \underbrace{\begin{bmatrix} 0 \\ 1 \end{bmatrix}}_{B_s} \underbrace{\frac{Ap - Kx_0 + F_{load}}{M}}_{u} \tag{5.42}$$

Due to the rotary motion of the valve spool, the axial position measurement is corrupted by a periodic noise x_n: $y = x_1 + x_n$. Here we model the periodic noise using the periodic time varying model:

$$\begin{aligned} x_n =& C_d(t) \cdot x_d \\ C_d(t) =& \begin{bmatrix} \cos\omega t & \sin\omega t & \cos 2\omega t & \sin 2\omega t & \cdots & \cos k\omega t & \sin k\omega t \end{bmatrix} \\ x_d =& \begin{bmatrix} x_{n1} & x_{n2} & x_{n3} & x_{n4} & \cdots & x_{n(k-1)} & x_{nk} \end{bmatrix} \end{aligned} \tag{5.43}$$

Augmenting the cylinder mass dynamics with the periodic noise, we have:

$$\begin{aligned} \underbrace{\frac{d}{dt}\begin{bmatrix} x_s \\ x_d \end{bmatrix}}_{x_{aug}} &= \underbrace{\left[\begin{array}{c|c} A_s & 0_{2\times 2k} \\ \hline 0_{2k\times 2} & 0_{2k\times 2k} \end{array}\right]}_{A_{aug}} \begin{bmatrix} x_s \\ x_d \end{bmatrix} + \underbrace{\begin{bmatrix} B_s \\ 0_{2k\times 1} \end{bmatrix}}_{B_{aug}} u \\ y &= \underbrace{\begin{bmatrix} 1 & 0 & C_d(t) \end{bmatrix}}_{C_{aug}(t)} x_{aug} \end{aligned} \tag{5.44}$$

$C_{aug}(t)$ is a periodic time varying vector; therefore the augmented system is a periodic time varying system. The question we pose next is whether this augmented system is observable.

5.5.2 Augmented System Observability

The observability of the augmented system defined in Eqn. (5.44) is evaluated via the determinant of the observability grammian. A linear system is observable on $[t_0, t_f]$ if and only if the observability grammian is invertible [85], which is equivalent to the observability grammian matrix being of full rank. Given a periodic system, the observability is checked for one period [85].

Without loss of generality, we set $t_0 = 0$, define $T = \frac{2\pi}{\omega}$ as the period, and the time

interval as $[0, T]$. The observability grammian is calculated as:

$$M(0,T) = \int_0^T m(0,t)dt = \int_0^T \Phi^{\mathrm{T}}(t) C_{aug}^{\mathrm{T}}(t) C_{aug}(t) \Phi(t) dt \tag{5.45}$$

$$M(0,T) = \begin{bmatrix} \Psi & L \\ L^{\mathrm{T}} & \frac{T}{2} I_{2k \times 2k} \end{bmatrix}, \Psi \in \mathbb{R}^{2\times 2}, L \in \mathbb{R}^{2 \times 2k} \tag{5.46}$$

$\Psi = \begin{bmatrix} \Psi_{11} & \Psi_{12} \\ \Psi_{12} & \Psi_{22} \end{bmatrix}$, with Ψ_{11}, Ψ_{12}, and Ψ_{22} calculated as:

$$\begin{aligned} \Psi_{11} &= \frac{T}{2} + \frac{\sin 2\gamma T}{4\gamma} \\ \Psi_{12} &= \frac{1 - \cos 2\gamma T}{4\gamma^2} \\ \Psi_{22} &= \frac{1}{\gamma^2}\left(\frac{T}{2} + \frac{sin 2\gamma T}{4\gamma}\right) \end{aligned} \tag{5.47}$$

The detailed calculation of the observability grammian is presented in Appendix A.1.

Manipulating the block matrix to reduce the order of the matrix being calculated, the following relationship holds:

$$\operatorname{rank}(M(0,t)) = \operatorname{rank}\left(\begin{bmatrix} \Psi & L \\ L^{\mathrm{T}} & \frac{T}{2} I \end{bmatrix}\right) = \operatorname{rank}\left(\begin{bmatrix} \frac{T}{2} I & L^{\mathrm{T}} \\ L & \Psi \end{bmatrix}\right) \tag{5.48}$$

Whether the augmented system is observable is equivalent to the question of whether the new matrix $\begin{bmatrix} \frac{T}{2} I & L^{\mathrm{T}} \\ L & \Psi \end{bmatrix}$ is full rank, and this is equivalent to checking whether the matrix is non-singular:

$$\det \begin{bmatrix} \frac{T}{2} I & L^{\mathrm{T}} \\ L & \Psi \end{bmatrix} = \det\left(\frac{T}{2} I\right) \cdot \det\left(\Psi - \frac{2}{T} L L^{\mathrm{T}}\right) \tag{5.49}$$

Now we are ready to define the conditions which determine the augmented system observability.

Theorem 5.5.1. *The augmented system defined in Eqn.* (5.44) *is observable* iff $\frac{2}{T}$ is *NOT an eigenvalue of the matrix pencil*[1] $\Psi - \lambda LL^{\mathrm{T}}$, *with* $\lambda \in \mathbb{C}$.

Proof. If the augmented system in Eqn. (5.44) is observable, the observability grammian $M(0,T)$ is invertible, and $\det(M(0,T)) \neq 0$:

$$\det(M(0,T)) = \det \begin{bmatrix} \frac{T}{2}I & L^{\mathrm{T}} \\ L & \Psi \end{bmatrix} = \det\left(\frac{T}{2}I\right) \cdot \det\left(\Psi - \frac{2}{T}LL^{\mathrm{T}}\right) \neq 0$$

$$\rightarrow \frac{2}{T} \text{ is not an eigenvalue of the matrix pencil } \Psi - \lambda LL^{\mathrm{T}} \tag{5.50}$$

$$\det\left(\Psi - \frac{2}{T}LL^{\mathrm{T}}\right) \neq 0 \rightarrow \det\left(\frac{T}{2}I\right) \cdot \det\left(\Psi - \frac{2}{T}LL^{\mathrm{T}}\right) \neq 0 \rightarrow \det \begin{bmatrix} \frac{T}{2}I & L^{\mathrm{T}} \\ L & \Psi \end{bmatrix} \neq 0$$

$$\text{augmented system (5.44) is observable} \tag{5.51}$$

□

If the conditions are met, the augmented system is observable, and all the system states can be uniquely determined using a proper estimator.

5.5.3 Augmented system state estimator

A periodic time varying Kalman filter is developed to estimate the states of the augmented system (Eqn. (5.44)):

$$\dot{\hat{x}}_{aug} = A_{aug}\hat{x}_{aug} + B_{aug}u + L_{aug}(t)\left[y - C_{aug}(t)\hat{x}_{aug}\right] \tag{5.52}$$

with the estimator output injection gain $L_{aug}(t)$ computed based on a continuous time periodic Riccati equation:

$$L_{aug}(t) = P_{Err}C_{aug}^{\mathrm{T}}(t)R_c^{-1}$$
$$\dot{P}_{Err} = -P_{Err}C_{aug}^{\mathrm{T}}(t)R_c^{-1}C_{aug}(t)P_{Err} + A_{aug}P_{Err} + P_{Err}A_{aug}^{\mathrm{T}} + Q_c \tag{5.53}$$

[1] *Let A and B be two n-by-n matrices. The set of all matrices of the form $A - \lambda B$ with $\lambda \in \mathbb{C}$ is said to be a* ***pencil***. *The eigenvalues of the pencil are elements of the set $\lambda(A,B)$ defined by $\lambda(A,B) = \{z \in \mathbb{C} : \det(A - zB) = 0\}$. If $\lambda \in \lambda(A,B)$ and $Ax = \lambda Bx \;\; x \neq 0$, then x is referred to as an eigenvector of $A - \lambda B$.[90](section 7.7)*

where $P_{Err}(t)$ denotes the estimation error covariance matrix, $R_c \in \mathrm{R}^{1\times 1}$ quantifies the variance of the unstructured measurement noise, and $Q_c \in \mathrm{R}^{(k+2)\times(k+2)}$ quantifies the variance of the unstructured process noise. Both R_c and Q_c are positive definite.

The estimator injection gain $L_{aug}(t)$ is designed following a standard periodic time varying Kalman filter[91], and the following analysis establishes the effectiveness of the Kalman filter:

Theorem 5.5.2. *Given a system defined in Eqn.* (5.44)*, and an estimator defined in Eqn.* (5.52)*, define* $\tilde{x}_{aug} = x - \hat{x}_{aug}$ *as the state estimation error, and the error dynamics are:*

$$\dot{\tilde{x}} = (A_{aug} - L_{aug}C_{aug})\tilde{x} \tag{5.54}$$

$\tilde{x} = 0$ *is Lyapunov stable. The stability can be proved using a Lyapunov function:*

$$V(\tilde{x}) = \tilde{x}^{\mathrm{T}} P_{Err}(t)^{-1}\tilde{x} \tag{5.55}$$

with $P_{Err}(t)$ *being the estimation error covariance matrix.*

Proof. Take the time derivative of the Lyapunov function defined in Eqn. (5.55):

$$\dot{V}(\tilde{x}) = \dot{\tilde{x}}^{\mathrm{T}} P_{Err}(t)^{-1}\tilde{x} + \tilde{x}^{\mathrm{T}} P_{Err}(t)^{-1}\dot{\tilde{x}} - \tilde{x}^{\mathrm{T}} P_{Err}^{-1}\dot{P}_{Err}P_{Err}^{-1}\tilde{x} \tag{5.56}$$

Substitute in the relationship defined in Eqn. (5.53) and Eqn. (5.54):

$$\begin{aligned}\dot{V}(\tilde{x}) = \tilde{x}^{\mathrm{T}}\Big[&(A_{aug} - L_{aug}C_{aug})^{\mathrm{T}} P_{Err}^{-1} + P_{Err}^{-1}(A_{aug} - L_{aug}C_{aug}) - P_{Err}^{-1}A_{aug} - A^{\mathrm{T}}P_{Err}^{-1} \\ &+ P_{Err}^{-1}Q_c P_{Err}^{-1} + C_{aug}^{\mathrm{T}}R^{-1}C_{aug}\Big]\tilde{x} \\ = -\tilde{x}^{\mathrm{T}}&\underbrace{\left[P_{Err}^{-1}Q_c P_{Err}^{-1} + C_{aug}^{\mathrm{T}}R^{-1}C_{aug}\right]}_{\Lambda_{\tilde{x}}}\tilde{x}\end{aligned} \tag{5.57}$$

$\Lambda_{\tilde{x}}$ is positive definite in $\tilde{x}$, and therefore $\dot{V}(\tilde{x}) < 0$ when $\tilde{x} \neq 0$, and $\dot{V} = 0$ only when $\tilde{x} = 0$. We can conclude that $\tilde{x} = 0$ is a global asymptotically stable point. □

5.6 Passive controller implemented with estimated states

In this section, we will exploit the stability of the passive control defined in Eqn. (5.37) when it is implemented with the spool estimation of the spool axial position and velocity instead of the direct measurements.

Recall the definition from the previous section. To make the derivation easier to follow, we define the cylinder position estimation error as e_1, and the cylinder velocity estimation error as e_2, which corresponds to the first two elements from (5.54). We will re-define the position tracking error e_n, the reference velocity r_n, and the reference velocity error e_{vn} using the estimated cylinder position x_{est}.

$$e_n := x_{est} - x_d; \quad r_n := \dot{x}_d - \lambda_p e_n; \quad e_{vn} := \dot{x}_{est} - r_n = e_n + \lambda_p e_n \tag{5.58}$$

with $\lambda_p > 0$. These variables are related to the tracking error variables defined in (5.28) as follows:

$$e = e_n + e_1; \quad r = r_n - \lambda_p e_1; \quad e_v = e_{vn} + (e_2 + \lambda_p e_1) \tag{5.59}$$

With the new tracking errors which are defined with the reference signals and the estimates of the spool position and velocity, we will redefine the desired pressure and the Lyapunov function for the mechanical part. Firstly, the desired pressure defined in Eqn. (5.29) becomes:

$$P_{dn} = \frac{1}{A}\left[M(\ddot{x}_d - \lambda_p \dot{e}_n) - F_{load} + K(x_d + x_0) - K_p e_n - K_v e_{vn}\right]$$

With this desired pressure, the velocity error dynamics defined in Eqn. (5.30) becomes:

$$M\dot{e}_{vn} = -(K + K_p)e_n - K_v e_{vn} + A\tilde{P}_n - M\dot{e}_2 - Ke_1 \tag{5.60}$$

with $\tilde{P}_n = P - P_{dn}$.

We re-define the Lyapunov function related to the mechanical energy part as:

$$\begin{aligned} W_{mech,n} &: = \frac{1}{2}Me_{vn}^2 + \frac{1}{2}(K + K_p)e_n^2 \\ \frac{dW_{mech,n}}{dt} &= -K_v e_{vn}^2 - \lambda_p(K + K_p)e_n^2 + \tilde{P}_n A e_{vn} - \dot{e}_2 M e_{vn} - e_1 K e_{vn} \end{aligned} \tag{5.61}$$

The dynamics of the desired pressure is obtained as:

$$\begin{aligned} \dot{P}_{dn} &= \frac{1}{A}\left[M(\dddot{x}_d - \lambda_p \ddot{e}_n) - \dot{F}_{load} + K\dot{x}_d - K_p\dot{e}_n - K_v\dot{e}_{vn}\right] \\ &= \underbrace{\frac{1}{A}\left[M\dddot{x}_d - \dot{F}_{load} + K\dot{x}_d\right]}_{\dot{P}_{d1}} + f(e_n, e_{vn}, \tilde{P}_n) \end{aligned} \tag{5.62}$$

where

$$f(e_n, e_{vn}, \tilde{P}_n) = \alpha_e e_n + \alpha_{ev} e_{vn} + \alpha_P \tilde{P}_n$$

for some α_e, α_{ev}, α_P, α_1, and α_2.

Now augment the Lyapunov function with the proposed pressure error energy density function:

$$W_{passive,n} = \frac{1}{2} M e_{vn}^2 + \frac{1}{2}(K + K_p) e_n^2 + (V_0 + A x_{est}) W_V(P, P_d) \tag{5.63}$$

Designing the control effort $Q = Q_{dn} + \tilde{Q}_n$, we will have:

$$\begin{aligned}
\frac{d}{dt} W_{passive,n} &= -K_v e_{vn}^2 - \lambda_p (K + K_p) e_n^2 + \tilde{P}_n A e_{vn} - \dot{e}_2 M e_{vn} - e_1 K e_{vn} \\
&\quad + \tilde{P}_n Q - \tilde{P}_n A \dot{x}_{est} + W_V(P, P_{dn}) Q - V(x_{est}) \left[e^{g(P, P_{dn})} - 1 \right] \dot{P}_{dn} \\
&= -K_v e_{vn}^2 - \lambda_p (K + K_p) e_n^2 - \dot{e}_2 M e_{vn} - e_1 K e_{vn} \\
&\quad + \tilde{P}_n \left[Q_{dn} - A r_n - \frac{V(x_{est})}{B(P, P_{dn})} \dot{P}_{dn} \right] + W_V(P, P_{dn}) Q_{dn} \\
&\quad + \tilde{P}_n [1 + \frac{W_V(P, P_{dn})}{\tilde{P}_n}] \tilde{Q}_n
\end{aligned} \tag{5.64}$$

with $B(P, P_{dn}) = \tilde{P}_n / [e^{g(P, P_{dn})} - 1]$.

Again design the desired flow Q_{dn} to compensate the term related to the reference trajectory with variables defined using the estimated states:

$$Q_{dn} = A r_n + \frac{V(x_{est})}{\beta(P_{dn})} \dot{P}_{d1} \tag{5.65}$$

and the derivative of $W_{passive,n}$ becomes:

$$\begin{aligned}
\frac{d}{dt} W_{passive,n} \leq & - K_v e_{vn}^2 - \lambda_p (K + K_p) e_n^2 - \tilde{P}_n \frac{V(x_{est})}{\beta(P_{dn})} f(e_n, e_{vn}, \tilde{P}_n) \\
& + \tilde{P}_n (1 + \frac{W_V(P, P_{dn})}{\tilde{P}_n}) \tilde{Q}_n \\
& + \underbrace{(\mu(P, P_{dn}) V(x_n) \dot{P}_{dn} + \epsilon(P, P_{dn}) |Q_{dn}|)}_{\kappa_n} \tilde{P}_n^2 \underbrace{-\dot{e}_2 M e_{vn} - e_1 K e_{vn}}_{g(e_1, e_2) \cdot e_{vn}}
\end{aligned} \tag{5.66}$$

where $g(e_1, e_2) = \alpha_1 e_1 + \alpha_2 e_2$ for some α_1, α_2, and $\mu(P, P_{dn}) > 0$, $\epsilon(P, P_{dn} > 0$ are defined from

$$\begin{aligned}
\mu(P, P_{dn}) |\tilde{P}_n| &\geq |\frac{1}{B(P, P_{dn})} - \frac{1}{\beta(P_{dn})}| \\
\epsilon(P, P_{dn}) \tilde{P}_n^2 &\geq W_V(\tilde{P}_n, P_{dn}) = \frac{1}{2\bar{\beta}(P, P_{dn})}
\end{aligned}$$

Finally design $\tilde{Q}_n = -\lambda_3 \tilde{P}_n$, and the overall control law is:

$$Q = Ar_n + \frac{V(x_{est})}{\beta(P_{dn})}\dot{P}_{d1} - \lambda_3 \tilde{P}_n \tag{5.67}$$

Augment the Lyapunov function so far ($W_{passive,n}$) with the estimation error part to define the total Lyapunov function, and recall the estimation errors $\tilde{x}$ defined in 5.5.2 i.e. $\begin{bmatrix} e_1 & e_2 & \cdots & e_n \end{bmatrix}$:

$$W_{total,n} = \frac{1}{2}Me_{vn}^2 + \frac{1}{2}(K + K_p)e_n^2 + (V_0 + Ax_{est})W_V(P, P_d) + \tilde{x}P_{Err}^{-1}\tilde{x} \tag{5.68}$$

where $P_{Err}(t) > 0$ is the estimation covariance matrix. Denoting $V_\beta = V_(x_{est})/2\beta(P_{dn})$, the time derivative of $W_{total,n}$ becomes:

$$\begin{aligned}
&\dot{W}_{total,n} \\
&\leq -\begin{bmatrix} e_n & e_{vn} & \tilde{P}_n & e_1 & e_2 & \cdots & e_n \end{bmatrix} \underbrace{\left(\begin{array}{ccc|cccc} & & & 0 & 0 & \cdots & 0 \\ & & & \frac{\alpha_1}{2} & \frac{\alpha_2}{2} & 0 & \cdots \\ \multicolumn{3}{c|}{\Lambda_{pass,n}} & 0 & 0 & \cdots & 0 \\ \hline 0 & \frac{\alpha_1}{2} & 0 & \multicolumn{4}{c}{} \\ 0 & \frac{\alpha_2}{2} & 0 & \multicolumn{4}{c}{} \\ \vdots & 0 & \vdots & \multicolumn{4}{c}{\Lambda_{err}} \\ 0 & \vdots & 0 & \multicolumn{4}{c}{} \end{array}\right)}_{\Lambda_{total}} \begin{bmatrix} e_n \\ e_{vn} \\ \tilde{P}_n \\ e_1 \\ e_2 \\ \vdots \\ e_n \end{bmatrix}
\end{aligned} \tag{5.69}$$

with

$$\Lambda_{pass,n} = \begin{bmatrix} \lambda_p(K + K_p) & 0 & \alpha_e V_\beta \\ 0 & K_v & \alpha_{ev} V_\beta \\ \alpha_e V_\beta & \alpha_{ev} V_\beta & \bar{\lambda}_3 - \kappa_n + 2\alpha_p V_\beta \end{bmatrix}$$

Selecting λ_3 to be sufficiently large, the matrix previously mentioned Λ_{total} is positive definite and $(e_n, e_{vn}, \tilde{P}_n)$ converge to $(0, 0, 0)$ exponentially. The states estimation errors will converge to zero exponentially as well. Therefore, the cylinder's tracking errors will converge to zero exponentially.

5.7 Experimental implementation

In this section, the approaches derived previously will be implemented experimentally. We will first look at the spool axial control problem when it does not spin. In this case, no estimator is implemented. Both passive and traditional backstepping controllers are implemented in this case. In the next step, we implement the passive controller when the valve spool is spinning, and then use the VVDP to drive an orifice load.

5.7.1 Axial motion only

Both the basic backstepping controller Eqn. (5.40) and the passive backstepping controller Eqn. (5.37) were experimentally implemented on the linear positioning of the valve spool, while the spool is not spinning. The bulk modulus was estimated using Yu's model [88] assuming a 10% air entrainment. The supply pressure was set at $190Psi$.

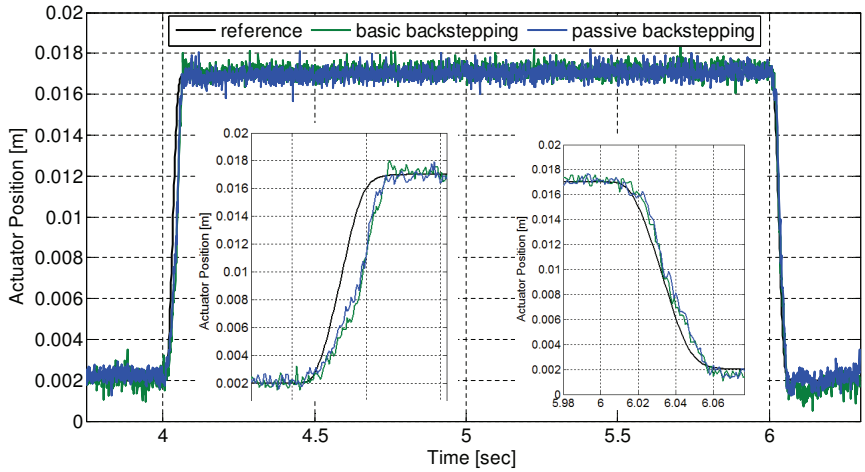

Figure 5.6: Trajectory tracking performances using the two controllers on a filtered trapezoidal trajectory corresponding to a full range duty variation in 50ms

First, the two controllers are compared on tracking a filtered trapezoidal trajectory as shown in Fig. 5.6. Each controller was tuned to the best of our effort. While the best tuned control performances are similar, the basic backstepping controller requires significantly higher gains than the passivity based control as shown in Table 5.1, and it

is more sensitive to measurement noise.

Table 5.1: Feedback gains using two approaches

	λ_p	K_p	K_v	λ_2	λ_3
Basic bkstp	50	550	45	3×10^{-12}	4×10^{-10}
Passivity	50	55	4	n/a	4×10^{-10}

Next, we investigate the benefits of the extra control gain λ_2 available in the basic backstepping controller in Eqn. (5.40) when the velocity measurement is corrupted. To wit, a $1Hz$ first order low pass filter is applied to the velocity measurement and a $5Hz$ sinusoidal trajectory is being tracked. Control gains similar to those in Table 5.1 are applied to both controllers, and a range of λ_2 is applied to the basic backstepping controller.

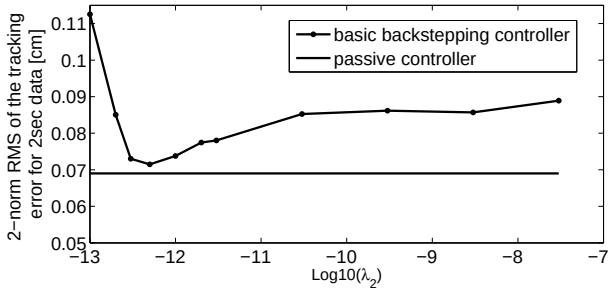

Figure 5.7: Effect of λ_2 on the trajectory tracking performance in the presence of corrupted velocity measurement

Figure 5.7 shows that the tracking error for the basic backstepping controller is minimized when $\lambda_2 \approx 3 \times 10^{-12}$ and is slightly worse than that of the passivity based control. This is expected since in Eqn. (5.40), velocity measurement error would corrupt the first term $\dot{x}$ when λ_2 is too large, and the second term e_v when λ_2 is too small. It is insensitive to the velocity measurement noise as $\lambda_2 \approx \frac{V_0 + Ax}{\beta P}$, because the basic backstepping controller approximates the passivity based controller.

5.7.2 Axial positioning using estimation

The external driving mechanism and the passivity based controller for stabilizing the valve spool axial position are implemented experimentally. The spool is driven to rotate at a constant angular velocity of $22.5Hz$. The spool axial position is measured by a set of optical sensors, and the measurement is corrupted by a periodic noise. The VVDP drives a constant orifice load of $400psi$ in this experiment.

Feeding back the correct spool axial position stabilizes the spool at a fixed axial position as shown in Fig. 5.8. This can be further reflected from the valve pressure profile, as shown in Fig. 5.9. Since the load is an orifice, the valve load pressure varies with the load flow, following the orifice equation. If the valve spool oscillates in the axial direction, the duty ratio and the load flow will vary, and correspondingly the valve load pressure will vary. A stabilized load pressure at $400Psi$ shows that the valve spool axial position is stabilized.

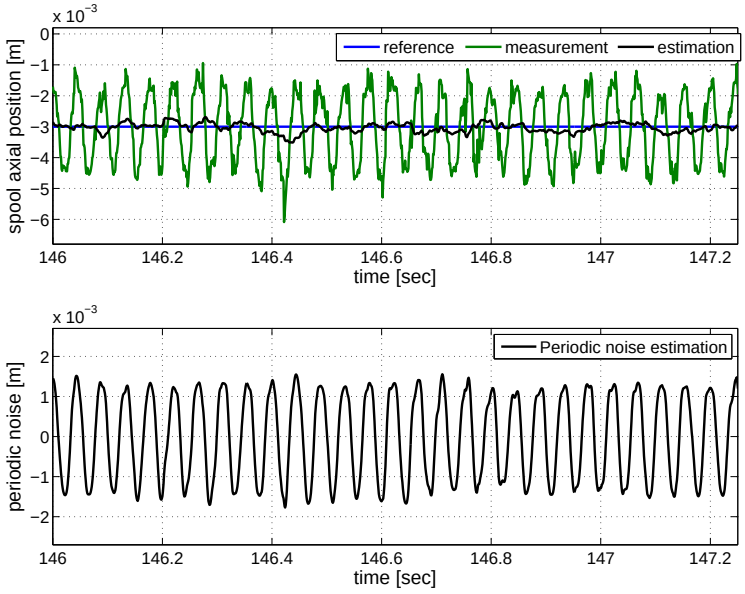

Figure 5.8: Stabilization of spool axial position in the presence of periodic measurement noise

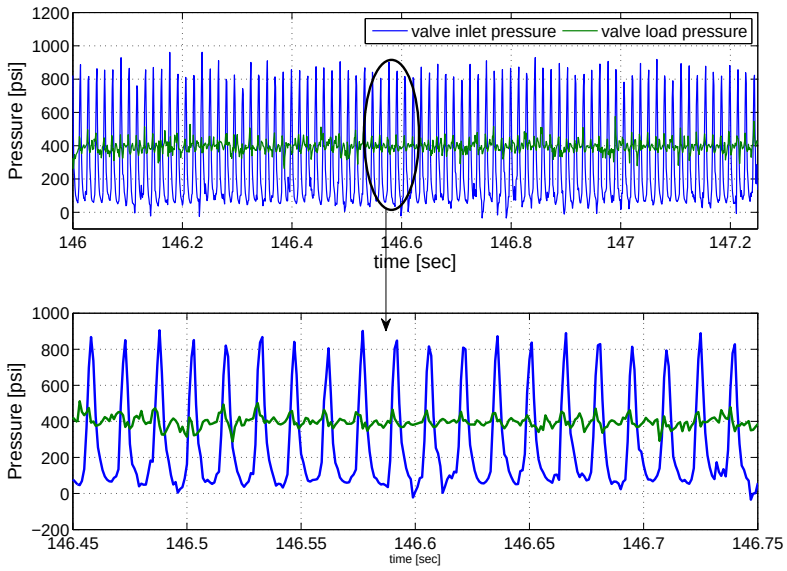

Figure 5.9: Valve inlet and load pressure

5.8 Summary

In this chapter, a different valve spool axial positioning system was proposed. Considering the actuation chamber pressure dynamics, a passivity based nonlinear controller was proposed to achieve the spool trajectory tracking. The controller storage function regarding pressure tracking was obtained from the compressibility energy of the fluid in the actuator. Compared with the traditional basic backstepping controller, the passive one maintains the essential nonlinearities associated with the varying chamber volume and the possibly uncertain bulk modulus for the stabilizing term, thus, resulting in a more robust and better tracking performance controller. This passivity based control strategy can be applied to the positioning of other hydraulic actuators.

Another contribution of this work is the observability investigation of the positioning system augmented with the structured noise. This analysis can be extended to the system with periodic measurement noise. We set up the condition to determine the observability of the augmented system, and built an estimator for the true spool axial position and velocity.

In a linear system where the estimator and the controller can be designed separately, it is safe to feed back the estimation. Both the estimation error and the tracking error can converge to zero. However, this nice property does not apply to nonlinear systems. The effectiveness of implementing the passive controller with estimation is considered via an augmented Lyapunov function. By properly designing the estimator, so that the estimator error converges fast, the trajectory tracking error can converge to zero exponentially.

Chapter 6

Direct displacement control of hydraulic actuators using a multi-mode nonlinear controller

6.1 Introduction

In this chapter, the VVDP will be utilized as a variable flow source in a displacement control circuit to drive the motion of a hydraulic actuator. While the rotary on/off valve concept can be extended to achieve a virtually variable pump/motor (VVDPM)[79][92], here we consider only the VVDP which can only function as a pump. It is because the VVDP cannot go "over-center" to provide negative displacements, like a swash-plate pump. In order to provide the control authority for four quadrant operation of an actuator, a proportional valve and a directional valve are utilized together with the VVDP in the circuit.

The proposed direct displacement control open circuit is shown in Fig. 6.1. The circuit consists of a variable displacement pump, a 4-way directional valve, and a proportional valve. The 4-way directional valve is operated in an open-loop manner, so no valve position feedback is required. This valve is utilized to switch the flow direction, and it remains fully open during operation to reduce throttling loss. In this circuit, no charge pump or accumulator is required on the return line to maintain the return

chamber pressure; instead, a one-way proportional valve is introduced on the return line to provide the back pressure via throttling flow control.

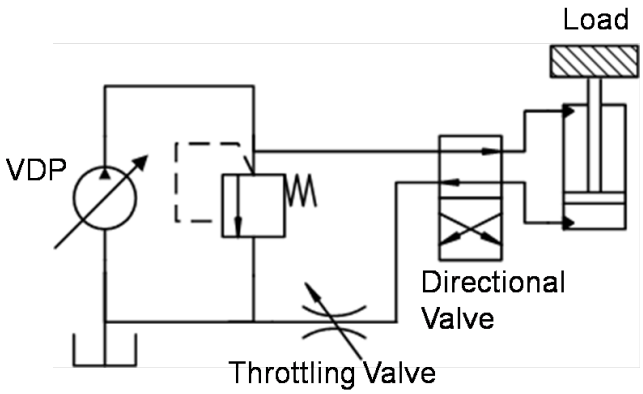

Figure 6.1: Direct displacement control open circuit

Comparing valve control with pump displacement control, throttling valves are typically faster but much less efficient, while variable displacement pumps are slower but more efficient. In our circuit, a key feature is that control effort is distributed optimally between the VVDP and the throttling valve. This enables the circuit to provide both good control performance and low throttling loss operations. To reduce the throttling loss, the ideal operation of the throttling valve's is to have a large mean opening area superimposed by a small varying area to provide high control bandwidth. The VVDP provides the rest of the control effort, and its temporal flow trajectory should be of low frequency. In order to achieve a balanced control distribution between the VVDP and the valve, a novel model is proposed to account for the control effort's dynamics, so that a routine estimation approach can be applied to determine the optimal control efforts of the VVDP and the throttling valve in real time. This novel model approximates the dynamics of the VVDP as a first order system with process noise to accommodate its slow dynamics. The combined control effort is treated as a "measurement" signal with a measurement noise, and the measurement noise accounts for the control effort provided from the proportional valve. With this novel first order model, a typical deterministic Kalman filter can be constructed to estimate the state - "pump control effort" from the noisy measurement "total control effort" in real time.

Since the VVDP and the throttling valve can be operated independently, in addition

to achieving accurate actuator position tracking, this hydraulic circuit can also prevent cavitation and over pressure in the actuator chambers. Depending on the chambers' pressure, different control modes are defined, and the control objectives of the VVDP and the throttling valve vary accordingly.

For the rest of this chapter, both the actuator's dynamics and the pressure dynamics when the directional valve is commanded to different positions will be presented in section 6.2. In section 6.3, a passivity based nonlinear controller will be developed to define the total control effort, which is targeted at driving the hydraulic actuator to accurately track a pre-defined trajectory. The novel model to capture the control efforts' bandwidth, and the estimator to determine the distribution of the control effort between the VVDP and the throttling valve will be discussed in section 6.4. Experimental validation of the proposed hydraulic circuit and the control approach will be presented in section 6.5. Finally, some concluding remarks and the future work will be covered in section 6.6.

6.2 System dynamics

For modeling purposes in this work, the inertial dynamics of the actuator, and the pressure dynamics inside the actuator chambers are considered. The dynamics of the proportional throttling valve are ignored, and the high frequency dynamics of the directional valve is accounted for in the process noise.

The hydraulic actuator and the load are modeled as a mass acted upon by the pressure forces from the two actuator chambers, the linear viscous friction force, and the load force:

$$m\ddot{x} = P_1 A_1 - P_2 A_2 - b\dot{x} + F_L + d \tag{6.1}$$

where m is the mass of the cylinder rod, and x is the position of the cylinder rod and the load inertia. A_1 and A_2 are the areas of the cylinder cap end and the rod end, b is the viscous friction coefficient, F_L is the carrying load force, and d represents the unknown disturbance force.

As shown in Fig. 6.2, the circuit has two configurations, depending on the operation of the directional valve. The VVDP either provides flow into the head chamber of the cylinder or in the rod chamber. Q denotes the flow rate entering the meter-in chamber.

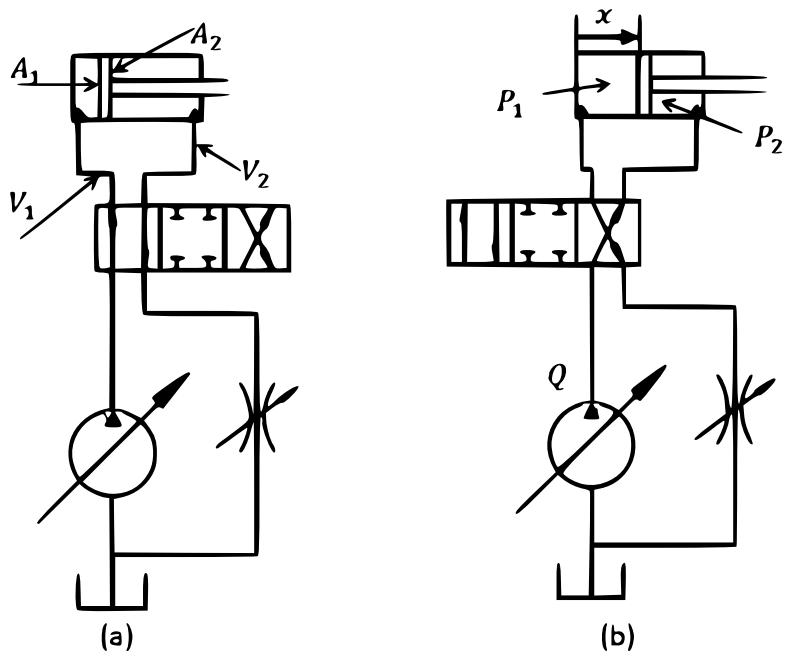

Figure 6.2: Hydraulic configurations for different directional valve operations: (a) is the circuit when the head side of the actuator is connected to the VVDP; (b) is the circuit when the rod side of the actuator is connected to the VVDP.

V_1 denotes the dead volume inside the cylinder on the head chamber when the actuator position is $x = 0$ and the volume inside the hose between the VVDP and the head chamber. V_2 denotes the dead volume on the rod side and the hose volume between the rod chamber and the the throttling valve when the actuator stays at the same position $x = 0$. The throttling valve on the return line is modeled as an orifice. The orifice coefficient is defined as $K_v = C_d A_{max}\sqrt{\frac{2}{\rho}}$, with A_{max} being the maximum valve opening area, and $u \in [0, 1]$ being the normalized throttling valve command. ρ is the fluid density, and $C_d = 0.6$ is the coefficient of discharge. The two positions of the directional valve are denoted by $u_d = \{-1, 1\}$, and the respective circuits are shown in Fig. 6.2(a) and Fig. 6.2(b). The flow crossing the throttling valve follows an orifice equation:

$$\begin{aligned}
&\text{when } u_d = 1 \text{ (Fig. 6.2(a)):} \\
&\quad Q_{valve} = uK_v\sqrt{(|P_2 - P_t|)}sign(P_2 - P_t) \\
&\text{when } u_d = -1 \text{ (Fig. 6.2(b)):} \\
&\quad Q_{valve} = uK_v\sqrt{(|P_1 - P_t|)}sign(P_1 - P_t)
\end{aligned} \tag{6.2}$$

With P_t denoting the tank pressure, the chamber pressure dynamics are modeled as:

$$\text{when} \quad u_d = 1 \text{ (Fig. 6.2(a)):}$$

$$\dot{P}_1 = \frac{\beta}{V_1 + A_1 x}(Q - A_1\dot{x}) \tag{6.3a}$$

$$\dot{P}_2 = \frac{\beta}{V_2 - A_2 x}(A_2\dot{x} - uK_v\sqrt{|P_2 - P_t|}sign(P_2 - P_t)) \tag{6.3b}$$

$$\text{when} \quad u_d = -1 \text{ (Fig. 6.2(b)):}$$

$$\dot{P}_1 = \frac{\beta}{V_1 + A_1 x}(-A_1\dot{x} - uK_v\sqrt{|P_1 - P_t|}sign(P_1 - P_t)) \tag{6.3c}$$

$$\dot{P}_2 = \frac{\beta}{V_2 - A_2 x}(A_2\dot{x} + Q) \tag{6.3d}$$

In this modeling, the fluid bulk modulus β is assumed to be constant. The control inputs include the directional valve input $u_d \in [-1, 1]$, which is a discrete binary when being powered, the proportional valve input u, which has a fast control bandwidth, and the variable flow Q, which has a slow control bandwidth.

6.3 Passivity based controller

The motion control objective is for the actuator's position $x(t)$ to track a reference trajectory $x_d(t)$. Introducing one variable as $F_H = P_1A_1 - P_2A_2$ to model the hydraulic force acting on the actuator, the cylinder dynamics become:

$$\begin{aligned} m\ddot{x} =& F_H - b\dot{x} + F_L + d \\ \dot{F}_H =& U_{total} - \beta \underbrace{\left(\frac{A_1^2}{V_1 + A_1 x} + \frac{A_2^2}{V_2 - A_2 x} \right)}_{L(x)} \dot{x} \end{aligned} \tag{6.4}$$

with $U_{total} = H(x, u_d) \cdot Q + G(x, u_d)\Psi(P_1, P_2, u_d) \cdot u$

$$\begin{aligned} H(x, u_d) &= \begin{cases} \frac{\beta A_1}{V_1 + A_1 x} & u_d = 1 \\ \frac{-\beta A_2}{V_2 - A_2 x} & u_d = -1 \end{cases} \\ G(x, u_d) &= \begin{cases} \frac{\beta A_2}{V_2 - A_2 x} & u_d = 1 \\ \frac{-\beta A_1}{V_1 + A_1 x} & u_d = -1 \end{cases} \\ \Psi(P_1, P_2, u_d) &= \begin{cases} K_v \sqrt{|P_2 - P_t|} sign(P_2 - P_t) & u_d = 1 \\ K_v \sqrt{|P_1 - P_t|} sign(P_1 - P_t) & u_d = -1 \end{cases} \end{aligned} \tag{6.5}$$

This section focuses on designing a U_{total} (Eqn. (6.4)) to achieve cylinder trajectory tracking. First, a desired compensation control law (DCCL) [89] is developed for cylinder trajectory tracking from the mechanical side in sec 6.3.1. Secondly, an $h(\cdot)$ function is proposed to support the design of a pressure (hydraulic force) tracking error based compressible energy storage function in sec 6.3.2 to account for the pressure tracking error. Finally, both effects are considered together to develop U_{total} in sec 6.3.3.

6.3.1 Trajectory tracking using a DCCL controller

Assuming $x_d(t)$, $\dot{x}_d(t)$, $\ddot{x}_d(t)$, and $\dddot{x}_d(t)$ are available and smooth, then following the typical mechanical robot motion controller design procedure, a DCCL controller was developed to accomplish cylinder position tracking. Let $e = x - x_d$, and define the following reference velocity r, and the reference velocity error e_v:

$$r = \dot{x}_d - \lambda e; \quad e_v = \dot{x} - r = \dot{e} + \lambda e \tag{6.6}$$

with $\lambda > 0$, the dynamics of e_v become:

$$m\dot{e}_v = -m(\ddot{x}_d - \lambda\dot{e}) - b(\dot{e} + \dot{x}_d) + F_H + F_L + d \tag{6.7}$$

The Lyapunov function considering the position and velocity tracking errors is defined as:

$$W_{mech} = \frac{1}{2}me_v^2 + \frac{1}{2}K_p e^2 \tag{6.8}$$

An ideal hydraulic force F_v is proposed as:

$$F_v = m(\ddot{x}_d - \lambda\dot{e}) + b(\dot{e} + \dot{x}_d) - F_L - K_v e_v - K_p e \tag{6.9}$$

With this hydraulic force, the time derivative of W_{mech} becomes:

$$\dot{W}_{mech} = -K_v e_v^2 - \lambda K_p e^2 - e_v d + e_v \tilde{F} \tag{6.10}$$

where $\tilde{F} = F_H - F_v$. K_v and K_p are positive constants.

6.3.2 Pressure error storage function

The Lyapunov function defined in Eqn. (6.8) needs to be augmented with the pressure error (or hydraulic force error). This will be used for controlling the pressure and the actuator velocity according to some desired reference trajectories. For a single ended double acting hydraulic actuator, a storage function is proposed in terms of pressure error (or hydraulic force error) instead of for the individual pressures. The storage function is formulated via a proposed monotonic function $h(\cdot) : \mathbb{R} \mapsto \mathbb{R}$[93][57][58][1] .

$$h(\sigma) := A_1 \ln(V_1 + A_1\sigma) + A_2 \ln(V_2 - A_2\sigma) \tag{6.11}$$

Let $F_H = A_1P_1 - A_2P_2$, x be the current actuator force and position, and F_v be the desired actuator force. Define x_{fd} and $\bar{x}$ from:

$$h(x) = h(\bar{x}) - \frac{F_H}{\beta}, \quad h(x_{fd}) = h(\bar{x}) - \frac{F_v}{\beta} \tag{6.12}$$

[1] The logic of defining $h(\cdot)$ is based on the course notes from a course at the University of Minnesota ME8287[94]. Topics in Control: Passivity and Control of Interactive Mechanical and Fluid Powered Systems

Consider the pressure error storage function:

$$W_F = \beta \int_{x_{fd}}^{x} \left[h(\sigma) - h(x_{fd})\right] d\sigma \tag{6.13}$$

which is derived considering the fluid compressible energy in both chambers. Recall the definitions in Eqn. (6.7) and Eqn. (6.9), $\dot{W}_F$ becomes

$$\begin{aligned}\frac{d}{dt}W_F =& \beta \left[h(x) - h(x_{fd})\right] \dot{x} - \beta \int_{x_{fd}}^{x} \dot{h}(x_{fd}) d\sigma \\ =& - \tilde{F}\dot{x} - \left(U_{total} - \dot{F}_v\right)(x - x_{fd})\end{aligned} \tag{6.14}$$

Notice that $h(\cdot)$ is continuous and monotonic, from the mean value theorem:

$$h(x) - h(x_{fd}) = L(\alpha)(x - x_{fd}), \text{for} \quad \alpha \in (x_{fd}, x) \tag{6.15}$$

where $L(\cdot)$ is defined in Eqn. (6.4). Substituting this relationship into Eqn. (6.14), $\dot{W}_F$ is manipulated into:

$$\dot{W}_F = -\tilde{F}\dot{x} + \frac{\tilde{F}}{\beta L(\alpha)}\left(U_{total} - \dot{F}_v\right) \tag{6.16}$$

6.3.3 Passive control law

Now augment W_{mech} defined in Eqn. (6.8) with W_F defined in Eqn. (6.13) to define the total energy storage function:

$$W_{total} = \frac{1}{2}me_v^2 + \frac{1}{2}K_p e^2 + \beta \int_{x_{fd}}^{x} \left[h(\sigma) - h(x_{fd})\right] d\sigma \tag{6.17}$$

The time derivative $\dot{W}_{total}$ becomes:

$$\dot{W}_{total} = -K_v e_v^2 - \lambda K_p e^2 - e_v d - r\tilde{F} + \frac{\tilde{F}}{\beta L(\alpha)}\left(U_{total} - \dot{F}_v\right) \tag{6.18}$$

Propose a control law U^*_{total} as:

$$U^*_{total} = \beta L(x) r + \dot{F}_v - \lambda_3 \beta \tilde{F} + u_{rob}\beta \tag{6.19}$$

$\dot{W}_{total}$ becomes:

$$\dot{W}_{total} = -K_v e_v^2 - \lambda K_p e^2 - e_v d - \frac{\lambda_3}{L(\alpha)}\tilde{F}^2 + \frac{\tilde{F}(\tilde{L}r + u_{rob})}{L(\alpha)} \tag{6.20}$$

where $\tilde{L} = L(x) - L(\alpha)$. Analysis in Ref [95] has shown that $\tilde{L}$ is bounded by $\tilde{F}$ as: $|\tilde{L}| \leq \gamma_F |\tilde{F}|$, for some finite positive γ_F. Therefore, by selecting $u_{rob} = -K_{rob}\beta\tilde{F}$, with a large feedback gain $K_{rob} > \gamma_F$, $\dot{W}_{total}$ becomes:

$$\dot{W}_{total} \leq -K_v e_v^2 - \lambda K_p e^2 - e_v d - \lambda_n \tilde{F}^2$$
$$\text{with} \quad \lambda_n = \frac{\lambda_3}{L(\alpha)} + (K_{rob} - \gamma_F) > 0 \tag{6.21}$$

The Lyapunov function W_{total} is positive definite in e, e_v, and $\tilde{P}$. When $d = 0$, the time derivative of the Lyapunov function $\dot{W}_{total}$ is negative definite in e, e_v, and $\tilde{P}$. Therefore, the tracking errors e, e_v, and $\tilde{P}$ will converge to zero exponentially. When d is bounded, by selecting K_v to be large enough, all the tracking errors can converge to an arbitrarily small value, as long as the control efforts do not saturate [95].

6.4 Control effort distribution

The previous section has defined the desired total control effort U^*_{total} in Eqn. (6.19). This section will discuss how to distribute the three control inputs Q, u, and u_d to achieve several objectives:

1. The trajectory tracking performance is guaranteed:

$$U^*_{total}(t) := H(x, u_d) \cdot Q + G(x, u_d)\Psi(P_1, P_2, u_d) \cdot u \tag{6.22}$$

2. The pressure in both actuator chambers stays bounded, with the upper bound denoted by $\overline{P}_i$, the lower bound denoted by $\underline{P}_i$, and the tank pressure denoted by P_t:

$$\overline{P}_i \geq P_i(t) \geq \underline{P}_i > P_t, \ i \in 1, 2 \tag{6.23}$$

3. The usage of the the proportional valve u is minimized to reduce the throttling loss.

4. In Eqn. (6.22), the control effort U^*_{total} is achieved in the following manner: $G(x, u_d)\Psi(P_1, P_2, u_d) \cdot u$ is used to track the high frequency component of $U^*_{total}(t)$, and $H(x, u_d) \cdot Q$ is used to track the low frequency component of U^*_{total}.

Recalling the pressure dynamics defined in Eqn. 6.3a-6.3d, these can be re-written as:

$$\begin{aligned}
\text{when } u_d &= 1: \\
\dot{P}_1 &= \frac{\beta}{V_1 + A_1 x}(Q - A_1\dot{x}) && (6.24a)\\
\dot{P}_2 &= \frac{\beta}{V_2 - A_2 x}(A_2\dot{x} - \Psi(P_1, P_2, u_d)u) && (6.24b)\\
\text{when } u_d &= -1: \\
\dot{P}_1 &= \frac{\beta}{V_1 + A_1 x}(-A_1\dot{x} - \Psi(P_1, P_2, u_d)u) && (6.24c)\\
\dot{P}_2 &= \frac{\beta}{V_2 - A_2 x}(A_2\dot{x} + Q) && (6.24d)
\end{aligned}$$

6.4.1 Directional valve

As defined in Eqn. (6.5), the signs of $H(x, u_d)$ and $G(x, u_d)$ are consistent with the sign of u_d. If the pressures in both chambers stay above atmospheric pressure, $\Psi(P_1, P_2, u_d)$ is positive. Therefore, u_d is determined by the sign of U^*_{total}:

$$u_d(t) = \begin{cases} 1 & \text{when} \quad U^*_{total} \geq 0 \\ -1 & \text{when} \quad U^*_{total} < 0 \end{cases} \tag{6.25}$$

6.4.2 Flow Q vs. throttling valve u

To distribute the total control efforts between Q and u after determining the directional valve position, two factors are considered. First, to minimize the throttling loss, the usage of the proportional valve u should be minimized. In other words, it is preferred to make u as close to 1 as possible. Second, Q and u have different control bandwidths, and it is desired to track the high frequency component of $U^*_{total}(t)$ using u, and to track the low frequency component of U^*_{total} using Q. To achieve this control effort distribution, the following method is proposed.

Assume the dynamics of the desired pump flow Q_{des} follows:

$$\begin{aligned}
\dot{Q}_{des} &= -\lambda_Q Q_{des} + \lambda_Q(w + \bar{Q}_{des}) \\
U^*_{total} &= H \cdot Q_{des} + G\Psi \cdot \bar{u}_{des} + G\Psi \cdot \tilde{u}_{des}
\end{aligned} \tag{6.26}$$

where $\bar{Q}_{des}$ and $\bar{u}_{est}$ are some pre-defined nominal values of Q_{des} and u_{des}. Here, it is desired to make $\bar{u}_{des}$ as close to 1 as possible, but $\bar{u}$ is constrained by the variation of $\tilde{u}_{des}$, because $0 \leq u_{des} = \hat{u}_{des} + \tilde{u}_{des} \leq 1$. A similar argument can be applied to Q_{des}. Since the flow from the variable displacement pump is always greater than 0, a positive nominal flow $\bar{Q}_{des}$ is introduced to account for this effect so that the process noise w of the desired pump flow dynamics can be modeled as zero-mean white noise. λ_Q is the time constant of the desired pump flow dynamics, which quantifies the control bandwidth of the desired pump flow.

The second equation in Eqn. (6.26) is manipulated into:

$$\underbrace{\frac{U^*_{total} - G\Psi\bar{u}_{des}}{G\Psi}}_{\nu} = \frac{H}{G\Psi}Q_{des} + \tilde{u}_{des} \tag{6.27}$$

where ν plays the role of a measurement, and $\tilde{u}_{des}$ plays the role of a measurement noise. Here $\tilde{u}_{des}$ is modeled as zero-mean white noise.

Next, Q_{est} is estimated by considering the pump flow dynamics in Eqn. (6.26) and the "measurement" ν, while minimizing the variation of w and $\tilde{u}_{des}$. The variance of the process noise w is denoted by Q_J, and the variance of the measurement noise $\tilde{u}_{des}$ is denoted by R_J. We define the estimator as:

$$\dot{\hat{Q}}_{des} = -\lambda_Q\hat{Q}_{des} + L_{est}\left(\nu - \frac{H}{G\Psi}\hat{Q}_{est}\right) \tag{6.28}$$

where L_{est} is the estimator gain which is computed by minimizing the following objective function:

$$J = \frac{1}{2}\int_{t_0}^{t_f}(wQ_J^{-1}w + \tilde{u}_{des}R_J^{-1}\tilde{u}_{des})\ d\tau \tag{6.29}$$

This objective function is considered with respect to the plant dynamics and output equation defined in Eqn. (6.26) and Eqn. (6.27):

$$\begin{aligned}\dot{Q}_{des} &= -\lambda_Q Q_{des} + \lambda_Q(w + \bar{Q}_{des}) \\ \nu &= \frac{H}{G\Psi}Q_{des} + \tilde{u}_{des}\end{aligned} \tag{6.30}$$

With this objective function, the design of the estimator feedback gain L_{est} follows the

design of a typical deterministic Kalman filter[62]:

$$\begin{aligned} \dot{P}_e &= -2\lambda_Q P_e + \lambda_Q^2 q_J - \frac{1}{R_J}\left(\frac{H}{G\Psi}\right)^2 P_e^2 \\ L_{est} &= \frac{P_e(t)H}{G\Psi R_J} \end{aligned} \tag{6.31}$$

$\hat{Q}_{est}(t)$ is the desired flow we would like the variable displacement pump output flow Q to track. To re-produce U^*_{total}, the desired proportional valve opening fraction is:

$$\begin{aligned} u_{des} &= \bar{u}_{des} + \tilde{u}_{des} \\ &= \frac{U^*_{total} - H \cdot \hat{Q}_{est}}{G\Psi} \end{aligned} \tag{6.32}$$

Note that the pump flow $\hat{Q}_{est}$ in Eqn. (6.28) and the throttling valve opening u_{des} in Eqn. (6.32) are feasible only when the pressure in both chambers stay bounded. If the pressure is higher (or lower) than the pressure bound defined in Eqn. (6.23), $\hat{Q}_{est}$ and u_{des} needs to be adjusted to account for the pressure compensation. Now the different operational modes can be defined to deal with different pressure conditions.

The chamber that is connected to the variable displacement pump is denoted as the supply chamber and the chamber that is connected to the proportional valve is denoted as the return chamber. Depending on the chamber pressure conditions, the corresponding operation modes can be defined as shown in Fig. 6.3. Besides position tracking, the control logic can also prevent chamber pressure cavitation and the chamber pressure being too high. Notice that the case where pressures in both chambers are lower than the lower threshold or higher than the upper threshold is not feasible if the system operates normally, so it will not be included in the modes.

Mode 1: both chamber pressures stay bounded.

This mode applies to the cases when no pressure constraint is active. U^*_{total} is reproduced from Eqn. (6.28) and Eqn. (6.32):

$$\begin{aligned} Q &= \hat{Q}_{des} \\ u &= u_{des} \end{aligned} \tag{6.33}$$

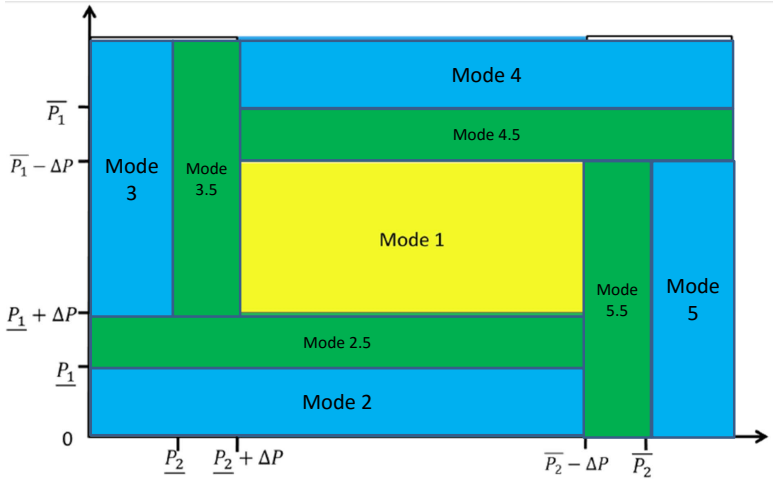

Figure 6.3: Control modes defined when P_1 refers to the supply chamber pressure and P_2 refers to the return chamber pressure

Mode 2: the supply chamber pressure is lower than $\underline{P}_i$.

In this mode, the pressure in the supply chamber is low, and has the potential to cavitate. From Eqn. (6.24a) and Eqn. (6.24c), the variable flow source Q will be used to increase the pressure. From the definition of U^*_{total}, setting $Q > A_1\dot{x}$ when $U^*_{total} > 0$, or setting $Q < -A_2\dot{x}$ when $U^*_{total} < 0$ will increase the meter-in chamber pressure. After determining the control effort of Q, based on Eqn. (6.22), the throttling valve u will be used for trajectory tracking. The control laws are:

$$
\begin{aligned}
Q &= \begin{cases} A_1\dot{x} + \xi_Q|A_1\dot{x}|, & \text{If } U^*_{total} > 0 \\ -A_2\dot{x} + \xi_Q|A_2\dot{x}|, & \text{If } U^*_{total} < 0 \end{cases} \\
u &= \frac{U^*_{total} - H(x,u_d)Q}{G(x,u_d)\Psi(P_1,P_2,u_d)}
\end{aligned}
\tag{6.34}
$$

with $\xi_Q > 0$. Notice that this imposes a lower bound on Q (or an upper bound on u). If the upper bound on u is greater than 1, we can set $u = 1$, and recalculate Q.

Mode 2.5: the supply chamber pressure is between $\underline{P}_i$ and $\underline{P}_i + \Delta P_i$.

This mode provides a smooth transition between Mode 1 and Mode 2. The flow command is a weighted sum of the flow command from mode 1 and the flow command from

mode 2. The weight is determined by the chamber pressure.

$$\begin{aligned}
\gamma &= \begin{cases} \frac{P_1(t)-\underline{P}_1}{\Delta P_1}, & \text{If } U^*_{total} > 0 \\ \frac{P_2(t)-\underline{P}_2}{\Delta P_2}, & \text{If } U^*_{total} < 0 \end{cases} \\
Q &= \gamma Q_1 + (1-\gamma) Q_2 \\
u &= \frac{U^*_{total} - H(x,u_d)Q}{G(x,u_d)\Psi(P_1,P_2,u_d)}
\end{aligned} \tag{6.35}$$

with Q_1 calculated from Eqn. (6.33), and Q_2 calculated from Eqn. (6.34).

Mode 3: the return chamber pressure is lower than $\underline{P}_i$.

In this mode the pressure in the return chamber is low. To prevent cavitation from this chamber, considering the pressure dynamics in Eqn. (6.24b) and Eqn. (6.24d), the throttling valve will be used to increase the chamber pressure when it reaches the threshold.

$$\begin{aligned}
u &= \begin{cases} \frac{A_2\dot{x}-\xi_u|A_2\dot{x}|}{\Psi(P_1,P_2,u_d)}, & \text{If } U^*_{total} > 0 \\ \frac{-A_1\dot{x}-\xi_u|A_1\dot{x}|}{\Psi(P_1,P_2,u_d)}, & \text{If } U^*_{total} < 0 \end{cases} \\
Q &= \frac{U^*_{total} - G(x,u_d)\Psi(P_1,P_2,u_d)u}{H(x_p,u_d)}
\end{aligned} \tag{6.36}$$

with $\xi_u > 0$. Similar to Mode 2, this control law imposes a lower bound on Q. If the bound is greater than Q_{max}, we can set $Q = Q_{max}$, and recalculate u.

Mode 3.5: the return chamber pressure is between $\underline{P}_i$ and $\underline{P}_i + \Delta P_i$.

This mode provides a smooth transition on the control effort between mode 1 and mode 3, and the control laws are defined as:

$$\begin{aligned}
\gamma &= \begin{cases} \frac{P_2(t)-\underline{P}_2}{\Delta P_2}, & \text{If } U^*_{total} > 0 \\ \frac{P_1(t)-\underline{P}_1}{\Delta P_1}, & \text{If } U^*_{total} < 0 \end{cases} \\
u &= \gamma u_1 + (1-\gamma) u_2 \\
Q &= \frac{U^*_{total} - G(x,u_d)\Psi(P_1,P_2,u_d)u}{H(x,u_d)}
\end{aligned} \tag{6.37}$$

with u_1 calculated from Eqn. (6.33), and u_2 calculated from Eqn. (6.34).

Mode 4: the supply chamber pressure is higher than $\overline{P}_i$

In this case, the pump would reduce the supply chamber pressure, and the control laws are:

$$\begin{aligned} Q &= \begin{cases} A_1\dot{x} - \zeta_Q|A_1\dot{x}|, & \text{If } U^*_{total} > 0 \\ -A_2\dot{x} - \zeta_Q|A_2\dot{x}|, & \text{If } U^*_{total} < 0 \end{cases} \\ u &= \frac{U^*_{total} - H(x,u_d)Q}{G(x,u_d)\Psi(P_1,P_2,u_d)} \end{aligned} \tag{6.38}$$

with $\zeta > 0$. This imposes an upper bound on Q. If the upper bound on Q is greater than the maximum flow that the variable flow pump can provide, we will set $Q = Q_{max}$, and recalculate u.

Mode 4.5: the supply chamber pressure is between $\overline{P}_i$ and $\overline{P}_i - \Delta P_i$.

A transition mode is defined between mode 1 and mode 4 to smooth the transition.

$$\begin{aligned} \gamma &= \begin{cases} \frac{\overline{P}_1 - P_1(t))}{\Delta P_1}, & \text{If } U^*_{total} > 0 \\ \frac{\overline{P}_2 - P_2(t)}{\Delta P_2}, & \text{If } U^*_{total} < 0 \end{cases} \\ Q &= \gamma Q_1 + (1-\gamma)Q_2 \\ u &= \frac{U^*_{total} - H(x,u_d)Q}{G(x,u_d)\Psi(P_1,P_2,u_d)} \end{aligned} \tag{6.39}$$

with Q_1 calculated from Eqn. (6.33), and Q_2 calculated from Eqn. (6.38).

Mode 5: the return chamber pressure is higher than $\overline{P}_i$.

In this mode the pressure in the return chamber is high, and the throttling valve is used to reduce the chamber pressure.

$$\begin{aligned} u &= \begin{cases} \frac{A_2\dot{x} + \zeta_u|A_2\dot{x}|}{\Psi(P_1,P_2,u_d)}, & \text{If } U^*_{total} > 0 \\ \frac{-A_1\dot{x} + \zeta_u|A_1\dot{x}|}{\Psi(P_1,P_2,u_d)}, & \text{If } U^*_{total} < 0 \end{cases} \\ Q &= \frac{U^*_{total} - G(x,u_d)\Psi(P_1,P_2,u_d)u}{H(x,u_d)} \end{aligned} \tag{6.40}$$

with $\zeta_u > 1$. This control law imposes an upper bound on u. If the bound is greater than 1, $u = 1$ is implemented.

Mode 5.5: the return chamber pressure is between $\overline{P}_i$ and $\overline{P}_i - \Delta P_i$.

This mode provides a smooth transition on the control effort between mode 1 and mode 5, and the control laws are defined as:

$$\begin{aligned}
\gamma &= \begin{cases} \frac{\overline{P}_2 - P_2(t)}{\Delta P_2}, & \text{If } U^*_{total} > 0 \\ \frac{\overline{P}_1 - P_1(t)}{\Delta P_1}, & \text{If } U^*_{total} < 0 \end{cases} \\
u &= \gamma u_1 + (1-\gamma) u_2 \\
Q &= \frac{U^*_{total} - G(x, u_d)\Psi(P_1, P_2, u_d)u}{H(x, u_d)}
\end{aligned} \tag{6.41}$$

with u_1 calculated from Eqn. (6.33), and u_2 calculated from Eqn. (6.40).

Continuity

In order to achieve trajectory tracking, and to regulate both chamber pressures operating in the normal range without being too high or cavitating, only five control modes are required (Mode 1,2,3,4,5). However, the control efforts Q and u defined in these five modes are not continuous. This may cause chattering on the mode selection when the pressures are near the bounds. The valves or the variable flow source needs to switch between states fast, which makes the control strategy infeasible to implement in practice. To overcome the discontinuity, four more modes were introduced: Mode 2.5, 3.5, 4.5 and 5.5. These modes provide transition margins, and the pressure weighted control laws provide a smooth transition between mode 1 and the other four modes.

6.5 Experimental results

In the experimental set up, instead of implementing a variable displacement pump, the virtually variable displacement pump (VVDP) accomplished using the rotary valve was used as the variable flow source[3]. To briefly recap the operational principle of the VVDP, figure 6.4 shows the hydraulic configuration of the VVDP. A constant flow source (a fixed displacement pump) is pulse width modulated (PWMed) by a high speed on/off valve, and the average flow feeding to load is smoothed out by an accumulator (or the hoses and the connectors). By controlling the PWM duty ratio, the mean flow going to the load branch can be adjusted. Since the on/off valve has low loss in either

on or off states, this approach potentially can reduce throttling loss and increase the system efficiency.

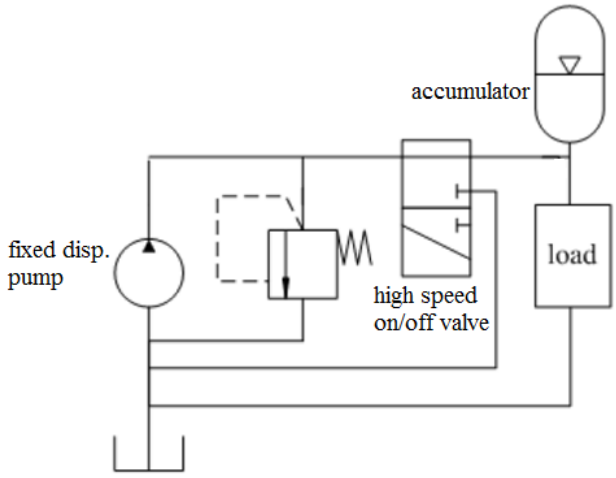

Figure 6.4: Software enabled VVDP circuit

The load being driven is a hydraulic cylinder. The cylinder has a cap area of $20.26cm^2$ and a rod area of $10.77cm^2$. The control objective is to regulate the cylinder position to track a pre-defined trajectory. The reference trajectory is a triangle wave, which corresponds to a stroke traveling of $21.6cm$ within $4sec$.

The cylinder position tracking results are shown in Fig. 6.5 and Fig. 6.6. With the proposed nonlinear controller, the actuator can achieve a good trajectory tracking, with a tracking error less than $0.5cm$. Both chamber pressures stay within bounds, and the controller operates in mode 1, without activating any of the pressure regulation modes.

Next, the control efforts are investigated to achieve the above cylinder motion regulation results. The directional valve command, the proportional valve command, and the supply flow command are shown in Fig. 6.7. The directional valve has a clear switching instead of chattering in between the two positions. The proportional valve input has a high bandwidth, and the pump flow command has a low bandwidth. In this experiment, the Kalman filter presented in sec 6.4.2 produces a "smooth" flow command with low frequency component, and the high frequency component of U^*_{total} is realized via the proportional valve. $\bar{u}_{des}$ is set to be 0.8, which means the nominal opening of

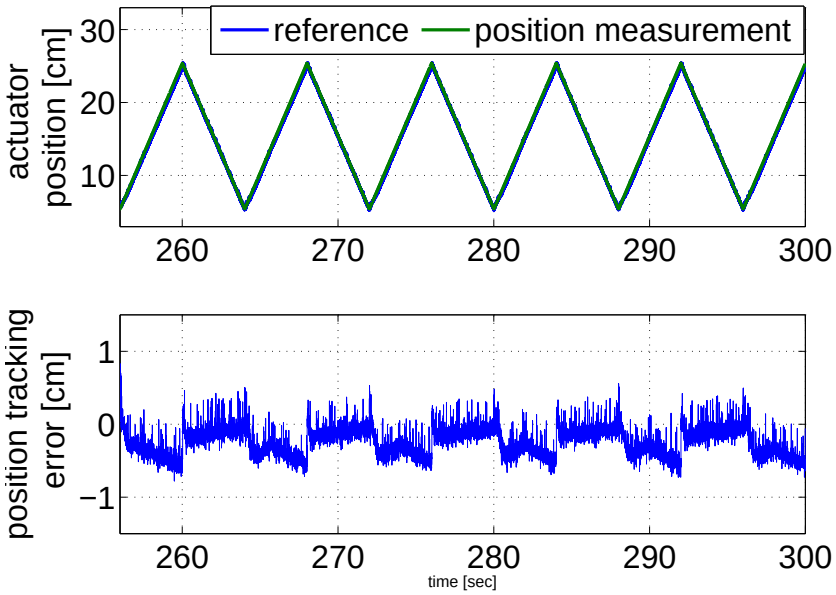

Figure 6.5: Actuator position reference and the tracking error

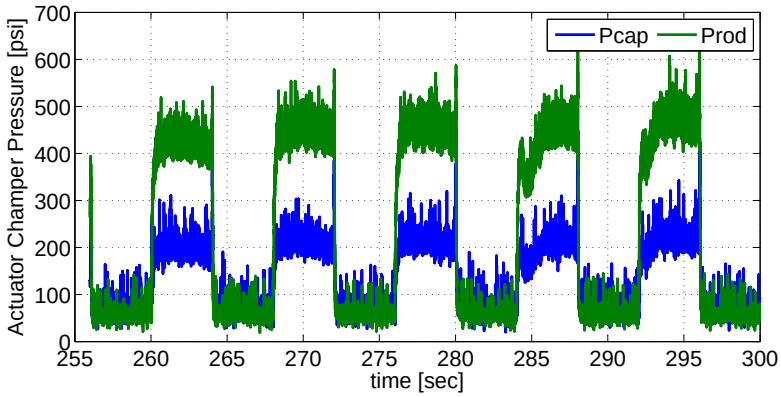

Figure 6.6: Chamber Pressures

the proportional valve is 80%. This threshold is established based on a trial and error exercise to meet the requirements that Q and u are not saturated. Except for the saturation constraints, the proportional valve is controlled to be open as much as possible. The distribution of U^*_{total} between Q and u is shown in in Fig. 6.8. Since the VVDP cannot function as a hydraulic motor, no negative flow can be provided, and therefore the lowest bound of Q is $0lpm$. When $Q = 0lpm$, all the control action is accomplished via the throttling valve.

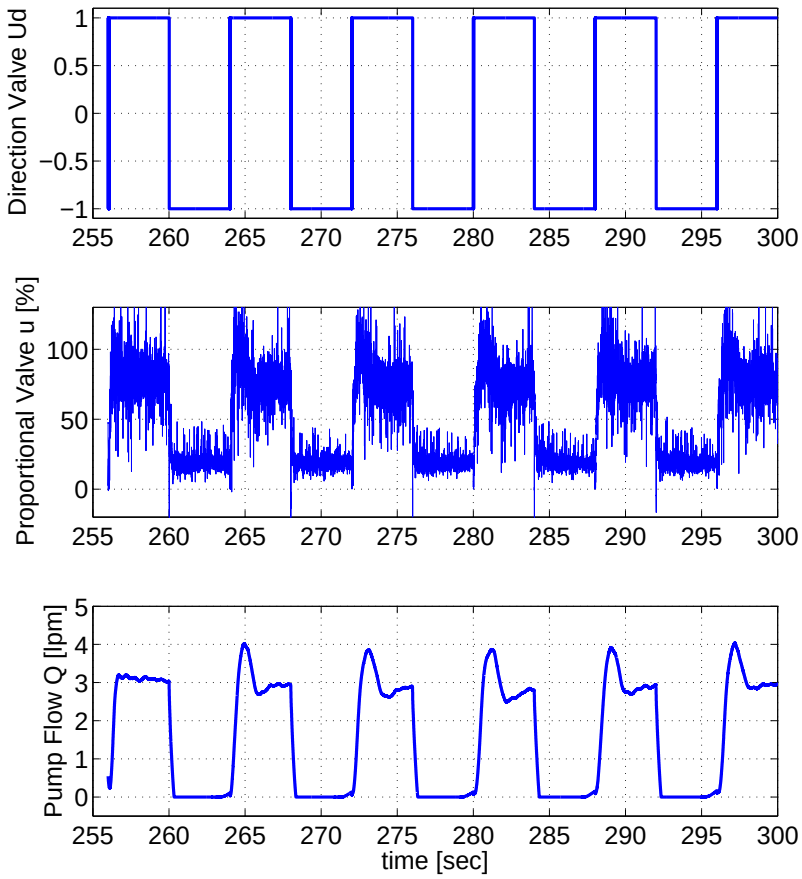

Figure 6.7: Control efforts of the directional valve, the throttling valve, and the VVDP

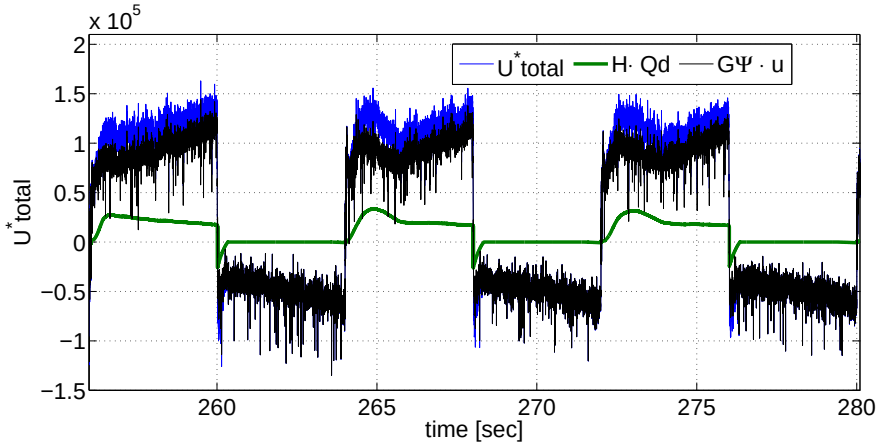

Figure 6.8: U^*_{total} distribution

6.6 Summary

In this chapter, the VVDP accomplished using the rotary valve is utilized in a direct displacement control circuit to drive the motion of a hydraulic cylinder. The VVDP provides a variable flow together with a directional valve and a throttling valve to regulate the cylinder motion in a cooperative manner.

A passivity based multi-mode controller is developed for cylinder motion control. Compared with the passive controller presented in Chapter 5, which deals only with a single chamber hydraulic actuator, this chapter focuses on a two chamber hydraulic cylinder with the assumption of a constant bulk modulus instead of a pressure dependent bulk modulus. The storage function presented in section 6.3.2 is formulated using the hydraulic force. This unique storage function can be augmented with the passivity based Lyapunov function derived for the mechanical part (cylinder position, velocity) to derive a passive control law.

Another highlight of the control strategy is the novel way to distribute different control efforts that are operated at different bandwidths. The circuit provides three control actuators, including a VVDP to provide a variable pump flow, a proportional valve to provide a variable orifice opening area, and a directional valve to switch the flow direction. A novel control effort distribution method is developed, which can distribute the total control effort between the VVDP and the proportional valve, so that the VVDP

output flow follows a low frequency trajectory, and the throttling valve opening area follows a high frequency trajectory with normally large opening. The approach compensates for the difference in control bandwidths between the VVDP and the proportional valve, while minimizing the valve throttling loss.

The proposed direct displacement circuit and the controller are implemented experimentally. The experimental result proves the feasibility and the effectiveness of the hydraulic circuit configuration and the control strategy.

Chapter 7

Conclusion and Future work

In this chapter, section 7.1 provides a summary of the thesis presented in the previous chapters, followed by the contributions made in this research work in sec 7.2. This chapter concludes with a proposal for future research paths.

7.1 Summary

High speed on/off valve enabled digital hydraulics have the potential to be competitive to current hydraulic system architectures, because digital hydraulics combine the high efficiency of variable displacement units and the good control bandwidth of the valve controlled systems. A novel high speed 3-way rotary on/off valve has been proposed as the enabling technology to build different digital hydraulic architectures. This thesis supports the modeling, control, and implementation of the rotary valve.

First, the 3-way rotary on/off valve implemented in a VVDP circuit needs to be optimized. The optimization objective is to find the valve geometric parameters and its operating conditions, so that the main valve's operation losses can be minimized. Given the complex flow path inside the valve, existing analytical equations are not sufficient to model the valve losses as explicit functions of the valve's key geometric parameters and the valve's operating conditions (i.e. flow, on/off frequency, etc). CFD is utilized to aid the valve loss modeling, and the models can further be fit into the valve optimization framework. CFD is also utilized to guide the design of a smooth flow path inside the valve.

Second, the self-spinning feature of the rotary valve works best with a non-contact sensor for measuring the spool's angular position to maintain the simple sealing structure. The limitations on the sensor size and the sensing range lead to a low resolution optical sensor, which produces an angular position signal at irregular time intervals. An event based Kalman filter was developed, which can estimate the spool angular position and velocity accurately from the irregular measurement events.

Third, the sensing approach of using a set of optical sensors was also applied to measure the spool's axial position. The spool's rotary motion introduces a periodic noise on the measurement of the spool's axial position. A controller which directly feeds back the noisy measurement will cause the spool's position to oscillate. The key solution to eliminating the oscillation is to distinguish the noise from the spool's position. A periodic time time-varying model is proposed to capture the structured noise's dynamics. This model can accurately reproduce the noise with a low order model. Augmenting the noise model with the dynamic model of the spool's axial position, a robust observer can be developed to estimate both the spool's axial position and the periodic noise.

Fourth, a passivity based nonlinear controller considering the spool chamber pressure dynamics was developed for controlling the spool's axial position. The observability of the system states (including the spool's axial position and velocity) from the corrupted spool position measurement was investigated. A Kalman filter was selected as the high gain observer to estimate the spool position and velocity. This information was fed back to the passive nonlinear controller to regulate the spool axial position.

Last, the VVDP was utilized in a direct displacement control circuit. A multi-mode nonlinear controller was developed to maneuver a double chamber single ended linear hydraulic actuator in an open circuit. The flow fed into the actuator supply chamber was directly regulated using the VVDP. A throttling valve was utilized between the return chamber and the tank. The throttling valve was mainly used to increase the control bandwidth, because the valve can respond faster than the VVDP. In addition, the throttling valve was utilized to manipulate the return chamber pressure when it was too low or too high. The throttling valve was controlled to be as open as possible to minimize the throttling loss. The accurate position control of the hydraulic actuator was achieved in an energy efficient manner.

Here is a list of my publications which are included in this thesis:

1. P. Y. Li and M. Wang, "Natural Storage Function for Passivity-Based Trajectory Control of Hydraulic Actuators", IEEE/ASME Transactions on Mechatronics, vol. 19, no. 3, pp. 1057−−1068, June 2014, DOI : 10.1109/$TMECH$.2013.2266916

2. H. Tu, M. B. Rannow, M. Wang, P. Y. Li, and T. R. Chase, "Design, Modeling and Validation of a High-Speed Rotary PWM On/Off Valve for Use in Virtually Variable Displacement Pumps", ASME Journal of Dynamic Systems, Measurement and Control, Vol. 134, November, 2012.

3. M. Wang and P. Y. Li, "Displacement Control of Hydraulic Actuators Using a Passivity Based Nonlinear Controller", ASME DSC Conference, [DSCC2012-MOVIC2012- 8784], Ft. Lauderdale, Nov. 2012.

4. P. Y. Li and M. Wang, "Passivity based nonlinear control of hydraulic actuators based on an Euler-Lagrange Formulation", ASME DSCC 2011 Bath Symposium on PTMC, Arlington, VA, October, 2011.

5. M. Wang, P. Y. Li, H. Tu, M. Rannow and T. R. Chase, "Direct Displacement Control of Hydraulic Actuators Based on a Self-Spinning Rotary On/Off Valve", 2011 International Fluid Power Exhibition (IFPE), Paper number: 20.2, Las Vegas, NV, March, 2011.

6. H. Tu, M. B. Rannow, M. Wang, P. Y. Li and T. R. Chase, "High-speed 4 way rotary on/off valve for virtually variable displacement pump/motor applications", ASME DSCC 2011 Bath Symposium on PTMC, Arlington, VA, October, 2011.

7. H. Tu, M. B. Rannow, M. Wang, P. Y. Li and T. R. Chase, "The Advantages and Feasibility of Externally Actuating a High-speed Rotary On/Off Valve", 2011 International Fluid Power Exhibition (IFPE), Paper number: 20.3, Las Vegas, NV, March, 2011.

8. Wang M. Tu H. Rannow M. Li P. Y. Chase T R. "CFD Analysis of a Novel High Speed Rotary ON/Off Valve", Proc. of 6th FPNI-PhD Symp. pp. 283 − −294, West Lafayette, IN, June, 2010

9. M. Rannow, H. Tu, M. Wang, P. Y. Li and T. R. Chase, "Optimal Design of a High-Speed On/off Valve for a Hydraulic Hybrid Vehicle Application", Proceedings of the $7th$ International Fluid Power Conference, Aachen, Germany, March 2010.

10. M. Wang and P. Y. Li, "Duty Ratio Control of a Rotary PWM valve with Periodic Measurement Error", Proceedings of the 2009 American Control Conference, St. Louis, MO, 2009. (Best presentation in session)

11. H. Tu, M. Rannow, M. Wang, P. Y. Li, and T. R. Chase, "Modeling and Validation of a High Speed Rotary PWM On/Off Valve", Proceedings of the ASME 2009 Dynamic Systems and Control Conference 2763, DSCC 2009 Bath Symposium PTMC, Hollywood, 2009.

12. M. Wang, and P. Y. Li, "Event Based Kalman Filter Observer For Rotary High Speed On/Off Valve", Proceedings of the 2008 American Control Conference, pp. 1546 – 1551, June, 2008.

13. H. Tu, M. B. Rannow, J. D. Van de Ven, M. Wang, P. Y. Li and T. R. Chase, "High Speed Rotary Pulse Width Modulated On/Off Valve", ASME-IMECE 2007 – 42559, Seattle, WA, November, 2007.

7.2 Contributions

The contributions of the work described in this dissertation are the following:

- In the CFD based modeling of hydraulic valves, a semi-empirical formula to predict the valve spool pressure drop was developed. This approach can be applied to analyze similar types of valves.

- We developed an event based Kalman filter to accurately estimate the states of a system given a measurement detected at irregular time instants, and successfully implemented it experimentally. This Kalman filter estimator can be applied to systems with slow sampling time and/or with low resolution sensors to increase the estimation accuracy.

- A low order model to cope with the system was proposed where the measurement was corrupted with a periodic structured noise. An augmented system combining the original system dynamics and the structured noise model was considered. The condition for the augmented system to be observable was defined.

- A passivity based nonlinear controller was implemented experimentally to accurately manipulate a linear hydraulic actuator. Some of the states utilized in the controller come from a high gain observer. The combined observer-controller was proved both theoretically and experimentally to be effective on regulating the observation errors and the tracking errors to zero.

- A direct displacement control open circuit and a corresponding multi-mode nonlinear controller was proposed for the positioning of a single degree-of-freedom hydraulic actuator. This hydraulic architecture can achieve good position tracking, while reducing the usage of throttling valves to improve system efficiency. The control efforts and the system states were proved to be continuous and bounded.

7.3 Further work

The research conducted in this dissertation can be continued in the following areas.

Rotary sensor threshold adaptation

As presented in chapter 3, the spool rotary position is sensed via a set of low resolution optical sensors. The analog spool rotary position measurement from the optical encoder needs to be discretized to generate the codewheel sector transition event. A threshold is required to discretize the analog position measurement signal. Chapter 3 has discussed the event detection time error due to the bias on the threshold estimate. The threshold estimate error was assumed to be of zero mean. If the estimation error is not zero mean, the angular position measurement error will not be a zero mean noise. Instead, it will have a certain repeated pattern. The threshold value needs to be adapted in real time. Otherwise, the position error due to the threshold bias will not be zero mean, and the estimation of the spool rotary position will have a bias.

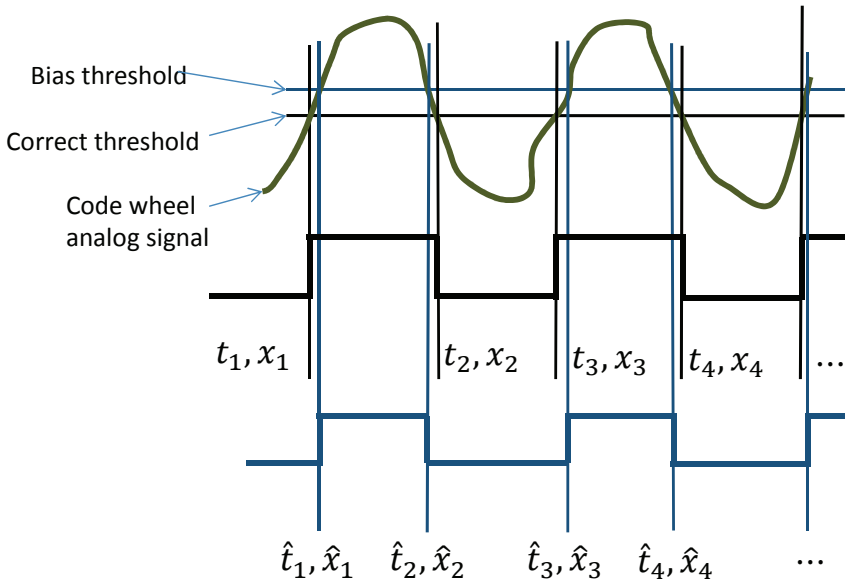

Figure 7.1: Angular position measurement error caused by the threshold bias

As shown in Fig. 7.1, we use t_i to denote the time when the true code wheel edge crossing event happens, and x_i to denote the spool angular position at t_i. We use $\hat{t}_i$ to denote the estimation of this event time with a bias threshold value, and $\hat{x}_i$ to denote the true spool angular position at $\hat{t}_i$. The detection time error is denoted as $e_i = t_i - \hat{t}_i$. Due to the bias on the threshold value, the transition event which occurred at t_i was detected at $\hat{t}_i$. The true angular position at $\hat{t}_i$ is $\hat{x}_i$, but the estimator treats the measurement of the spool's angular position of the spool as position is x_i at $\hat{t}_i$. This time error introduces a spool angular position measurement error. If the spool rotates at a constant angular velocity, we can observe the following properties:

- the sum of the detection time error will add up to zero over one revolution, $\sum e_i = 0$. This means that even if the threshold is biased, using the measurement information over one revolution to estimate the spool angular velocity will be unbiased.

- the detection time error switches signs for every measurement, i.e. $e_1 > 0$, $e_2 < 0$, $e_3 > 0$, and etc.

One research topic we propose here is how to adapt the threshold in real time, so that the estimate of the threshold converges to the true threshold. The framework as shown in Fig. 7.2 is proposed. If the threshold value is a constant, or slowly varying, and the spool angular velocity stays constant, or slowly varying, the average of the state estimation can potentially be fed back to adjust the threshold. How to develop a robust threshold update mechanism requires further research investigation.

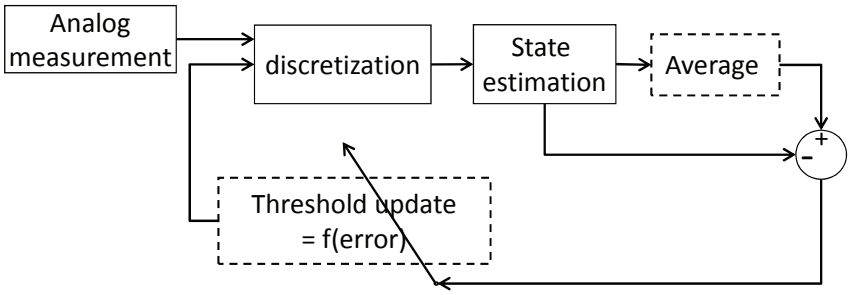

Figure 7.2: Threshold Value Adaptation Framework

Sensor fusion

In the VVDP system, the inlet pressure is being pulse width modulated, and the inlet pressure varies depending on whether the valve connects the inlet to load or to tank. The inlet pressure exhibits a repeated pattern, and the pattern frequency is the same as the valve PWM frequency. The PWM frequency is "N" times the spool angular frequency, and "N" represents the PWM sections per valve spool rotation. In the prototype VVDP system, $N = 3$. Therefore, the inlet pressure profile provides some sensing information on the valve PWM frequency, which equivalently provides the valve spool rotary frequency. In addition, the PWM valve duty ratio is originally defined based on this valve feature, which is the time over one pulse width period when the inlet is connected to the load branch. Therefore the duty ratio can be processed from the valve inlet pressure. Due to the pressure dynamics, the duty ratio reflected from the inlet pressure is slightly different from the "theoretical" duty ratio. Still, the inlet pressure constitutes a secondary sensor to provide the duty ratio information, and equivalently the valve spool axial position information. However, processing the duty ratio requires

the collection of the valve inlet pressure over at least one PWM period, and therefore this sensor signal is not a "continuous " measurement signal. How to merge the pressure and optical sensing information to increase the sensing precision is an interesting topic for further research.

Introducing adaptive control to displacement control

The performance of the displacement controller discussed in chapter 6 can be improved if the parameter adaptation approach is utilized to estimate the system parameters that cannot be easily measured, or slowly vary on-line. In another research project [96], a novel nonlinear function parameterization model was proposed for nonlinear adaptive controller design. Applying this approach to the linear hydraulic actuator control problem, functions with unknown parameters appearing nonlinearly (for example, actuator dead volume) can be re-parameterized linearly, which significantly simplifies the adaptive controller design. This approach has been successfully applied to the control of a single linear hydraulic actuator powered by a constant pressure source [96]. How to adopt it to the direct displacement control framework could be investigated in the future.

Final words

On off valve based control of hydraulic systems has been studied and proved to be a viable solution to realize both a low cost and a good control performance simultaneously. The key enabling technology for this digital hydraulic architecture is a high speed on/off valve. A novel high speed rotary 3-way on/off valve has been developed, and the research work described in this script supports the development of the on/off valve itself, as well as the development of utilizing the on/off valve in a virtually variable displacement pump configuration. The actuation, sensing, and control algorithms developed here can not only effectively facilitate the operation of the rotary valve, but they can also be applied to the motion sensing and control of hydraulic actuators in broader applications.

References

[1] Perry Y Li, Cassie Y Li, and Thomas R Chase. Software enabled variable displacement pumps. In *ASME International Mechanical Engineering Congress and Exposition, Orlando, FL*, volume 12, pages 63–72, 2005.

[2] Petter Krus. On load sensing fluid power systems. *Division of Fluid Power Control Department of Mechanical Engineering, Linkoping University, Sweden*, 1988.

[3] Haink C Tu, Michael B Rannow, Meng Wang, Perry Y Li, Thomas R Chase, and James D Van de Ven. Design, modeling, and validation of a high-speed rotary pulse-width-modulation on/off hydraulic valve. *Journal of dynamic systems, measurement, and control*, 134(6), 2012. paper number: 061002.

[4] Matti Linjama, Mikko Huova, Pontus Boström, Arto Laamanen, Lauri Siivonen, Lionel Morel, Marina Waldèn, and Matti Vilenius. Design and implementation of energy saving digital hydraulic control system. In *Vilenius, J. & Koskinen, KT (eds.) The Tenth Scandinavian International Conference on Fluid Power, May 21-23, 2007, Tampere, Finland, SICFP'07*, 2007.

[5] Matti Linjama and Matti Vilenius. Digital hydraulics-towards perfect valve technology. In *Vilenius, J. & Koskinen, KT (eds.) The Tenth Scandinavian International Conference on Fluid Power, May 21-23, 2007, Tampere, Finland, SICFP'07*, 2007.

[6] Forbes T Brown, SC Tentarelli, and S Ramachandran. A hydraulic rotary switched-inertance servo-transformer. *Journal of Dynamic Systems, Measurement, and Control*, 110(2):144–150, 1988.

[7] SP Tomlinson and CR Burrows. Achieving a variable flow supply by controlled unloading of a fixed-displacement pump. *Journal of dynamic systems, measurement, and control*, 114(1):166–171, 1992.

[8] Jianwei Cao, Linyi Gu, Feng Wang, and Minxiu Qiu. Switchmode hydraulic power supply theory. In *ASME 2005 International Mechanical Engineering Congress and Exposition*, pages 85–91. American Society of Mechanical Engineers, 2005.

[9] Michael B Rannow, Haink C Tu, Perry Y Li, and Thomas R Chase. Software enabled variable displacement pumps: experimental studies. *ASME Paper No. IMECE2006-14973*, 2006.

[10] Takashi Kajima and Yoshihisa Kawamura. Development of a high-speed solenoid valve: investigation of solenoids. *Industrial Electronics, IEEE Transactions on*, 42(1):1–8, 1995.

[11] Michael M. Schechter. Fast response multipole solenoids. In *SAE Technical Paper*. SAE International, 02 1982.

[12] Takeo Kushida. High speed, powerful and simple solenoid actuator "disole" and its dynamic analysis results. In *SAE Technical Paper*, 02 1985.

[13] Takashi Kajima, Shuichi Satoh, and Ryuichi Sagawa. Development of a high-speed solenoid valve(experimental results under actual loads). *Nippon Kikai Gakkai Ronbunshu, C Hen/Transactions of the Japan Society of Mechanical Engineers, Part C*, 60(576):2744–2751, 1994.

[14] Sung-Hwan Park, Ato Kitagawa, and Masayuki Kawashima. Water hydraulic high-speed solenoid valve part 1: Development and static behaviour. *Proceedings of the Institution of Mechanical Engineers, Part I: Journal of Systems and Control Engineering*, 218(5):399–409, 2004.

[15] Shinichi Yokota and Kotarou Akutu. A fast-acting electro-hydraulic digital transducer: A poppet-type on-off valve using a multilayered piezoelectric device. *JSME international journal. Ser. 2, Fluids engineering, heat transfer, power, combustion, thermophysical properties*, 34(4):489–495, 1991.

[16] Hao Lu, Cheng-lin Zhu, Si Zeng, Yuping Huang, Min Zhou, and Youwen He. Study on the new kind of electro-hydraulic high-speed on-off valve driven by pzt components and its powerful and speedy technique. *Jixie Gongcheng Xuebao(Chinese Journal of Mechanical Engineering)(China)*, 38(8):118–121, 2002.

[17] Sojiro Tsuchiya, Hironao Yamada, and Takayoshi Muto. A precision driving system composed of a hydraulic cylinder and high-speed on/off valves. *International Journal of Fluid Power*, 2(1):7–16, 2001.

[18] B Winkler. Development of a fast low-cost switching valve for big flow rates. In *3rd FPNI-PhD Symposium on Fluid Power, Terrassa, Spain*, 2004.

[19] Xin Fu Lu, Richard T Burton, Greg J Schoenau, and XR Zeng. Feasibility study of a digital variable flow divider valve. In *SAE Technical Paper*. SAE International, 09 1991.

[20] Tom Royston and Rajendra Singh. Development of a pulse-width modulated pneumatic rotary valve for actuator position control. *Journal of dynamic systems, measurement, and control*, 115(3):495–505, 1993.

[21] P Cui, Richard T Burton, and PR Ukrainetz. Development of a high speed on/off valve. In *SAE Technical Paper*. SAE International, 09 1991.

[22] Surendra Gaikwad, Kunal Arora, Vamshi Korivi, and Su K Cho. Steady and transient cfd approach for port optimization. *SAE International Journal of Materials & Manufacturing*, 1(1):754–762, 2009.

[23] Bao Min, Fu Xin, and Chen Ying. Computational fluid dynamics approach to pressure loss analysis of hydraulic spool valve. In *Fifth International Conference on Fluid Power Transmission and Control, ICFP 2001*. Citeseer, 2001.

[24] Ryo Morita, Fumio Inada, Michitsugu Mori, Kenichi Tezuka, and Yoshinobu Tsujimoto. Cfd simulations and experiments of flow fluctuations around a steam control valve. *Journal of Fluids Engineering*, 129(1):48–54, 2007.

[25] James A Davis and Mike Stewart. Predicting globe control valve performance part i: Cfd modeling. *Journal of Fluids Engineering - transactions of the ASME - J FLUID ENG*, 124(3):772–777, 2002.

[26] Nicholas Paul Whitehead, Arezki Slaouti, and Howard Taylor. Optimisation of flow through a pneumatic control valve using cfd analysis and experimental validation. *International Journal of Fluid Power*, 8(3):31–41, 2007.

[27] Gianpietro Di Rito. Experiments and cfd simulations for the characterisation of the orifice flow in a four-way servovalve. *International Journal of Fluid Power*, 8(2):37–46, 2007.

[28] Riccardo Amirante, Giuseppe Del Vescovo, and Antonio Lippolis. Evaluation of the flow forces on an open centre directional control valve by means of a computational fluid dynamic analysis. *Energy Conversion and Management*, 47(13):1748–1760, 2006.

[29] Riccardo Amirante, Giuseppe Del Vescovo, and Antonio Lippolis. Flow forces analysis of an open center hydraulic directional control valve sliding spool. *Energy conversion and Management*, 47(1):114–131, 2006.

[30] José R Valdés, Mario J Miana, Jose L Nunez, and Thomas Pütz. Reduced order model for estimation of fluid flow and flow forces in hydraulic proportional valves. *Energy Conversion and Management*, 49(6):1517–1529, 2008.

[31] Qin Zhang. Hydraulic linear actuator velocity control using a feedforward-plus-pid control. *International Journal of Flexible Automation and Integrated Manufacturing*, 7(3/4):277–292, 1999.

[32] Andrew R Plummer and ND Vaughan. Robust adaptive control for hydraulic servosystems. *Journal of Dynamic Systems, Measurement, and Control*, 118(2):237–244, 1996.

[33] Teng Joon Lim. Pole placement control of an electrohydraulic servo motor. In *Power Electronics and Drive Systems, 1997. Proceedings., 1997 International Conference on*, volume 1, pages 350–356. IEEE, 1997.

[34] Roger Fales and Atul Kelkar. Robust control design for a wheel loader using h and feedback linearization based methods. *ISA transactions*, 48(3):312–320, 2009.

[35] JE Bobrow and K Lum. Adaptive, high bandwidth control of a hydraulic actuator. *Journal of dynamic systems, measurement, and control*, 118(4):714–720, 1996.

[36] Hassan K Khalil. *Nonlinear systems*, volume 3. Prentice hall Upper Saddle River, 2002.

[37] Jean-Jacques E Slotine. Sliding controller design for non-linear systems. *International Journal of control*, 40(2):421–434, 1984.

[38] Andrew G Alleyne and Rui Liu. Systematic control of a class of nonlinear systems with application to electrohydraulic cylinder pressure control. *Control Systems Technology, IEEE Transactions on*, 8(4):623–634, 2000.

[39] Garett A Sohl and James E Bobrow. Experiments and simulations on the nonlinear control of a hydraulic servosystem. *Control Systems Technology, IEEE Transactions on*, 7(2):238–247, 1999.

[40] Adrian Bonchis, Peter I Corke, David C Rye, and Quang Phuc Ha. Variable structure methods in hydraulic servo systems control. *Automatica*, 37(4):589–595, 2001.

[41] Russell Sindrey and Gary M Bone. Position tracking control of a miniature water hydraulic rotary actuator. *Journal of dynamic systems, measurement, and control*, 131(6):061003, 2009.

[42] T-L Chern and Y-C Wu. Design of integral variable structure controller and application to electrohydraulic velocity servosystems. *Control Theory and Applications, IEE Proceedings D*, 138(5):439–444, 1991.

[43] Alexander G Loukianov, Jorge Rivera, Yuri V Orlov, and EY Morales Teraoka. Robust trajectory tracking for an electrohydraulic actuator. *IEEE Transactions on Industrial Electronics*, 56(9):3523–3531, 2009.

[44] Shu Wang, Saeid Habibi, and Richard Burton. Sliding mode control for an electrohydraulic actuator system with discontinuous non-linear friction. *Proceedings of*

the Institution of Mechanical Engineers, Part I: Journal of Systems and Control Engineering, 222(8):799–815, 2008.

[45] Shu Wang, Richard Burton, and Saeid Habibi. Sliding mode controller and filter applied to an electrohydraulic actuator system. *Journal of Dynamic Systems, Measurement, and Control*, 133(2):024504, 2011.

[46] Andrew Alleyne. A systematic approach to the control of electrohydraulic servosystems. In *American Control Conference, 1998. Proceedings of the 1998*, volume 2, pages 833–837. IEEE, 1998.

[47] Bin Yao, Fanping Bu, John Reedy, and George TC Chiu. Adaptive robust motion control of single-rod hydraulic actuators: theory and experiments. *Mechatronics, IEEE/ASME Transactions on*, 5(1):79–91, 2000.

[48] Daniel E Koditschek. The application of total energy as a lyapunov function for mechanical control systems. *Contemporary mathematics*, 97:131, 1989.

[49] Nader Sadegh and Roberto Horowitz. Stability and robustness analysis of a class of adaptive controllers for robotic manipulators. *The International Journal of Robotics Research*, 9(3):74–92, 1990.

[50] Andreas Kugi. *Non-linear control based on physical models: electrical, hydraulic, and mechanical systems*. Springer-Verlag New York, Inc., 2001.

[51] Ortega Romeo, Loria Antonio, Johan Nicklasson Per, and Sira Ramırez Hebertt. Passivity-based control of euler-lagrange systems, 1998.

[52] Perry Y Li and Roger F Ngwompo. Power scaling bond graph approach to the passification of mechatronic systems with application to electrohydraulic valves. *Journal of dynamic systems, measurement, and control*, 127(4):633–641, 2005.

[53] Perry Y Li and Kailash Krishnaswamy. Passive bilateral teleoperation of a hydraulic actuator using an electrohydraulic passive valve. *International Journal of Fluid Power*, 5(2):43–55, 2004.

[54] Grabmair Gernot. and Schlacher Kurt. Energy-based nonlinear control of hydraulically actuated mechanical systems. In *44th IEEE Conference on Decision and Control, and the European Control Conference*, pages 7520–7525, 2005.

[55] Sakai Satoru. and Stramigioli Stefano. Passivity based control of hydraulic robot arms using natural casimir functions-theory and experiments. In *2008 IEEE/RSJ International Conference on Intelligent Robots and Systems*, pages 538–544, 2008.

[56] Frederic Mazenc and E Richard. Stabilization of hydraulic systems using a passivity property. *Systems & Control Letters*, 44(2):111–117, 2001.

[57] Perry Y Li and Meng Wang. Passivity based nonlinear control of hydraulic actuators based on an euler-lagrange formulation. In *ASME 2011 Dynamic Systems and Control Conference and Bath/ASME Symposium on Fluid Power and Motion Control*, pages 107–114. American Society of Mechanical Engineers, 2011.

[58] Perry Y Li and Meng Rachel Wang. Natural storage function for passivity-based trajectory control of hydraulic actuators. *IEEE/ASME Transactions on Mechatronics*, 19(3):1057–1068, 2014.

[59] Denis Garagić and Krishnaswamy Srinivasan. Application of nonlinear adaptive control techniques to an electrohydraulic velocity servomechanism. *Control Systems Technology, IEEE Transactions on*, 12(2):303–314, 2004.

[60] Amit Mohanty and Bin Yao. Indirect adaptive robust control of hydraulic manipulators with accurate parameter estimates. *Control Systems Technology, IEEE Transactions on*, 19(3):567–575, 2011.

[61] Cheng Guan and Shuangxia Pan. Nonlinear adaptive robust control of single-rod electro-hydraulic actuator with unknown nonlinear parameters. *IEEE Transactions on Control Systems Technology*, 16(3):434–445, May 2008.

[62] Graham Clifford Goodwin, Stefan F Graebe, and Mario E Salgado. *Control system design*, volume 240. Prentice Hall New Jersey, 2001.

[63] A.N. Atassi and Hassan K. Khalil. A separation principle for the stabilization of a class of nonlinear systems. *IEEE Transactions on Automatic Control*, 44(9):1672–1687, Sep 1999.

[64] Hyungbo Shim and Andrew R. Teel. Asymptotic controllability and observability imply semiglobal practical asymptotic stabilizability by sampled-data output feedback. *Automatica*, 39(3):441 – 454, 2003.

[65] Rolf Findeisen, Lars Imsland, Frank Allgwer, and Bjarne A. Foss. Output feedback stabilization of constrained systems with nonlinear predictive control. *International Journal of Robust and Nonlinear Control*, 13(3-4):211–227, 2003.

[66] Allan J. Hewett. Hydraulic circuit flow control, July 19 1994. US Patent 5,329,767.

[67] Rpbert Rahmfeld and Monika Ivantysynova. Development and control of energy saving hydraulic servo drives. In *Proc. of the 1st FPNI-PhD Symposium, Hamburg Germany*, pages 167–189, 2000.

[68] Kim Heybroek. *Saving Energy in Construction Machinery using Displacement Control Hydraulics Concept Realization and Validation*. Linköping University Electronic Press, Linköping, 2008.

[69] Christopher Williamson and Monika Ivantysynova. Pump mode prediction for four-quadrant velocity control of valveless hydraulic actuators. In *Proceedings of the JFPS International Symposium on Fluid Power*, number 7 in 2, pages 323–328. The Japan Fluid Power System Society, 2008.

[70] Christopher Williamson and Monika Ivantysynova. Stability and motion control of inertial loads with displacement controlled hydraulic actuators. In *Proceedings of the 6th FPNI PhD Symposium, West Lafayette, USA*, pages 499–514, 2010.

[71] Michael B Rannow, Haink C Tu, Meng Wang, Perry Y Li, and Tom R Chase. Optimal design of a high-speed on/off valve for a hydraulic hybrid vehicle application. In *Proceedings of the 7th International Fluid Power Conference, Aachen, Germany*. Citeseer, 2010.

[72] H Tu, M Rannow, Meng Wang, P Li, and T Chase. The advantages and feasibility of externally actuating a high-speed rotary on/off valve. In *Proceedings of the 52nd National Conference on Fluid Power, National Fluid Power Association, Milwaukee, WI*, pages 53222–3219, 2011.

[73] ANSYS, Inc. *Gambit 2.1 tutorials*.

[74] ANSYS, Inc. *ANSYS Fluent 6.3 tutorials*.

[75] Donald F Young, Bruce R Munson, Theodore H Okiishi, and Wade W Huebsch. *A brief introduction to fluid mechanics*. John Wiley & Sons, 2010.

[76] Herbert E Merritt. *Hydraulic control systems*. John Wiley & Sons, 1967.

[77] Haink C Tu, M Rannow, J Van de Ven, Meng Wang, P Li, and T Chase. High speed rotary pulse width modulated on/off valve. In *Proceedings of the ASME International Mechanical Engineering Congress, Seattle, WA*, 2007. paper number: 42559.

[78] Antonino Risitano. *Mechanical Design*. CRC Press, 2011.

[79] Haink Cheng Tu. *High Speed Rotary PWM On/Off Valves for Digital Control of Hydraulic Pumps and Motors*. PhD thesis, University of Minnesota, 2014.

[80] NK Sinha, B Szabados, et al. New high-precision digital tachometer. *Electronics Letters*, 7(8):174–176, 1971.

[81] Alan Dunworth. Digital instrumentation for angular velocity and acceleration. *Instrumentation and Measurement, IEEE Transactions on*, 18(2):132–138, 1969.

[82] B Habibullah, H Singh, KL Soo, and LC Ong. A new digital speed transducer. *IEEE Transactions on Industrial Electronics and Control Instrumentation*, 4(IECI-25):339–342, 1978.

[83] Torkel Glad and Lennart Ljung. Velocity estimation from irregular, noisy position measurements. In *IFAC Proceedings Volumes*, volume 17-2, pages 1069–1073. Elsevier, 1984.

[84] Dan Simon. *Optimal state estimation: Kalman, H infinity, and nonlinear approaches*. John Wiley & Sons, 2006.

[85] Wilson J Rugh. *Linear system theory*, volume 2. Prentice Hall Upper Saddle River, NJ, 1996.

[86] Haink Tu, Mike Rannow, Meng Wang, Perry Li, and Tom Chase. The advantages and feasibility of externally actuating a high-speed rotary on/off valve. In *Proceedings of the 52nd National Conference on Fluid Power, National Fluid Power Association, Milwaukee, WI*, 2011.

[87] Andreas Kugi and Wolfgang Kemmetmüller. New energy-based nonlinear controller for hydraulic piston actuators. *European Journal of Control*, 10(2):163–173, 2004.

[88] Yu Jinghong, Chen Zhaoneng, and Lu Yuanzhang. The variation of oil effective bulk modulus with pressure in hydraulic systems. *Journal of dynamic systems, measurement, and control*, 116(1):146–150, 1994.

[89] Nader Sadegh and Roberto Horowitz. Stability and robustness analysis of a class of adaptive controllers for robotic manipulators. *The International Journal of Robotics Research*, 9(3):74–92, 1990.

[90] Gene H Golub and Charles F Van Loan. *Matrix computations*, volume 3. JHU Press, 2012.

[91] Brian DO Anderson and John B Moore. *Optimal filtering*, volume 21. Englewood Cliffs, 1979.

[92] Haink C Tu, Michael B Rannow, Meng Wang, Perry Y Li, Thomas R Chase, and Kai Loon Cheong. High-speed 4-way rotary on/off valve for virtually variable displacement pump/motor applications. In *ASME. Dynamic Systems and Control Conference, ASME 2011 Dynamic Systems and Control Conference and Bath/ASME Symposium on Fluid Power and Motion Control*, volume 1, pages 201–208, 2011.

[93] Venkar Durbha and Perry Li. A nonlinear spring model of hydraulic actuator for passive controller design in bilateral tele-operation. In *American Control Conference (ACC), 2012*, pages 3471–3476. IEEE, 2012.

[94] Perry Y Li. Lecture notes of special topics in dynamics and control. `http://http://www.me.umn.edu/courses/me8287/pdf/ME8287_IntermediateRobotics_Syllabus_S17_v1.1.pdf`, 2013,2017.

[95] Meng Wang and Perry Y Li. Passivity based adaptive control of a two chamber single rod hydraulic actuator. In *American Control Conference (ACC), 2012*, pages 1814–1819. IEEE, 2012.

[96] Meng Wang and Perry Y Li. Passivity based adaptive control of a two chamber single rod hydraulic actuator. In *American Control Conference (ACC), 2012*, pages 1814–1819. IEEE, 2012.

Appendix A

Observability grammian derivation

A.1 Observability grammian for system Eq.(A.1)

The augmented system defined in Eq.(A.1) is repeated here:

$$\begin{aligned}\frac{d}{dt}\underbrace{\begin{bmatrix}x_s\\x_d\end{bmatrix}}_{x_{aug}} &= \underbrace{\left[\begin{array}{c|c}A_s & 0_{2\times 2k}\\\hline 0_{2k\times 2} & 0_{2k\times 2k}\end{array}\right]}_{A_{aug}}\begin{bmatrix}x_s\\x_d\end{bmatrix} + \underbrace{\begin{bmatrix}B_s\\0_{2k\times 1}\end{bmatrix}}_{B_{aug}}u\\ y &= \underbrace{\begin{bmatrix}1 & 0 & C_d\end{bmatrix}}_{C_{aug}}x_{aug}\end{aligned} \tag{A.1}$$

With $t_0 = 0$, define $T = \frac{2\pi}{\omega}$ being the period, and the time interval being $[0, T]$, the observability grammian is calculated as:

$$M(0,T) = \int_0^T m(0,t)dt = \int_0^T \Phi^{\mathrm{T}}(t)C_{aug}^{\mathrm{T}}(t)C_{aug}(t)\Phi(t)dt \tag{A.2}$$

with

$m(0,t) =$

$$\left[\begin{array}{cc|ccccc} \phi_{11}^2 & \phi_{11}\phi_{12} & \phi_{11}\cos\omega t & \phi_{11}\sin\omega t & \cdots & \phi_{11}\cos k\omega t & \phi_{11}\sin k\omega t \\ & \phi_{12}^2 & \phi_{12}\cos\omega t & \phi_{12}\sin\omega t & \cdots & \phi_{12}\cos k\omega t & \phi_{12}\sin k\omega t \\ \hline & & \cos^2\omega t & \cos\omega t\sin\omega t & \cos\omega t\cos 2\omega t & \sin\omega t\sin 2\omega t & \cdots \\ & & & \sin^2\omega t & \sin\omega t\cos 2\omega t & \sin\omega t\sin 2\omega t & \cdots \\ & & & & \cos^2 2\omega t & \cos 2\omega t\sin 2\omega t & \cdots \\ & & & & & \sin^2 2\omega t & \cdots \\ & & & & & & \ddots \end{array}\right] \tag{A.3}$$

The upper left corner is determined by the plant dynamics only. Define $\gamma = \sqrt{\frac{K}{m}}$, the elements are:

$$\phi_{11} = \cos\gamma t; \quad \phi_{12} = \frac{1}{\gamma}\sin\gamma t; \quad \phi_{21} = -\gamma\sin\gamma t; \quad \phi_{22} = \cos\gamma t \tag{A.4}$$

The calculation of $M(0,T)$ is the integration by element of $m(0,t)$ from $t=0$ to $t=T$. Several observations from the lower right quadrant of the matrix $m(0,t)$ include:

- given two distinct integers $h \geq 1$, $g \geq 1$, $\int_0^T \cos h\omega t \cdot \cos g\omega t dt = 0$, $\int_0^T \cos h\omega t \cdot \sin g\omega t dt = 0$, $\int_0^T \sin h\omega t \cdot \sin g\omega t dt = 0$.

  Proof.

$$\begin{aligned} \int_0^T \cos h\omega t\cos g\omega t dt &= \int_0^T \frac{1}{2}\cos(h+g)\omega t dt + \int_0^T \frac{1}{2}\cos(h-g)\omega t dt \\ &= \frac{1}{2(h+g)}\sin(h+g)\omega t\Big|_0^T + \frac{1}{2(h-g)}\sin(h-g)\omega t\Big|_0^T = 0 \end{aligned} \tag{A.5}$$

  □

  Similar proofs apply to the other two cases.

- Given an integer $h \geq 1$, $\int_0^T \cos^2 h\omega t dt = \frac{T}{2}$, and $\int_0^T \sin^2 h\omega t dt = \frac{T}{2}$.

Proof.

$$\int_0^T \cos^2 h\omega t dt = \int_0^T \frac{1+\cos 2h\omega t}{2} dt = \int_0^T \frac{1}{2} dt + \frac{1}{2}\int_0^T \cos 2h\omega t dt = \frac{T}{2} \quad \text{(A.6)}$$

$$\int_0^T \sin^2 h\omega t dt = \int_0^T \frac{1-\cos 2h\omega t}{2} dt = \int_0^T \frac{1}{2} dt - \frac{1}{2}\int_0^T \cos 2h\omega t dt = \frac{T}{2} \quad \text{(A.7)}$$

□

Now we are ready to integrate $m(0,t)$. Firstly, we consider the integration of the upper left quadrant of $m(0,t)$:

$$\begin{aligned}
\Psi_{11} &= \int_0^T \phi_{11}^2 dt = \int_0^T cos^2(\gamma t) dt = \frac{T}{2} + \frac{\sin 2\gamma T}{4\gamma} \\
\Psi_{12} &= \int_0^T \phi_{11}\phi_{12} dt = \int_0^T \frac{\cos(\gamma t)\sin(\gamma t)}{\gamma} dt = \frac{1-\cos 2\gamma T}{4\gamma^2} \\
\Psi_{22} &= \int_0^T \phi_{22}^2 dt = \int_0^T \frac{cos^2(\gamma t)}{\gamma^2} dt = \frac{1}{\gamma^2}\left(\frac{T}{2} + \frac{sin 2\gamma T}{4\gamma}\right)
\end{aligned} \quad \text{(A.8)}$$

Next, we consider the lower right corner. This matrix integration turns out to be $\frac{T}{2}\mathrm{I}_{2k\times 2k}$.

Finally, we consider the off-diagonal elements integration, given an integer g, we have:

$$\begin{aligned}
&\int_0^T \phi_{11} \cos g\omega t dt = \int_0^T \cos\gamma t \cos g\omega t dt \\
&= \frac{1}{2(\gamma+g\omega)} \sin(\gamma+g\omega)t\Big|_0^T + \frac{1}{2(\gamma-g\omega)} \sin(\gamma-g\omega)t\Big|_0^T = \frac{\gamma \sin\gamma T}{(\gamma+g\omega)(\gamma-g\omega)}
\end{aligned} \quad \text{(A.9)}$$

$$\begin{aligned}
&\int_0^T \phi_{11} \sin g\omega t dt = \int_0^T \cos\gamma t \sin g\omega t dt \\
&= -\frac{1}{2(\gamma+g\omega)} \cos(\gamma+g\omega)t\Big|_0^T + \frac{1}{2(\gamma-g\omega)} \cos(\gamma-g\omega)t\Big|_0^T = \frac{g\omega(\cos\gamma T - 1)}{(\gamma+g\omega)(\gamma-g\omega)}
\end{aligned} \quad \text{(A.10)}$$

$$\begin{aligned}
&\int_0^T \phi_{12} \cos g\omega t dt = \frac{1}{\gamma}\int_0^T \sin\gamma t \cos g\omega t dt \\
&= \frac{-1}{2\gamma(\gamma+g\omega)} \cos(\gamma+g\omega)t\Big|_0^T + \frac{-1}{2\gamma(\gamma-g\omega)} \cos(\gamma-g\omega)t\Big|_0^T = \frac{1-\cos\gamma T}{(\gamma+g\omega)(\gamma-g\omega)}
\end{aligned} \quad \text{(A.11)}$$

$$\int_0^T \phi_{12} \sin g\omega t dt = \frac{1}{\gamma} \int_0^T \sin \gamma t \sin g\omega t dt$$
$$= \frac{-1}{2\gamma(\gamma + g\omega)} \sin(\gamma + g\omega)t \Big|_0^T + \frac{1}{2\gamma(\gamma - g\omega)} \sin(\gamma - g\omega)t \Big|_0^T = \frac{g\omega \sin \gamma T}{\gamma(\gamma + g\omega)(\gamma - g\omega)} \tag{A.12}$$

With the definition above, the grammian $M(0,t)$ will have the following form:

$$M(0,t) = \begin{bmatrix} \Psi & L \\ L^{\mathrm{T}} & \frac{T}{2} I_{2k \times 2k} \end{bmatrix}, \Psi \in \mathbb{R}^{2\times 2}, L \in \mathbb{R}^{2 \times 2k} \tag{A.13}$$

with

$$\Psi_{11} = \frac{T}{2} + \frac{\sin 2\gamma T}{4\gamma}$$
$$\Psi_{12} = \frac{1 - \cos 2\gamma T}{4\gamma^2}$$
$$\Psi_{22} = \frac{1}{\gamma^2} \left(\frac{T}{2} + \frac{sin 2\gamma T}{4\gamma} \right) \tag{A.14}$$

Appendix B

Copyright permission

B.1 Copyright Permission

The following copyright permission is obtained from the publisher.